The dynamics of towed seeding equipment

A Thesis Submitted to the

College of Graduate and Postdoctoral Studies

in Partial Fulfillment of the Requirements

for the degree of Master of Science

in the Department of Mechanical Engineering

University of Saskatchewan

Saskatoon

By

Ian W. P. Paulson

Permission to Use

In presenting this thesis in partial fulfilment of the requirements for a Postgraduate degree from the University of Saskatchewan, I agree that the Libraries of this University may make it freely available for inspection. I further agree that permission for copying of this thesis in any manner, in whole or in part, for scholarly purposes may be granted by the professor or professors who supervised my thesis work or, in their absence, by the Head of the Department or the Dean of the College in which my thesis work was done. It is understood that any copying or publication or use of this thesis or parts thereof for financial gain shall not be allowed without my written permission. It is also understood that due recognition shall be given to me and to the University of Saskatchewan in any scholarly use which may be made of any material in my thesis.

Requests for permission to copy or to make other use of material in this thesis in whole or part should be addressed to:

Head of the Department of Mechanical Engineering
57 Campus Drive
University of Saskatchewan
Saskatoon, Saskatchewan S7N 5A9
Canada

OR

Dean
College of Graduate and Postdoctoral Studies
University of Saskatchewan
105 Administration Place
Saskatoon, Saskatchewan S7N 5A2
Canada

Abstract

Seed depth consistency is a critical performance metric of agricultural seeding equipment. To improve productivity, equipment manufacturers have historically focused on increasing the equipment working width of hoe-opener style seeding drills (hoe drills). However, the physical limitations of hoe drill size do present a design challenge. Increasing seeding speed to improve equipment productivity continues to be a challenge for equipment designers. Most operating conditions restrict hoe-drill seeding speeds to approximately 2.2 m/s (5 mph); depth consistency generally degrades above this speed with current hoe drill technology.

This research focused on developing an understanding of why this performance degradation occurs as speed increases. The general industry hypothesis points vaguely to "excessive motion" of the components to which the soil-engaging tools connect (the row units). However, little research on the dynamics of towed agricultural implements was found in the open literature. An understanding of the mechanism(s) causing this "excessive motion" was sought during this research.

A 2-D simulation tool was developed in MATLAB® to provide equipment designers with the capability to conduct performance trade-off and sensitivity studies early in the prototype stage of a project. The simulation tool was compartmentalized so that changes to equipment geometry, component-soil contact models, or hydraulic systems could be modified with little or no change to other parts of the program.

Operational data were also collected using a small plot drill based on a New Holland P2070 Precision Hoe Drill. Data were collected at multiple operating speed up to 4.4 m/s (10 mph) to characterize depth consistency issues present at higher speeds. Various geometric seed depth and hydraulic pressure settings were also tested. Kinematic parameters (acceleration, position), force, hydraulic pressure, and video of the instrumented row unit were recorded during steady-state the operation of the machine in typical seeding conditions.

Measured data aided in calibrating aspects of the simulation tool, and the tool enabled certain performance features in the measurement data to be explored further. Frequency domain acceleration power spectra revealed that row unit acceleration power was generally concentrated at two frequencies. The terrain profile of the test field contained furrows from

the previous seeding operation; this resulted in acceleration power to be concentrated at a distinct speed-dependent frequency related to the furrow spacing. While somewhat expected, this indicated the general inability of the current design to attenuate terrain inputs. The small packer wheel provided little compliance between the row unit and soil, so improving the attenuation performance of the system could improve depth consistency performance in future designs.

The second major acceleration spectra feature was related to the arrangement of the hoe opener and trailing packer wheel; both rigidly connect to the row unit body. The row unit position changed when the packer wheel encountered a terrain bump or dip; this resulted in a change in the vertical position of the hoe opener located in front of the packer wheel. Immediate changes in the operating depth of the hoe opener tool resulted. Also, depth changes generally modified the terrain such that a new bump or dip was created in the soil surface preceding the packer wheel, thus creating a feedback path between the hoe opener and packer wheel.

Considering the simplifications of the 2-D model, agreement between simulated and measured data was encouraging. The frequencies of the above phenomena were in reasonable agreement throughout the speed range of interest. Power spectra amplitude differences were likely due to both input terrain differences between simulation and test terrains, and simplifications made in representing soil-tire and soil-tool contact. Future work to improve these sub-models, and to further explore the observed non-linear effect of hydraulic pressure changes would improve the predictive accuracy of the model presented.

Acknowledgements

A heartfelt Thank You is extended to my research co-supervisors, Professors Scott Noble and Allan Dolovich of the Mechanical Engineering department at the University of Saskatchewan. It has been a true privilege to work with both of you. The respect, encouragement, time investment, and understanding that you have both extended throughout the many seasons of this project helped to reinforce my choice of pursuing an advanced degree. Thank you for your sincere interest in the topic you have shown throughout the project.

Secondly, my committee members, Professors JD Johnston and Travis Wiens of the Mechanical Engineering department, deserve many thanks as well. The thought-provoking questions were welcomed and appreciated. Thank you for keeping an eye towards a realistic result from the relatively short timeframe over which a masters program occurs.

Thirdly, to Joel Gervais and Jim Henry of the Innovation group at CNH Industrial in Saskatoon: thank you for the project opportunity. Your interest in this research provided a backdrop of industrial relevance to keep me motivated. Additionally, without the physical resources provided by CNH Industrial, this project simply would not have been possible.

Lastly, financial support provided by both CNH Industrial and the Natural Sciences and Engineering Research Council of Canada (NSERC) through the Industrial Postgraduate Scholarship program is gratefully acknowledged. This scholarship program provided an excellent gateway to industry collaboration and it is unfortunate that it is no longer in place.

To my wife, Taylor, and my parents, Keith and Marj.

Taylor, your patience and encouragement were integral in helping me see this journey through. I am forever grateful for your support, both silent and spoken. I look forward to many more milestones together in our future.

Dad, thank you for your willingness to share your time to discuss your thoughts and experiences from three decades of farm operation at a phone call's notice; and thanks for listening when you didn't get a chance to do much of the talking.

Mom, through all of this you have been the embodiment of seeing a challenge through to the end. Thank you for setting this example once again.

Contents

List of Tables

List of Figures

List of Abbreviations

CG	Center of gravity
CS	Coordinate system
dB	Decibel
DEM	Discrete element method
DOF	Degree of freedom
FBD	Free body diagram
FEM	Finite element method
FFT	Fast Fourier transform
FIR	Finite impulse response
HSUPP	Hitch support link
IMU	Inertial measurement unit
ISTVS	International Society for Terrain Vehicle Systems
PC	Packer wheel center
PSD	Power spectral density
PW	Packer wheel
RMS	Root mean square
RMSE	Root mean square error
RU	Row unit
SF	Subframe
TWL	Tail wheel link
TWSL	Tail wheel support link
WA	Walking axle
WC	Wheel center

Chapter 1

Introduction

1.1 Introduction

Demand for efficient food production continues to grow as global population estimates exceed 9 billion people by 2050 (United Nations: Department of Economic and Social Affairs, Population Division, 2015). While world populations may be increasing, shifting demographics in western Canada mean that fewer farm operators are managing larger and larger farming operations. From 2006 to 2011, Statistics Canada reported a 16.4% decrease in the number of farm operators in Saskatchewan, while the average farm size in the province increased 15.1% during the same time frame (Statistics Canada, 2016). Similar trends exist in the other prairie provinces.

With seemingly more land to cover each growing season, the productivity demands of an average farming operation continue to increase. This begins with seeding the crop in the spring season. In order to minimize frost risk near the end of the growing season, seeding typically commences as early as soil temperature and moisture conditions permit. Without increased seeding capacity (using multiple implements or increasing machine productivity), increasing farm size competes with the need to complete seeding in a timely fashion to maintain the growing schedule throughout the season. Additionally, as machinery purchase costs continue to increase, capital efficiency must also be considered when making additional equipment investments.

To answer the call of increased seeding productivity, equipment manufacturers have continued to increase the working width of seeding drills with each new model. Today, seeding equipment with a working width of 30.5 m is produced by several equipment manufacturers prevalent in western Canada. In contrast, equipment designed 10 years ago was typically

less than 22 m wide, and most equipment produced 20 years ago was less than 15 m wide. A current-model seeding drill manufactured by New Holland Agriculture is pictured in Fig. 1.1. The particular machine shown has a working width of 18.3 m, and is available up to a width of 21.4 m.

Figure 1.1: A New Holland P2070 Precision Hoe Drill unfolded into the working configuration, with the bulk product air cart towed behind. Image credit: www.newholland.com.

While increased frame width has met the historical demand for greater productivity, practical limits to seeding implement size exist. The lateral spacing between planted rows is typically offered in only a few sizes regardless of implement width, so the draft force required to pull an implement through the field increases with working width. Thus, larger tractors are needed to pull wider seeding drills.

The hydraulic power demands of the implement also increase with working width. The bulk product air cart (towed behind the drill in Fig. 1.1) stores the seed and fertilizer before it is placed in the soil by the drill. Modern seeding implements use a pneumatic conveying system to transport seed and fertilizer to each seed row, hence the name "air drill" and "air cart" often used to describe the seeding implement and towed cart, respectively. As more rows are added to wider implements, the demand of the hydraulically-powered pneumatic system grows.

Maintaining the mechanical strength of the implement frame also becomes more challenging as it becomes wider as all towing force is transmitted through the hitch between the

tractor and the frame. Overall frame weight can become a design concern when excessive soil compaction occurs, in addition to increased material costs, and the manufacturing and logistical challenges associated with larger machinery.

Owning land conducive to operating wide equipment can be another purchasing barrier for potential customers. In order to utilize the increased working width effectively, terrain features may require modification. For instance, drainage paths may be altered, utility poles may be re-located, and areas of existing vegetation may be modified or removed entirely to enable larger equipment to be maneuvered through the field. However, these activities carry extra costs for the land owner.

In addition to the above challenges, equipment operators are often required to transport the tractor, seeding drill, and air cart ensemble on public roads to access the various fields to be seeded during the seeding season. Air drill frames have design features that allow the frame to be folded into a compact transport configuration, however the transport width often still exceeds the width of a standard traffic lane; for instance the published transport width for the P2070 Precision Hoe Drill is 5.4 m (New Holland Agriculture, 2010). While transport exemptions exist for agriculture equipment in Saskatchewan, strict transport regulations in other North American regions and Europe do present challenges to equipment designers. In general, moving the large equipment ensembles in regular high-speed traffic can be a stressful experience for the machine operator. Overhead clearance to power lines and overpasses along the travel route must be considered along with possible width restrictions.

A key aspect of air drill performance relates to the spatial consistency with which the seed and fertilizer products are sowed, in terms of both relative spacing between products, and proximity to the soil surface. If fertilizer is placed to close to the seed, chemical damage to the seedling can result, however it must be placed close enough to provide an agronomic benefit. Additionally, absolute seed depth is a critical agronomic factor in successful plant emergence, development and overall yield in several types of crops (Gan et al., 2003; Harker et al., 2012). Seeding too deep is a known contributor to root rot in some cereal grains (Government of Alberta Agriculture and Rural Development, 2002). Depth variation is also problematic when the choice of seeding depth is influenced by the depth of available moisture. "Seeding into moisture" is a common practice in western Canada, therefore, when the seeding implement

cannot reliably maintain the set depth, proximity to moisture may vary across the seeded area. Inconsistent depth within a field can cause plant development variation, so consistent seed depth is an important performance characteristic of modern seeding equipment.

While increasing the travel speed of the implement may increase apparent productivity, depth consistency can degrade above speeds of approximately 2.2 m/s (5 mph) with contemporary hoe-opener seeding technology. Figure 1.2 presents the relative emergence of canola planted at various speeds. The data, adapted from Canola Council of Canada (2014), were collected at multiple field sites during several crop years with a variety of field-scale equipment and soil-engaging-tool designs.

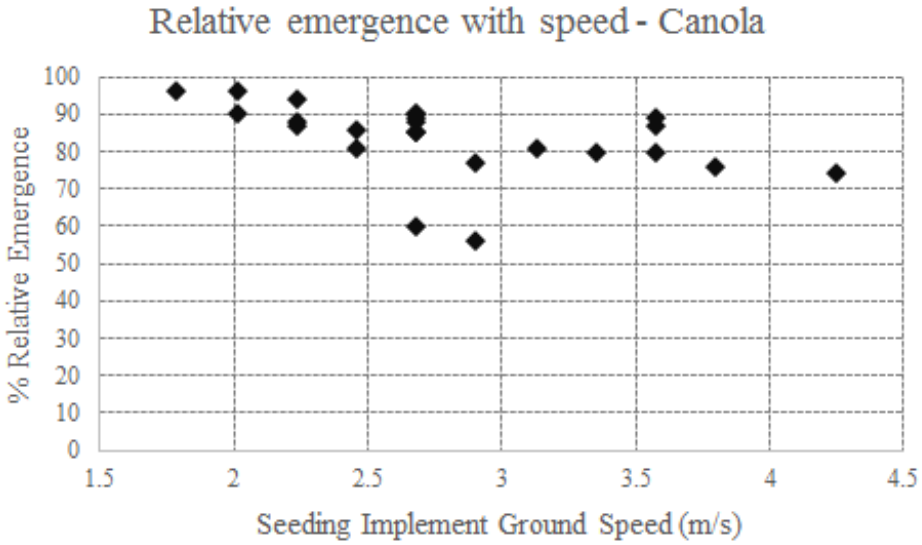

Figure 1.2: Relative emergence of canola is plotted against seeding speed. Data were collected at multiple field sites during several test years using a variety of field-scale equipment. Data adapted from Canola Council of Canada (2014).

Although many factors effect crop emergence, the general trend in Fig. 1.2 of reduced emergence at higher seeding speeds is consistent with the industry's current working hypothesis and may explain, at least in part, why increasing frame width has been the preferred approach to improving productivity. The top speed of hoe-drill style seeding equipment has not increased nearly as drastically as equipment size in recent years. A maximum seeding speed of 2.7 m/s (6 mph) is suggested for the New Holland P2070 model (New Holland Agriculture, 2010), however many operators commonly do not exceed 2 m/s in an effort to

maintain consistent seeding placement.

While there is an understanding amongst equipment operators and manufacturers alike of the depth consistency issues that arise with hoe drill technology at higher operating speeds, a more in-depth understanding of the cause of the excessive motion is desired. A greater understanding of the specifics of the mechanism(s) contributing to the motion of air drill components would benefit equipment designers, and ultimately end users of their products. Design guidelines have served manufacturers well in regard to maintaining operating speed accomplishments with design updates, however the ability to quantitatively predict the depth consistency performance of a given design has not yet been developed in the literature. As equipment prototyping and testing costs rise, and design and development schedules are shortened to maintain competitiveness, the need to "design in" key performance attributes from early stages in a project continues to grow.

1.2 Objectives

Due to the variability present in natural materials such as soil and plant residue, the value of having a model capable of predicting air drill motion to further augment interpreting measurement data was identified early in this research. A modelling tool could aid in both testing activities and future design evaluations, thus, developing such a tool was included as a goal of this research project from the beginning. However, to understand and quantify depth inconsistency that arises at higher ground speeds, a measured dataset that included poor depth consistency performance was also deemed valuable.

From these overall needs and desired project outcomes, the objectives of this research project were as follows:

1. Develop a mathematical simulation tool to be used in predicting the motion of a seeding implement in an agricultural field,

2. Measure the dynamic motion of a seeding implement when operating at several different speeds to record the dynamic behaviour as seeding depth consistency and excessive motion become problematic at higher ground speed,

3. From a combination of simulation results and measured data, identify the mechanism(s) that causes depth consistency problems at higher speed.

Project activities were based on the three objectives above, rather than the more traditional approach of Research Questions because of the general lack of prior implement dynamic modelling work in the open literature, as commented on in Section 2.2. Often, hypotheses and focused research experiments can only be formed once a preliminary understanding of the problem is gained. This work was driven by the need for that preliminary understanding. While objectives outlined above formed the concrete plan of how this project was to be executed, a goal of this work was to provide direction to the focus of future detailed research.

1.3 Outline of thesis

This thesis contains five chapters followed by references and appendices.

Chapter 1 briefly reviews the trends in the design of seeding equipment used in western Canada, the importance of plant emergence to growing healthy, profitable crops, and the deteriorating seeding depth consistency that results from operating current seeding technology at higher working speeds. The research objectives of the project were also stated.

Chapter 2 provides an overview of the specific model of seeding implement that was used throughout this research. This description is followed by a literature review of relevant prior work relating to modelling soil-tool interaction, soil-tire interaction, and past efforts in simulating off-road vehicle dynamics.

Chapters 3 and 4 are based on manuscripts to be submitted to the *Journal of Terramechanics* and *Transactions of the ASABE*, respectively, upon degree completion. To avoid duplication within this thesis, the background sections of both papers were removed and expanded to create the literature review of Chapter 2; save for this structural change for this thesis, the content of the manuscripts will remain largely unchanged when submitted to both journals.

Chapter 3 outlines the mathematical simulation tool developed during this research. Comparisons of simulation results to measured data are provided.

Chapter 4 presents the data collection activities related to measuring the dynamic mo-

tion of the seeding implement of interest while in operation. Data analysis techniques are presented, and interpretations of the measured data are discussed, along with supporting simulation results. The motion of the row unit during a sequence of video frames is presented.

Chapter 5 concludes the thesis, including limitations of the presented research and subsequent recommendations for future work.

The kinematic and kinetic equations of the simulation tool are included in Appendix A. Some of the data processing methods used to process the measured data are given in Appendix B. Symbols used throughout are listed in Appendix C.

Chapter 2

Background

An overview of the implement used during testing and modelling activities is presented. Initial familiarity with the various components and systems of the apparatus was beneficial in directing literature review efforts. The implement description is followed by a review of the literature pertinent to the interaction of seeding equipment operating on deformable soil.

2.1 Test apparatus overview

While many ground-engaging tools have been developed for varying tillage systems, seed types, and soil conditions, this work was restricted to hoe-style openers used commonly for seeding throughout western Canada. Seeding equipment mounted with these tools are commonly referred to as hoe drills and are produced in varying widths with the lateral distance between hoe openers generally ranging from 0.2-0.3 m. Often these machines are constructed from multiple frame sections to allow the machine to be folded into a more compact configuration for transportation on public roads. These frame joints also allow it to conform to varying terrain, as the pivoting degree of freedom (DOF) between sections remain when the implement is in the field configuration.

Separate of the hoe drill frame, the product cart containing seed and fertilizer to be seeded is towed behind the hoe drill frame, or between the tractor and the hoe drill. The bulk product cart is refilled as needed during the seeding operation, and a pneumatic conveying system is used to carry seed and fertilizer from this bulk storage location to each individual hoe opener. Details of the pneumatic conveying system were beyond the scope of this research. A typical field-scale setup is pictured in Fig. 1.1. The model shown is available in varying working widths from 15-21 m by modifying the number and size of wing frame sections connected to

the common center frame section.

A simplified version of a production-model P2070 Precision Hoe Drill manufactured by New Holland Agriculture (2010) was the basis of modelling efforts and data collection within this research project. The common center frame section of a production model hoe drill was used to construct a narrow testing drill used for seeding test plots by research and development staff at CNH Industrial - Saskatoon (CNH Industrial is the parent company of the New Holland Agriculture and Case equipment brands). Multiple views of the plot drill testing apparatus are shown in Figs. 2.1 and 2.2, and specific details of the components of the plot drill are outlined further.

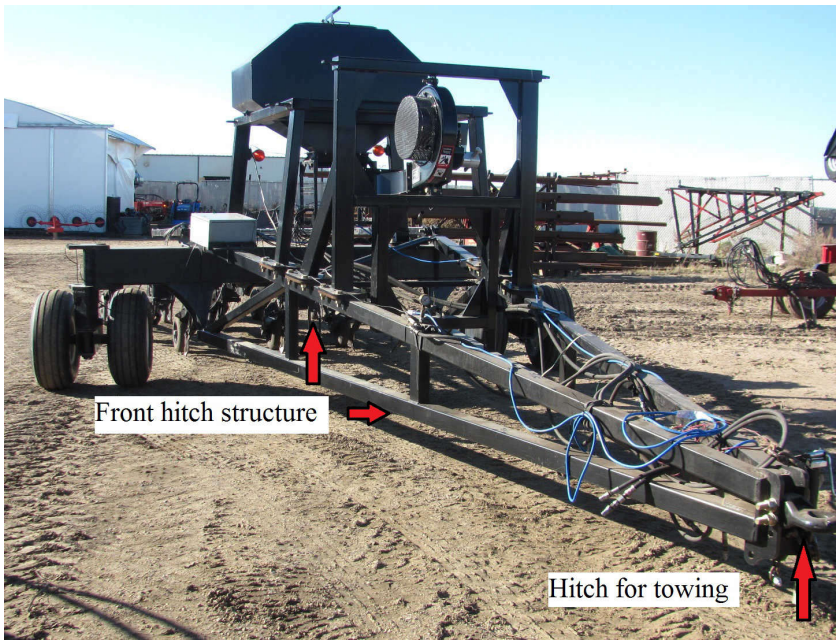

Figure 2.1: Front view of the plot drill. The testing rig was built from the center section of a production model P2070 Precision Hoe Drill.

The plot drill included a rigid structure connecting the large cross-section beam (the boom) to the hitch towing point at the right edge of Fig. 2.1. Attached to the boom were two sets of castering walking axles on both sides of the drill. The boom and one walking axle are visible in Fig. 2.2. The plot drill had twelve row units attached to a subframe that pivoted relative to the boom. The subframe along with the other supporting links formed two 4-bar linkage systems that connect the tail wheel at the rear of the plot drill to the boom at the front.

Figure 2.2: A side view of the plot drill. 3 ranks of row units are mounted to a subframe of the plot drill. 12 row units are mounted on the plot drill.

2.1.1 Row units

Unlike past generations of field cultivator design where tillage tools were directly connected to the frame via deformable C-shaped arms, current hoe drill technology features individual row units which move through curvilinear translation relative to the subframe to which they mount via a pair of equal-length parallel links. One of these row units is pictured in Fig. 2.3. Vertical motion (following an arced path) independent of vertical movement of the subframe is possible, however, the row unit is influenced by rotation of the subframe. The row unit was raised and lowered into field position by the operator-controlled row unit hydraulic cylinder; the pressure of this hydraulic circuit (common to all row unit cylinders) was regulated by one common pressure relief valve which can be set by the operator. Pressure was applied during operation to maintain the soil packing force applied by the packer wheel and to counter-act lift force generated by the hoe opener.

The vertical distance between the hoe opener tip and the packer wheel was adjustable on each row unit; this geometric depth setting was the only means of adjusting the seeding depth,

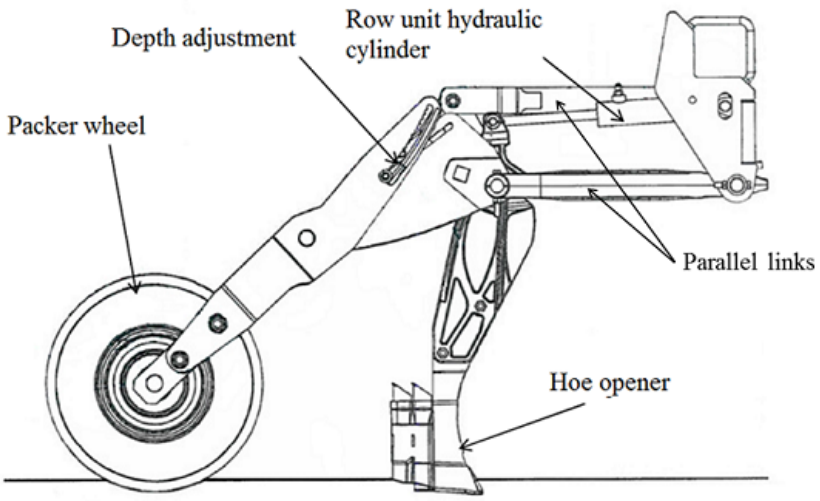

Figure 2.3: A schematic of a single row unit which attaches to the drill frame via two parallel links and a hydraulic cylinder. Direction of travel is to the right. Image provided by CNH Industrial.

but depending on the dynamic motion of the row unit, seeding depth was not guaranteed. Both the packer wheel and hoe opener are rigidly attached to the body of the row unit.

At typical seeding speeds, a furrow was created by the hoe opener where separate streams of seed and fertilizer were placed. A vertical and lateral separation between the two product streams is dictated by the location where the two products exit the opener. Soil flowed around the opener to cover the seed and fertilizer. The packer wheel followed directly behind the opener, compacting the soil a desired amount so that adequate soil-seed contact was achieved, which improved moisture and nutrient transfer to the seed. Soil compaction was influenced by the row unit hydraulic pressure setting selected by the operator. The profile of the opener is shown in Fig. 2.4 with the packer wheel visible in the background of the image.

To simplify the geometry of the opener attached to the row unit under evaluation, the opener was modified such that only one product stream could be placed in the soil. Normally the "winged" portion noted in Fig. 2.4 would be mirrored along the vertical mid-plane of the tool so that a second product stream could be placed. Pneumatic conveying and product placement were beyond the scope of this research, so this modification was deemed acceptable.

Figure 2.4: The profile of the opener is evident, with the packer wheel in the background. Note the slight bend in the opener creating a "winged" portion below the soil surface.

2.1.2 Front boom and subframe

The hitch used for towing the plot drill was rigidly connected to the front boom where caster walking axles were mounted. The tractor/hitch connection point is in the lower right corner of Fig. 2.1, and the boom connection with the castering walking axles is shown in Fig. 2.2. A product tank and air fan associated with the pneumatic conveying system were also connected to the front boom and hitch structure, but no product was being sowed so product delivery hoses and some air system components were not installed on the plot drill.

The subframe to which the row units connect was not rigidly connected to the front boom. Rotation of this subframe relative to the boom was possible due to pinned connections between the subframe and boom. This connection point is circled in Figure 2.5. On a production model drill with wing sections, this joint allowed the wings to be rotated upwards during transport. The connection also improved ground contour-following capability

of production models because upward motion of one tail wheel at the rear of the subframe (Section 2.1.4) did not cause other wing sections to rotate.

Figure 2.5: The front two ranks of row units are pictured. The pivot between the front boom and subframe is circled in red. This allows the subframe with row units to pivot separately from the front boom.

The twelve row units of the plot drill were attached to the subframe in three ranks (rows). The front ranks had three row units, the middle had four, and the rear rank had five row units. The front and middle ranks are shown in Fig. 2.5. The row units were spaced such that the furrows created by the drill were spaced 0.254 m (10 in.) laterally.

2.1.3 Walking beam axles

The plot drill was designed with castering walking beam axles that supported the front boom with a pair of wheels at each end. The walking ability reduced terrain displacement inputs to the frame. As seen in Fig. 2.6, this was achieved by offsetting the wheel axles from the walking axle pivot axis. However, this basic "suspension" design did not introduce additional damping or stiffness elements beyond the damping and stiffness characteristics of the walking axle tires. The vertical castering freedom of both sets of walking axles greatly increased lateral maneuverability. The walking axle tires used were 12.5L - 15 FI smooth highway implement tires, manufactured by Goodyear, Inc (Akron, OH).

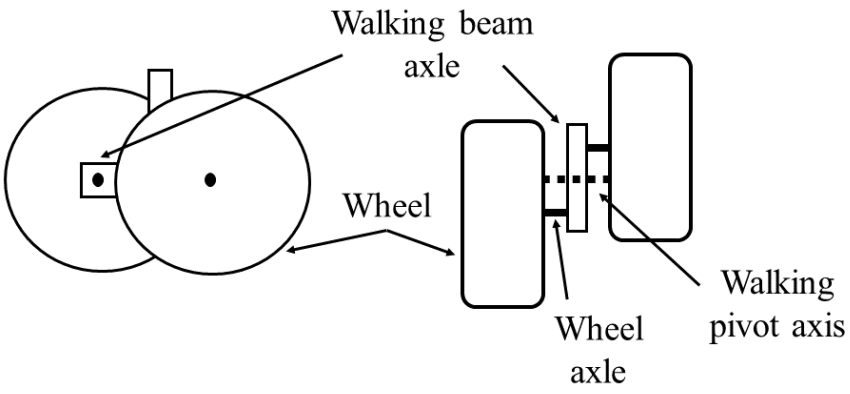

Figure 2.6: A schematic of the front boom walking axle wheel arrangement. Side (L) and top (R) view. The wheel axes are longitudinally offset from a central walking pivot axis. This feature reduced the vertical displacement of the boom when one walking axle wheel was displaced vertically.

2.1.4 Tail wheel

One large wheel supported the rear end of the subframe (size: 31 × 13.5 - 15). This tail wheel was connected to the subframe indirectly through linkages that located the wheel behind the subframe, pictured in Fig. 2.7.

Figure 2.7: The tail wheel supported the rear end of the subframe to which all row units mount. It connected to the subframe via a 4-bar linkage system.

Another frame connected the front boom to the tail wheel linkages and was positioned above the subframe (visible in Fig. 2.8). This top frame was part of a hitch structure for tow-behind air carts used with full-scale field equipment. The front boom, subframe, cart

hitch, and vertical support link pictured in Fig. 2.7 made up a 4-bar linkage system.

A second 4-bar linkage system connected the tail wheel to the subframe and vertical support link. The link indicated by the red arrow in Fig. 2.7 is normally adjustable on production models, and would be used to level the subframe if required.

2.1.5 Frame cylinder

A hydraulic cylinder between the front boom and subframe was used to modify the vertical force carried by the walking axle wheels, tail wheel and tractor hitch during field operation. This cylinder, pictured in Fig. 2.8, extended to effectively push the tail wheel downwards and lift the walking axle wheels; when in field operation the walking axle wheels remained in contact with the soil. This cylinder was used to ensure that the upward packer wheel and opener reaction forces did not lift the tail wheel off the soil surface.

Figure 2.8: The frame hydraulic cylinder extended between the front boom and the subframe. The pressure applied to this hydraulic cylinder changed the vertical load carried by the tail wheel, walking axle wheels, and tractor hitch. The large frame structure above the subframe was part of the production-model hitch system used to pull an air cart.

The frame hydraulic cylinder circuit pressure was controlled separately from the hydraulic circuit used to raise and lower the row units. The frame hydraulic pressure was set by the operator by means of a pressure relief valve mounted on the implement.

2.1.6 2-D representation

A 2-D schematic of the plot drill as viewed from the side is given in Fig. 2.9. Only three row units are shown for illustrative purposes. The hitch between the boom and tractor has also been omitted. The walking axle pivot point has been moved to directly beneath the boom. Two 4-bar linkage systems are evident in the figure. The first is comprised of the subframe, hitch for towing the product cart, hitch support link, and boom. The second linkage system connects the tail wheel to the rest of the frame via portions of the subframe and hitch support link, the tail wheel link, and tail wheel support link. While two linkage systems are present, they do not move independently; with knowledge of the dimensions of the machine and only one link angle, the positions of all other links can be determined mathematically.

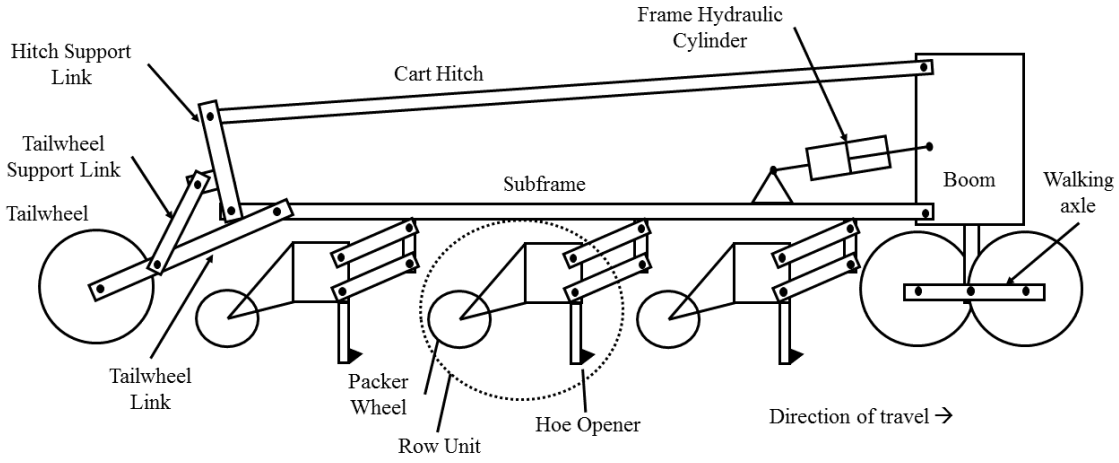

Figure 2.9: A schematic of the plot drill used during this research. Direction of travel is toward the right of the figure. The hitch to the tractor (right of boom) is omitted for illustrative purposes. The walking axle pivot point has been moved to directly beneath the main boom. The links above and the the left of the subframe are part of a hitch system for towing an air cart behind the plot drill.

2.2 Literature review

An initial literature search regarding the dynamic performance of agricultural tillage implements returned little research on the performance of tillage implements as a whole. However, given the historical importance of tillage in agriculture, significant effort has been directed toward understanding the interaction between soil and tillage tools. Additionally, the performance of off-road vehicles (both wheeled and tracked) has also received major attention from military, agricultural, construction and lunar exploration interests. Research focused on the dynamics of off-road vehicles has generally been related to improving operator comfort and reducing the vibration exposure of occupants of driven power units (tractors, forestry skidders, etc.). Little work on the the dynamics of towed implements was found in the open literature. Cowell (1969) investigated automatic depth control of a tractor-mounted plough implement through a hydraulically actuated control system with mechanical sensing elements, however equations were developed for a static operating situation. Dwyer et al. (1974) also investigated a draft control system including a stability analysis of the controller used. Unfortunately, dynamic equations of the apparatus were not presented; in general, the goals of both of these works did not align with the objectives of this research presented in Chapter 1.

Given the lack of literature pertaining directly to modelling and predicting the motion of towed implements, a logical starting point for this work was to survey the literature for modelling approaches that have been successfully used to mimic the physics the various mechanical elements of the plot drill, as well as methods to represent the contact between the machine and the deformable soil surface. Therefore, the majority of this research review pertains to soil-tool and soil-tire research, as well as previous dynamic modelling work related to tractor ride comfort vibration.

2.2.1 Soil-tool interaction

Much of the early soil-tool research was based on the premise that soils fail in a brittle manner according to the Mohr-Coulomb criterion (Coulomb, 1776), where the shear strength of the soil depends on the normal stress applied to the soil, given by σ. The shear strength of the

soil is given by

$$\tau_{soil} = c + \sigma \tan \phi, \tag{2.1}$$

where c is soil cohesion and ϕ is soil friction angle. Note: Appendix C contains a list of mathematical symbols used during this research.

The first widely-applied model of soil-cutting by wide 2-dimensional blades was based on Terzaghi's work on passive earth pressure and retaining walls (Terzaghi, 1943). Failure was assumed to result in a wedge of soil forming in front of the blade. The assumed soil failure surface was a logarithmic spiral which passed through the blade tip and extended to the surface. At the moment of soil failure, the model assumed that the maximum shear stress, τ_{max}, at all points along the failure surface equaled to τ_{soil} (i.e., at failure, $\tau_{max} = \tau_{soil}$). Forces acting on the 2-D blade react the stresses acting on the failure surface.

The calculation of soil forces on a 2-D blade was reduced to the addition of force contributions from gravitational, cohesive, adhesive, and surcharge components (Reece, 1964). This formulation is often deemed the fundamental earth-moving equation and defines the soil force on an loaded plane

$$P = \gamma d^2 N_\gamma + c d N_c + c_a d N_a + q d N_q, \tag{2.2}$$

where the N-factors are based on soil properties and blade geometry, d is the blade depth, γ is the soil density, and q is the surcharge pressure of loose soil above the failed soil wedge. Values for each N-factor were tabulated (Hettiaratchi et al., 1966). However, the model was based on a quasi-static force analysis of soil failure in front of the 2-D blade.

The development of a 3-D failure model was based on qualitative observations of narrow tines acting in different soils (Payne, 1956). It was observed that a wedge-shaped failure zone regularly formed immediately ahead of the blade, and an outer crescent-shaped failure boundary surrounded the wedge and extended beyond the sides of the tool. O'Callaghan and Farrelly (1964) expanded on these observations with the concept of a critical working depth that defined different modes of soil failure for *shallow* and *deep* tines based on tine aspect ratio. Soil failed only horizontally below the critical depth. Below the critical depth, soil failed only in a horizontal manner due to the presence of soil above the critical interface. For

a vertically oriented tool, the transition between shallow and deep modes was reported to occur when $\frac{d}{w} > \frac{1}{2}$, but the transition aspect ratio increased as the tool rake angle departed from the vertical. Because of this sensitivity to rake angle, the hoe-openers of the plot drill would not operate strictly in the *deep* working mode.

A failure model with simplified geometry (Hettiaratchi et al., 1966) was reported that was capable of predicting the rupture distance (distance between tool and front edge of failed soil). Other 3-D models (Godwin and Spoor, 1977) required prior knowledge of the critical depth or the rupture distance. These parameters would be established from physical testing of the blade operating in the soil of interest.

The model of McKyes and Ali (1977) did not require critical depth parameters. The geometry of this soil-tool interaction model is shown in Fig. 2.10. At the soil surface, the leading edge of soil failure is composed of circular crescents along lines AB and CD, connected by a straight line BC equal to the width of the blade. Straight lines extend from the tool tip (points G and H) to the extents of the failure crescents (points A and D). The shear stress acting on the soil failure surfaces (ABH, BCGH, and CDG) is assumed to be equal to τ_{soil} at the moment of soil failure. Stresses are integrated across the failure surfaces, and are reacted by the forces acting on the blade face.

With knowledge of soil parameters c, ϕ, and γ along with tool depth, width, rake angle (α), and soil-tool friction angle (δ), the draft and lift forces acting on the tool face can be directly calculated by minimizing the gravitational draft force term with respect to the surface angle (β). Soil-metal adhesion was neglected by McKyes and Ali (1977).

Zhang and Kushwaha (1995) minimized total draft force (including an adhesion contribution) to predict the failure surface angle (β). Minimization is used to determine β because the minimum strength of the soil determines when failure will occur. The N-factors of Eq. (2.2) presented in Zhang and Kushwaha (1995) are defined as:

$$N_\gamma = \frac{\frac{1}{2}(\cot\alpha + \cot\beta)(1 + \frac{2d}{3w}\sqrt{\cot^2\beta + 2\cot\alpha\cot\beta})\sin(\beta+\phi)}{\sin(\alpha+\delta+\beta+\phi)} \tag{2.3}$$

$$N_q = \frac{(\cot\alpha + \cot\beta)(1 + \frac{d}{w}\sqrt{\cot^2\beta + 2\cot\alpha\cot\beta})\sin(\beta+\phi)}{\sin(\alpha+\delta+\beta+\phi)} \tag{2.4}$$

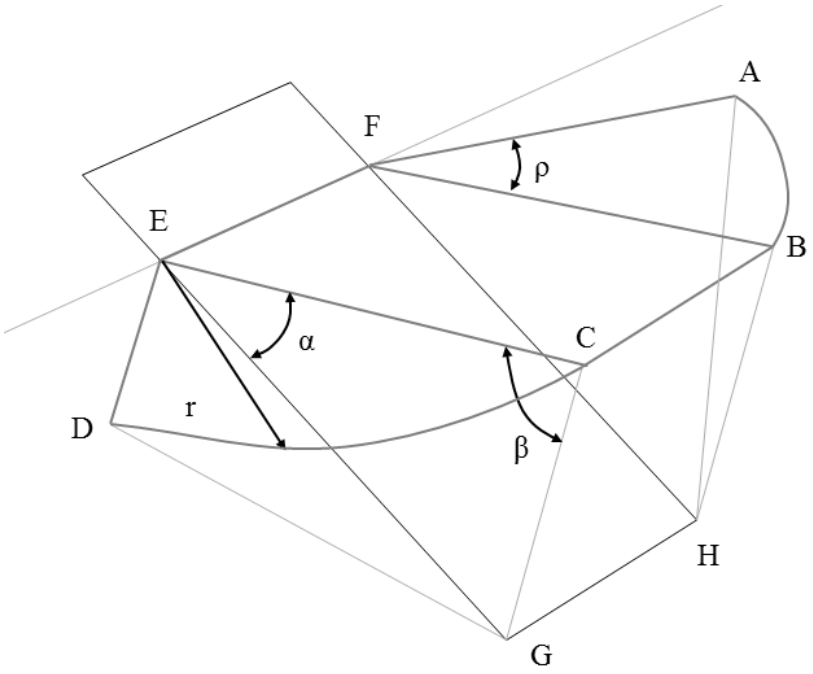

Figure 2.10: A diagram of the assumed soil failure geometry of the McKyes-Ali model. The tool surface is represented by EFHG.

$$N_c = \frac{\cos\phi(1 + \frac{d}{w}\sqrt{\cot^2\beta + 2\cot\alpha\cot\beta})}{\sin\beta\sin(\alpha+\delta+\beta+\phi)} \tag{2.5}$$

Neglecting adhesion, substituting the N-factors from Eqs. (2.3-2.5) into Eq. (2.2) gives the total force acting on the tool, P. The horizontal force (H) and vertical force (V) acting on the tool face were computed by

$$H = P\sin(\alpha+\delta), \tag{2.6}$$

and

$$V = P\cos(\alpha+\delta), \tag{2.7}$$

where α is the rake angle of the tool, and δ is the soil-tool friction angle.

Observations in early lab tests (Söhne, 1956; Olson and Weber, 1965) pointed to changing soil failure mechanisms with increasing speed. Stafford (1979) measured a logarithmic relationship between soil shear strength and strain *rate*. Dry soils and low speeds resulted in cyclical brittle wedge-shaped failures, while moist soils resulted in soil flowing around the

tool in a non-periodic manner. These failure modes were developed further based on critical state soil mechanics (Stafford, 1981). The effect of strain rate on soil shear strength (Stafford and Tanner, 1983a) and soil-metal friction (Stafford and Tanner, 1983b) were quantified for two soils. These works were combined to create mean draft and vertical force prediction models for brittle and flow failures (Stafford, 1984). Predictions were compared to test data with a demonstrated improvement compared to other contemporary models, however accuracy was reduced when the soil failure type was not distinct. The model was sensitive to soil strength and soil metal friction measurement methods which were far more complicated than standard direct shear (ASTM International, 2016) or triaxial compression soil tests (ASTM International, 2011a,c,b).

High-speed draft measurements up to 18 m/s were reported for field soils near Saskatoon, SK (Kushwaha and Linke, 1996). A critical speed range of 3-5 m/s was observed. Above the critical speed, draft increased less with increased speed. No draft-speed regression was published, but a logarithmic relationship similar to Stafford (1984) appeared appropriate given the logarithmic trend of the data presented. The reduction in specific draft (draft/speed) at the higher operating speeds presents a potential of power savings by operating tillage equipment at higher speeds. Given that current seeding speeds (< 2.5 m/s) are below the identified range of critical speed, power savings could potentially be realized if seeding was performed at a higher speed.

Wheeler and Godwin (1996) developed a predictive model with velocity effects based on the crescent failure model of Godwin and Spoor (1977). However, this model again requires prior knowledge of the rupture distance between the tool and the failure front along the soil surface.

The spectral content of draft and vertical tillage forces was investigated by Upadhyaya et al. (1987). Time-varying draft forces were accurately reconstructed using only 10 fast Fourier transform (FFT) coefficients, and the failure pattern was sensitive to soil type, moisture, density, and tool speed. Others reported that the majority of draft/vertical force variation below 3 Hz was attributed to spatial variation of soil strength in dense clay (Owen et al., 1990); significant frequency peaks were often present between 5-10 Hz. Tool depth did not significantly affect draft and vertical force frequency peaks. These works were some of

only a few papers found that quantified the time-varying nature of tillage forces. But, to their credit, authors of the classical models have acknowledged that the predicted forces by analytical models are the maximum values required to create the give failure plane; time-varying forces do result during actual tillage.

The finite element method (FEM) has been applied to 3-D soil failure from narrow blades (Chi and Kushwaha, 1989). An assumed failure shape was not imposed, and greater tool shape complexity was possible. A Duncan-Chang constitutive non-linear soil stress-strain relationship was used and soil strength was based on the Mohr-Coulomb failure criterion. Varied tool geometries including bevel-edged tines with soil-tool adhesion terms using a hyperbolic soil stress-strain relationship (Chi and Kushwaha, 1991), and curved blades (Chi and Kushwaha, 1993) were analyzed. Strain-rate material sensitivity was analyzed by FEM (Kushwaha and Shen, 1995) and compared to field data. Average draft was underpredicted up to 17 m/s but the magnitude of prediction was appropriate. Armin et al. (2014) modelled soil-tool interaction using FEM, and developed a method of representing separation between mesh nodes as the tool cut through the soil.

Although relatively new in comparison to the classical tool models and FEM approaches mentioned earlier, the discrete element method (DEM) has been applied to computing the reaction forces acting on various types of tillage tools with promising results. In this modelling approach, interactions between individual soil particles are represented through a combination of stiffnesses, damping, and friction; Shmulevich (2010) provides a review of various contact models from the literature. Reactions against soil container walls and other bodies (tillage tools, excavator blades, etc.) are also represented enabling the calculation of draft and vertical forces on tools of arbitrary shape. Shmulevich et al. (2007) developed a 2-D DEM model of a dozer blade in cohesionless soil using 15,000 soil particles within a simulated soil bin 0.45 m long by 0.13 m deep. Maximum error between simulated and measured draft energy was 12%. Obermayr et al. (2011) modelled the interaction of a dozer blade with soil using model parameters that were determined by first calibrating a simulated tri-axial compression test to measurement data. A similar approach was used by Tamás et al. (2013) where measured shear box test results were replicated with a tri-axial DEM simulation. The subsequent simulation of an agricultural tillage tool agreed with measured data within 12%

over a speed range from 0.5-2.4 m/s. 30,000 particles were used to represent the soil bin.

While the results of additional research employing DEM to study and improve tillage tools are encouraging (Chen et al., 2015; Sadek and Chen, 2015; Mak et al., 2012), several challenges exist when implementing the method. A major criticism is that no standardized method exists to relate measurable macro-scale parameters (i.e., cohesion, friction angle) or tool response (i.e., draft and vertical forces, resulting deformed terrain) to the micro-scale particle interaction parameters needed to populate a DEM model (Shmulevich, 2010). Additionally, computational time is significant; Tamás et al. (2013) reported a 32 hour run time to complete a single simulation of a tillage tool operating at a fixed depth through a soil bin 1 m in length using a modern computer.

2.2.2 Off-road vehicle dynamics and soil-tire interaction

Terramechanics and off-road vehicle dynamics research dates prior to the 1950s, with vehicle traction and soil compaction both being popular topics. Initial research also focused on relating simple cone index measurements to the trafficability of a given soil; in-situ soil measurements were used to define go/no-go operating ranges by U.S. Army Corps Engineers for heavy military equipment in off-road environments (Bekker, 1969).

Work has focused on describing local terrain properties, with a vertical soil penetration relationship proposed by Bernstein (1913) and Goriatchkin et al. (1936) where the nominal pressure (p) acting on a plate penetrated to a sinkage depth (u) was expressed by

$$p = ku^n, \tag{2.8}$$

where k and n are determined from empirical data. Prominent work by Bekker (1956, 1960, 1969) and (Wong, 1978, 1989) further developed this semi-empirical relationship into the form still in use today

$$p = (k_c/b + k_\phi)u^n, \tag{2.9}$$

where k_c and k_ϕ are determined from empirical data, b is the smaller dimension of the loading area (plate diameter or narrow plate width) (Bekker, 1969). By expanding the leading coefficient to the form presented in Eq. (2.9), the sensitivity to the size of the soil loading

area used during data collection is reduced. Using this form with two leading coefficients requires data collection with at least two different plate sizes.

To quantify a tire's tractive capability in a given soil, knowledge of the shear strength properties of the soil were required. A popular semi-empirical description of the shear strength-displacement relationship was developed by Janosi and Hanamoto (1961). The shear stress, τ, along the failure surface beneath a shear plate with grousers (lugs) resulting from lateral displacement under vertical load was described by

$$\tau = (c + \sigma \tan \phi)(1 - e^{(-j/K)}), \tag{2.10}$$

where K is the the shear deformation coefficient determined from empirical data, and j is the linear or angular displacement of the plate. K is determined by applying a static vertical load to a linear (or annular) shear plate while measuring applied the force (or torque) and displacement of the plate. The leading bracketed term in Eq. (2.10) is the Mohr-Coulomb failure criterion (Eq. (2.1)) as applied to the situation beneath a tire on soil; brittle failure was the assumed mode of failure in this representation of soil-tire interaction.

If a shear plate with lugs is used and failure occurs on a plane between the lug tips, data fit with Eq. (2.10) would describe the shear stress along that failure plane. However, if the friction relationship between a smooth tire and the soil is of interest, then the testing apparatus would need to be equipped with a rubber-faced shear plate with rubber characteristics equivalent to those of the smooth tire being modelled, and c and ϕ are replaced with c_a (soil-tire adhesion) and δ (soil-tire friction angle) in Eq. (2.10) (McKyes, 1989). Alternatively, simpler approaches have used a friction coefficient to describe soil-tire friction (Harnisch et al., 2005).

With the vertical pressure-sinkage and shear strength-displacement relationships defined, forces acting on the tire can be determined through integrating the appropriate components of soil-tire contact stress across the contact area of the tire. When the inflation pressure of the tire is greater than the contact pressure of the soil, the treadband of the tire is often assumed rigid (Wong, 1989). A model of the forces acting on the rigid treadband is shown in Fig. 2.11.

To compute the wheel center force reactions F_x, F_z, and wheel center torque, T, for a

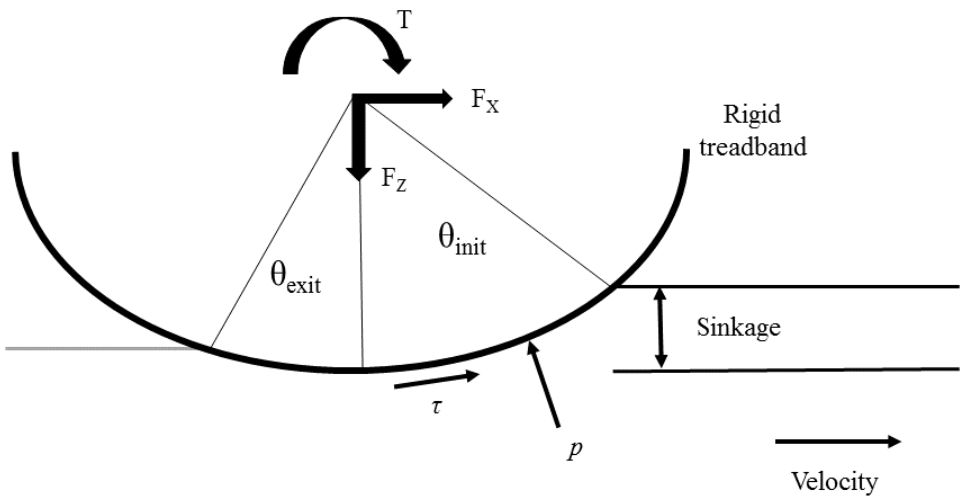

Figure 2.11: A diagram of forces acting on a rigid tire in the Bekker-Wong soil-tire interaction model.

tire of radius R and width b, the corresponding components of the stress distributions $p(\theta)$ and $\tau(\theta)$ are integrated. In the Bekker-Wong soil-tire model, it is assumed that the pressure acting on the tire treadband is equivalent to the pressure acting on a rigid plate at the same sinkage depth. For a flat soil profile, sinkage can be parameterized by angular position on the treadband by

$$u(\theta) = u_{max} - R(1 - \cos\theta) \tag{2.11}$$

where u_{max} is the maximum sinkage of the tire (occurring at th bottom-dead-center point for flat terrain). The normal and shear stress distributions, $p(\theta)$ and $\tau(\theta)$, can be determined based on this parameterization. Pressure acts normal to the treadband surface, and shear stress acts tangentially. The longitudinal and vertical reaction forces are calculated, respectively, by

$$F_x = bR \int_{\theta_{exit}}^{\theta_{init}} \Big(\tau(\theta)\cos\theta - p(\theta)\sin\theta\Big) d\theta, \tag{2.12}$$

and

$$F_z = bR \int_{\theta_{exit}}^{\theta_{init}} \Big(p(\theta)\cos\theta + \tau(\theta)\sin\theta\Big) d\theta, \tag{2.13}$$

where b and R again are the tire width and radius, respectively. For driven or braked wheels, the reaction torque T can also be computed.

When a vertical load is applied to soil, permanent deformation often results; for example, as a tire rolls across a soil surface a rut will remain once the wheel has passed if stresses exceed the elastic limit of the soil. The depth of the remaining rut is dependent on both the load being applied to the tire and the characteristics of the soil being considered. Along with the pressure-sinkage relationship of Eq. (2.9), an example of this soil unloading is shown in Fig. 2.12 based on work presented by Wong (1989). The red dashed line is an example of the Bekker-Wong pressure-sinkage relationship of the soil while increasing pressure is applied from *1* to *2*. If pressure is removed at *2*, an approximated pressure-sinkage during unloading is given by the dashed blue line from *2* to *3*. If load is then reapplied, the pressure sinkage curve *3-4* is first traversed, then the pressure-sinkage relationship then continues to be described by Eq. (2.9) along the red dashed line. If a soil region is only loaded and unloaded once, the plastic (permanent) deformation is described by the sinkage distance between points *1* and *3*.

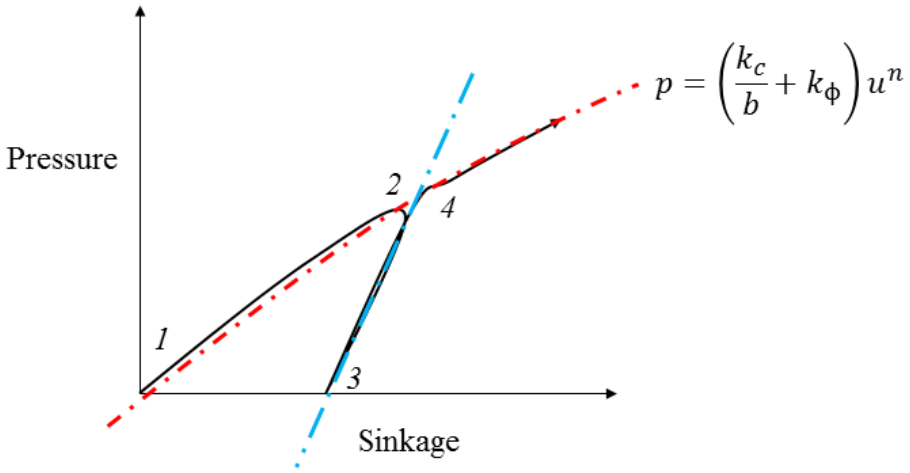

Figure 2.12: A pressure-sinkage digram of a soil during loading (1-2), unloading (2-3), and reloading (3-4...), based on Wong (1989).

Wong (1989) approximated the slope of the blue dashed line in Fig. 2.12 by a linear function of the maximum sinkage before unloading occurred, namely

$$k_{unload} = A_o + A_k u_{max}, \tag{2.14}$$

where A_o and A_k are soil unloading parameters. Therefore, in flat terrain the sinkage pressure

of the soil that is experiencing unloading along the rigid treadband is given by

$$p(u) = p_{max} - k_{unload}(u_{max} - u), \tag{2.15}$$

where p_{max} is the pressure at the point of greatest sinkage – located at the bottom dead center point of the treadband for flat terrain. Therefore,

$$p(u) = (k_c/b + k_\phi)u_{max}^n - k_{unload}(u_{max} - u), \tag{2.16}$$

where $u = u(\theta)$ from Eq. (2.11). The last point of contact is described by θ_{exit}; it is assumed that the soil being unloading cannot experience tension, therefore, θ_{exit} corresponds to the point where Eq. (2.16) becomes 0. The semi-empirical Bekker-Wong model has become the foundation of most semi-empirical soil-tire interaction models used today (Taheri et al., 2015).

Due to the limitations of a semi-empirical tire representation, research has also focused on advanced methods for modelling soil-tire interaction physics in a variety of soil types. Yong and Fattah (1976) presented an early soil-tire FEM model. Tires were simplified to semi-flexible rings with plane strain. Fassbender et al. (1997) explored FEM tire representations in a dynamic model using the Drucker-Prager constitutive model to represent soil material properties. Modelling approaches including both 2-D FEM and DEM in combination (Nakashima and Oida, 2004) have been developed to more accurately represent soil deformation and failure (using DEM) while including deformation of the tire (using FEM). Zhao and Zang (2014) presented a 3-D FEM/DEM approach to capture aspects of 3-D soil deformation (i.e., soil bulging beside the track of the tire), but noted a solving time of 96 hours for a 1.3 m long simulation at one tire slip condition.

To reduce complexity, the lumped stiffness/mass tire was used with DEM representation of the soil particles (Wakui and Terumichi, 2011). The Hybrid Soft Soil Tire Model (HSSTM) represents the tire sidewall and face as masses connected by multiple (non-) linear spring-damper assemblies. Tire properties are collected from several sources including static and rolling cleat tests, modal analysis, and FEM results (Taheri et al., 2015).

Given the computational complexity and cost of FEM and DEM approaches, modifications the the Bekker-Wong soil-tire model continue to be developed. Grahn (1991) proposed a

multiplication of Eqn. (2.9) by a power of the sinkage velocity, where sinkage velocity was defined as the vertical velocity component of a rigid rolling treadband. This velocity-dependent relationship was of the form

$$p = k_o u^n \dot{u}^m, \tag{2.17}$$

where $\dot{u}$ is the vertical component of the sinkage velocity, and m is determined experimentally.

Rubinstein and Hitron (2004) proposed an additive component of sinkage pressure linearly proportional to the vertical velocity of a track link. The AS^2TM model (Harnisch et al., 2005) applied the Bekker model and critical inflation pressure calculations (Wong, 1989) to create a model with slip-sinkage, tire-lug interaction, and multi-pass soil compaction capability. Traction and slip-sinkage prediction agreed with measurement data.

Describing and predicting the mechanics of tire deformation continues to be an ongoing field of research. Similar to the varying descriptions of soil-tire interaction, models of tire deformation span the spectrum of complexity. The most basic model often used to describe only vertical tire deflection is a parallel spring-damper combination (Kelvin-Voigt element). To understand the radial stiffness and damping characteristics of an agricultural tractor tire, Lines and Murphy (1991a,b) experimentally measured these parameters on a variety of tractor tires in static and rolling conditions. Generally, both the stiffness and damping of a tire decrease once rolling begins. Above speeds of 1.7 -2.8 m/s the sensitivity of vertical stiffness to speed decreased. Lines and Peachey (1992) used a simply-suspended one-wheeled vehicle for dynamic tire data collection. The vertical response was modelled with parallel spring and damper elements. The data were then used to simulate the motion of a simple unsuspended vehicle; results were compared to measured data. Simulated root-mean-square (RMS) acceleration was less accurate in comparison to the measured simple vehicle response. Frequency peak prediction was improved with the use of dynamically-measured tire properties. Crolla et al. (1990) used a spring and viscous damper acting in parallel to model the vertical response of tractor tires, and proposed a spring and damper in series (Maxwell element) to represent the lateral and longitudinal response of the tires. Initial agreement to measured vibration response was improved by using a Maxwell element in the lateral and longitudinal directions.

Measured tire parameters were further used to model the ride vibration of a full agricultural tractor model (Lines et al., 1992); comparisons to measured data indicated good agreement between the vertical and roll DOF acceleration quantities. Due to small angles of rotation experienced by the tractor during operation, the pitch, heave, and longitudinal motion were modelled independently from roll, yaw, and lateral motion in the full tractor model (Stayner et al., 1984).

Park et al. (2004) simulated three configurations of 1/4 car models of varying complexity including a linearized deformable soil and compliant tire representation. Based on these results, tire deflection was found to be an important contributor to the dynamic motion even when the tire is much stiffer than the ground. Ground profiles were generated through the inverse FFT of the off-road profile spectrum. Body and wheel position were found to vary less as ground stiffness was increased. Although rigid wheels and treadbands spatially filter the vertical tire inputs, this filtering effect in the frequency domain were not analyzed.

Extensions have been made to 3-D full-tractor models including the operator seat suspension system (Ahmed and Goupillon, 1997), again through the use of spring-damper elements acting in the various directions of seat suspension compliance. Model prediction correlated well with measured acceleration of the tractors rigid body. Predicted seat accelerations were less accurate, and soil deformation was not considered.

Dynamic modelling efforts with simple mechanical elements have helped in the evaluation and parameter selection of suspension solutions for forestry equipment. Pazooki et al. (2011) developed a dynamic model of a forestry skidder with 13 DOFs to explore the effect of adding rear axle suspension to reduce operator vibration exposure. Soil deformation was not directly modelled. Reasonable agreement between predicted and measured vibration performance was achieved in the vertical, roll, and pitch DOFs of the main body of the skidder. The addition of a rear-axle suspension system provided a measured reduction in operator vibration exposure.

Advanced modelling techniques have been employed to create models of tire deformation with much higher fidelity than the rigid ring approach that is often used in basic semi-empirical soil-tire modelling. Tire lugs (grousers) and varying tire construction methods result in tire deflections that cannot be accurately described by basic spring/damper tire models. For example, the commercially available *Ftire* model (Cosin Scientific Software,

2014) used a flexible, extensible ring representing the treadband which connected to the wheel using distributed stiffess in the radial, lateral, and tangential directions. The effects of damping and hysteresis were included. However, advanced models like *Ftire* require significant data collection efforts to parametrize a specific tire; 24 separate tests were suggested by the developers (Cosin Scientific Software, 2016); other advanced models used modal analysis techniques in addition to some of the test modes of the *Ftire* model.

2.2.3 Summary

While using DEM to compute forces acting at both the soil-tool and soil-tire interface represents the state of the art in modelling, the advanced complexity, necessity of collecting significant experimental data for model calibration, and excessive computational time of this approach precludes its application in this research, given the objectives outlined in Section 1.2. This approach, while potentially the most accurate available, does not lend itself to exploring the performance sensitivities of design variables early in the prototype development process. Similarly, advanced tire models such as *Ftire* present a high-fidelity, but high-cost approach to representing tire deflection that does not align with the goals of this work.

As an initial starting point for model development, the semi-empirical approach of the Bekker-Wong soil-tire interaction model using the rigid treadband approximation appeared to be a reasonable approach to representing contact between the tires of the plot drill and the deformable soil. To represent soil-tool contact, the 3-D analytical model of McKyes and Ali was deemed as a reasonable starting point to compute the forces acting on the hoe-opener without significant prior knowledge of soil-tool interaction parameters such as rupture distance.

Chapter 3

Development of a dynamic simulation model of a towed seeding implement

Ian W. P. Paulson, Allan T. Dolovich, Scott D. Noble

This chapter contains a manuscript describing the development of the dynamic model of the plot drill intended to meet Objective #1 of Section 1.2. An earlier version of the manuscript without simulation results and interpretations was presented to the International Society for Terrain Vehicle Systems (ISTVS) at *The ISTVS 8th Americas Conference* in Detroit, MI, in September, 2016 (Paulson et al., 2016). A similar version of the following manuscript was subsequently invited for submission to the *Journal of Terramechanics* Agriculture and Forestry special issue. The submission is also titled "Development of a dynamic simulation model of a towed seeding implement"; the manuscript was still under peer review at the time of thesis completion. This journal is published on behalf of the ISTVS. Relevant previous literature along with a description of the plot drill were condensed from Chapter 2 and inserted into Section 3.2 below.

The dynamic simulation tool was developed and programmed by the lead author. Prof. A. Dolovich provided guidance regarding modelling techniques, along with editorial contributions. Prof. S. Noble contributed guidance to the paper structure and writing approach along with editorial contributions.

3.1 Introduction

Modern farming operations are continually looking for ways to reduce operational costs and increase time and capital efficiency while improving the end product. Naturally, equipment

manufacturers are also looking to increase equipment productivity. This is particularly evident in seeding technology changes over the past several decades. Seeding equipment as wide as 30 m is commonly available in Canada today; equipment developed two decades ago was typically no wider than 15 m. However, factors such as the mechanical strength of the frame, public roadway size restrictions, field layout, and available tractor power present challenges to future width increases. Therefore, productivity gains from increased seeding speed are increasingly important. However, with increased ground speed, current seeding technology typically exhibits excessive dynamic motion which is detrimental to consistent seeding depth, hence the trend of past productivity gains through wider equipment.

Taking lessons from the automotive industry, the ability to simulate the dynamic performance of a given vehicle design and to quickly compare many potential design configurations has led to drastically shorter development schedules and lower development costs. Simple models with reduced degrees of freedom and ideal representations of mechanical elements have become useful tools in understanding parameter sensitivity and eliminating underperforming designs. An example of a simple model is the bicycle model used for simulating handling performance (Jazar, 2013).

While seeding implements take a much wider array of configurations compared to the fairly standard automobile layout, simplified dynamic models of towed seeding implements capable of evaluating the dynamic performance characteristics are lacking in the literature. This work aimed to take basic first-principle and semi-empirical models of the various elements of a seeding implement (tires, tillage tools, etc.) and combine these sub-models for use in the dynamic simulation of a hoe-opener type seeding drill, a seeding implement common throughout western Canada. The purpose of the model is calculate the kinematic and kinetic response of a towed seeding implement as it passes over field terrain while the tillage tools are engaged.

The structure of the paper is as follows: Section 3.2 reviews background information on the effects of poor seed depth consistency, past off-road dynamic modelling efforts, applications of the Bekker soil-tire interaction model in dynamic modelling, soil-tool interaction models appropriate for low-cost computation, and the specifics of the machine being modelled. Section 3.3 covers data collection activities involved in this research, and the short-

comings of interpreting operational data without understanding system sensitivities. Section 3.4 explains the sub-models used to represent soil-tire and soil-tool interaction. Section 3.5 explains the model calculation structure and highlights some specific challenges in robust numerical modelling. Section 3.6 compares simulation results to test data with a discussion of the limitations of the model, and Section 3.7 concludes.

3.2 Background

For presentation in this thesis, the background section of this manuscript was expanded and moved to Chapter 2. As the model requires the representation of soil-tool and soil-tire interactions as the plot drill moves through the field, the reader should be familiar with Section 2.1 and 2.2.

3.3 Testing and data interpretation

As part of the broader research project, operational data were collected with the plot drill. Independent operating variables of interest were ground speed, hydraulic pressure, and the geometric depth setting of the row unit. To understand the performance of the equipment across a wide range of seeding speeds, including high-speed performance, four test speeds were chosen: 1.1, 2.2, 3.3, and 4.4 m/s. Typical seeding speeds are below 2.5 m/s.

A variety of operational responses were measured including acceleration of the row unit and frame near the tail wheel. The relative angles between the top row unit link and the subframe, and between the subframe and boom were measured. An inertial measurement unit (IMU) was mounted on the boom and measured acceleration and angular velocity with respect to a coordinate system fixed to the plot drill. Details regarding the experimental work are presented in Chapter 4.

Acceleration data were analyzed through the calculation of power spectral density (PSD) from steady-state operating data. PSDs were generated using Welch's Overlapped Segment method (Welch, 1967) with 50% overlap and 0.25 Hz resolution. Figure 3.1 presents an example of PSDs of row unit and boom vertical acceleration at a hydraulic pressure of 5500

kPa and a depth setting of 25 mm, at 2.2 and 4.4 m/s.

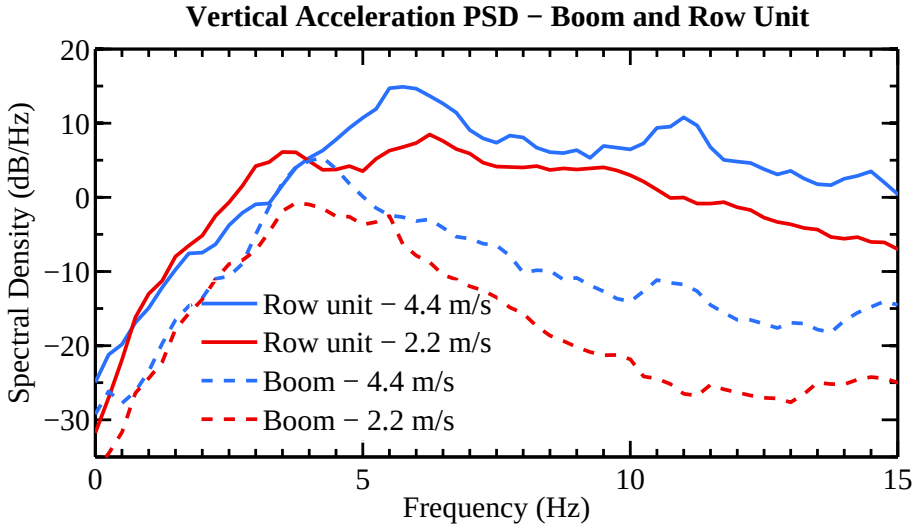

Figure 3.1: Power spectral densities of measured vertical vibration of the row unit and boom at 2.2 m/s and 4.4 m/s when operating at 5500 kPa hydraulic pressure and 25 mm operating depth.

Obvious qualitative differences can be identified from the PSDs in Fig. 3.1. At both sensor locations, vibration power is more than twice as large at 4.4 m/s versus 2.2 m/s across most of the frequency range. In general, the vibration power of the row unit is greater than the frame. The row unit has two distinct peaks at approximately 6 Hz and 11 Hz at 4.4 m/s whereas two peaks are present at approximately 3 Hz and 6.5 Hz at 2.2 m/s. The main peak of vertical boom vibration occurs at approximately the same frequency at both operating speeds. Higher-frequency vertical frame peaks (11 Hz and 14.5 Hz) present at 4.4 m/s are indistinguishable at 2.2 m/s. Further work could be focused on quantifying differences across the other test variables, developing regression models, etc. However, distilling *why* these changes occur and *how* system parameters (tire stiffness, geometry, hydraulic characteristics, etc.) are related to a specific response feature strictly through data collection and analysis has practical limitations. The response changes may be due to both characteristics of the inputs to the system, and/or non-linear response of the system itself.

Without a physical model, identifying the cause of these changes is challenging. Demanding testing standards may be required to confidently quantify input-response relationships if using only physical testing; depending on the natural variability of the test environment, the

required level of repeatability may not even be achievable. Additionally, the cost of designing and manufacturing prototype parts can be prohibitive. This is not to discredit discovery made by experimentation, but only to highlight the cost of physical prototyping and the limitations of data interpretation without deeper knowledge of the system itself.

3.4 Model characteristics

With the value of an analytical model of the plot drill system established, the specifics of the model developed are outlined in the following section. The developed model computes the motion of the plot drill as it passes over varying terrain while the hoe-openers are contacting the soil.

Newtonian-mechanics-based free body diagrams (FBDs) were developed for a 2-D simplification of the plot drill. This simplified 2-D configuration was shown in Fig. 2.9, and is repeated in this section for convenience in Fig. 3.2. As shown in the figure, only three row units were included in the model: one at each rank position along the length of the subframe. The FBDs and derived force/moment equations developed can be found in Appendix A.

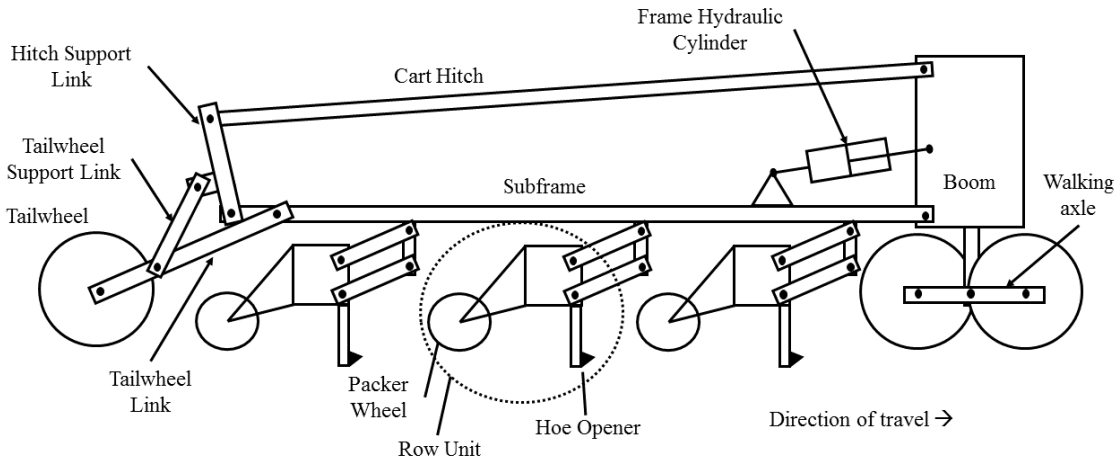

Figure 3.2: The plot drill schematic used to develop the dynamic simulation model. Direction of travel is toward the right of the figure. The hitch to the tractor (right of boom) is omitted for illustrative purposes. The walking axle pivot point has been moved to directly beneath the main boom. The hitch and support link annotated above refer to the hitch typically used to tow the product cart behind the hoe drill.

Based on initial qualitative analysis from the measurement video and typical equipment

motion observed during operation, the vertical and pitching motion of the plot drill were of primary interest. One walking axle was repositioned directly beneath the center of the boom, and forces at the walking pivot were scaled because only one walking axle was used, rather than scaling components' masses. The front hitch structure was lumped with the boom, and the motion of the hitch/boom was restricted to a vertical DOF. The subframe pivots relative to the boom via a rotational DOF. The row units were connected to the subframe by equal-length parallel links. In summary, the geometric DOFs of the model were

1. Vertical translation of the boom,
2. Front walking axle rotation,
3. Subframe rotation, and
4. Link angle rotation of each row unit included in the model.

The non-linear geometry of the 4-bar linkages of the main frame (refer to Sec. 2.1.6) was solved externally to the main kinematic and kinetic equations of the model. Newton-Raphson iteration was used to first find the position of the links immediately above and to the rear of the subframe. A 2^{nd} Newton-Raphson iteration scheme then calculated the position of the rear 4-bar links using the solution to the 1^{st} iteration. Compartmentalizing the geometry calculations allowed for modification of drill geometry without altering the equations of motion of the plot drill.

The tire reaction forces and hoe opener reaction forces were applied forces in the system FBDs and were calculated separate from the system of governing equations. This allowed for future improvement to the soil-tire and soil-tool models without drastic modifications to the governing equations to which these components attached. This approach allowed for the potential of coupling to other software suites should FEM or DEM representations of soil-contacting components be investigated.

3.4.1 Hydraulic forces

The frame and row unit hydraulic cylinders noted in Figs. 2.3 and 3.2, respectively, were represented as a constant force ($A_{cylinder} \times P_{hydraulic}$) applied in opposite directions to the

mounting points of each cylinder. Dynamics of the hydraulic system were deemed beyond the scope of this modelling work.

3.4.2 Soil-tire model implementation

Similar to basic tire models in the literature (Lines and Murphy, 1991a,b; Ahmed and Goupillon, 1997), the tire was modelled with vertical sidewall deflection represented by a non-linear spring with stiffness κ_{TIRE} in parallel with a viscous damper with damping coefficient c_{TIRE}. Cornering stiffness, and lateral and longitudinal compliance were not considered because of the primarily straight-line operation of a seeding implement. The stiffness and damping parameters are given in Table 3.1. A schematic of the tire model is given in Fig. 3.3.

Table 3.1: Values of tire parameters in model. As the tire stiffnesses were non-linear with deflection, the values given are the stiffnesses at the static deflection.

Tire	Stiffness (N/m)	Damping (Ns/m)
Walking axle wheel	407,300	3250
Tail wheel	394,700	4250
Packer wheel	84,800	400

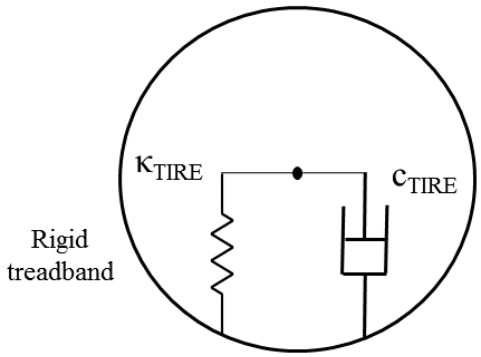

Figure 3.3: The simple model of vertical tire compliance. The vertical stiffness of the tire is represented by a non-linear spring, κ_{TIRE}, in parallel with a viscous damper, c_{TIRE}.

As outlined in Section 2.2.2, the Bekker-Wong model with an assumed rigid tread band was selected to represent soil-tire interaction, based on its application in a variety of modelling

examples summarized by Taheri et al. (2015). The treadband was discretized into segments of equal horizontal length to facilitate the discrete calculation of vertical sinkage and resulting pressure. Forces acting on the treadband are described in Fig. 3.4. In the horizontal direction, the rolling resistance due to sinkage was reacted at the wheel center. The vertical component of pressure acting on the treadband was reacted by the summation of static load on the wheel, additional force due to sidewall deflection beyond the static position, and damping force from the side wall proportional to the relative velocity between the wheel center and treadband.

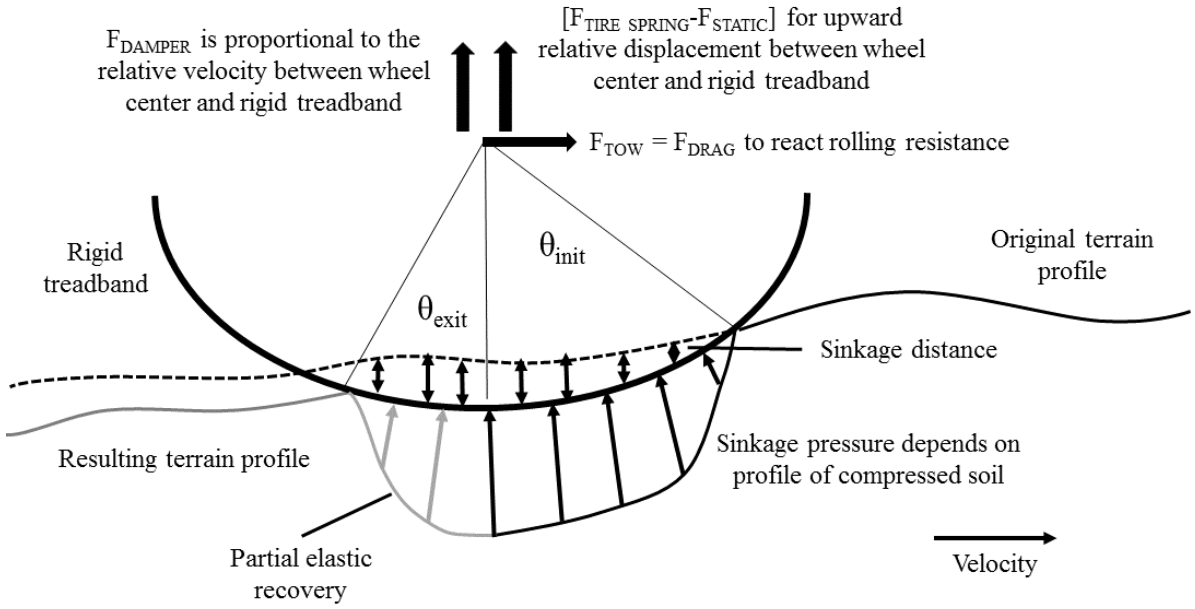

Figure 3.4: A schematic of forces acting on the treadband model. The sinkage-pressure profile depends on the terrain profile being compressed. Shear stress along the treadband was neglected. Elastic recovery of the soil was based on repetitive loading characteristics.

Sinkage pressure is governed by Eqn. (2.9) from the leading contact point at the front of the treadband to a transition point beneath the treadband. Beyond this transition point, the soil is assumed to be in elastic recovery modelled by repetitive loading (Wong, 1989), as described in Section 2.2.2. During model development it was found that neglecting elastic recovery (i.e. the assumption that soil contact ends at the bottom dead center point of the treadband) resulted in unrealistically deep sinkage values because only the front half of the treadband would support load. Additionally, a fixed transition point led to numerical issues

if a small sinkage at a given timestep resulted in initial contact starting behind the bottom dead center point. Therefore, the transition point from Bekker pressure-sinkage compression to elastic recovery was estimated by the following procedure, based on Fig. 3.5:

1. A secant between the leading contact point and the last point of contact is calculated from the converged solution of the previous time step.

2. A radial line normal to this secant is determined.

3. The treadband gridpoint nearest to this radial line is selected as the transition point.

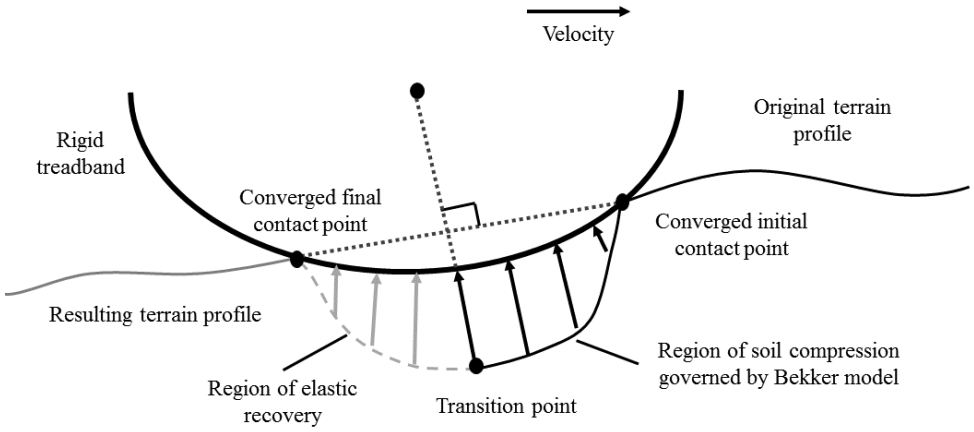

Figure 3.5: A schematic indicating where soil compression transitions to elastic recovery. Based on the solution of the previous time step, a secant is formed between the initial and final contact points. The intersection of the normal to this secant and the treadband is used as the transition point.

Because the end of contact is solely determined by the sinkage pressure at the transition point and the soil recovery properties, sinkage "history" behind the transition point is neglected. Generally, small sinkages result in no-till or minimum-tillage field conditions, and all wheels operate in a free-rolling towed condition, so shear stresses on the treadband were neglected. In summary, the vertical and drag force components acting on the treadband are calculated by the integration of the pressure acting on the treadband, given by

$$F_z = bR \int_{\theta_{exit}}^{\theta_{init}} p(\theta) \cos\theta d\theta \tag{3.1}$$

in the vertical direction, and

$$F_x = bR \int_{\theta_{exit}}^{\theta_{init}} -p(\theta) \sin\theta d\theta \tag{3.2}$$

in the horizontal direction, where R is the radius of the rigid treadband, b is the width of the treadband, $p(\theta)$ is the sinkage pressure as a function of angle, θ_{init} is the angle at the initial point of contact, and θ_{exit} is the angle at the last point of contact.

The soil-tire model implementation is capable of computing sinkage over uneven terrain, assuming vertical sinkage. Terrain profiles were generated randomly with specified spectral characteristics outlined by Wong (1978). Terrain frequency components related to the lateral tool spacing of a previous tillage operation can be observed in power spectra of tilled terrain (Bekker, 1969; Laib, 1977), so the desired power spectrum including the presence of furrows was used to form the filter coefficients of a finite-impulse-response (FIR) filter. This filter was then applied to a vector of random numbers drawn from a uniform distribution, whose length corresponded to the simulation length. This procedure was repeated to create unique terrain profiles for the walking axle, tail wheel and row units.

3.4.3 Terrain modification by opener

The seeding process using hoe-style openers involves an inherent modification of the terrain through which the opener passes. Video analysis indicated that the terrain over which the packer wheel passed was related to the depth of the opener when the opener was previously at this location. However, the depth of the opener is influenced by the position of the packer wheel, so this would suggest that feedback between the opener and packer wheel can occur, depending on the conditions of the field.

Generally, the tillage operation related to seeding tends to smooth the terrain to a certain extent. Small-scale terrain undulations were smoothed, but the equipment follows the longer-wavelength contours of the terrain (i.e. local roughness is reduced while field topography is followed). To incorporate the aforementioned feedback in combination with the general smoothing of the seeding process, the terrain inputs to the packer wheels could not be pre-generated in advance of the simulation. Rather, the elevation of each packer wheel terrain point was calculated as part of the simulation process. However, the literature is generally

lacking a robust, low-complexity approach for predicting the resulting terrain profile after the passage of a tillage tool. DEM holds the greatest promise for predicting this response, but with the accompanying computational expense. As a means to completing the development of this initial model, an approximate method based on the observed opener-packer wheel feedback phenomenon is presented here.

The opener tip and packer wheel are separated by a longitudinal distance (in the direction of forward motion) of $L_{sep} = 0.66$ m. Therefore, when traveling at velocity v, the packer wheel will pass over the current location of the opener tip $t_{delay} = \frac{L_{sep}}{v}$ *in the future*, at time $t_i + t_{delay}$. The terrain point that will be immediately beneath the packer wheel center at time $t_i + t_{delay}$ is computed at the current time step, t_i. In Fig. 3.6, the packer wheel will pass over the terrain at the $\star$ after this time delay, however the hoe opener will have modified the terrain profile during the seeding operation.

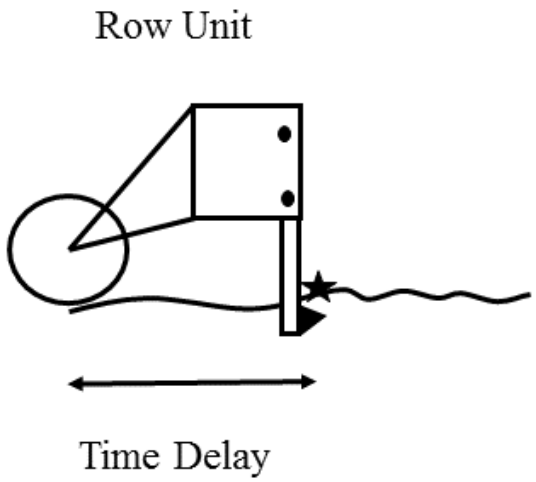

Figure 3.6: A time delay between the hoe opener and packer wheel occurs due to the separation between them. The point at the $\star$ will be passed over by the packer wheel after a time delay of t_{delay} seconds, thus the modification of the terrain by the opener is occurring in the future relative to the current position of the packer wheel.

While tillage is analogous to an averaging process, the resulting tilled soil profile is influenced more by the original terrain through which the opener just passed than by the terrain further behind the opener. Therefore, when computing the terrain elevation point to be experienced by the packer wheel at time $t_i + t_{delay}$, original terrain elevations experienced by the opener more recently are weighted more heavily than terrain experienced by the opener

further in the past. Weightings were chosen to increase linearly as distance behind the opener decreased.

This non-uniform weighting was motivated by the observation that the elevation of a point in the tilled terrain profile is more closely related to the elevation of points in close proximity than to the elevation of points further away. For example, a bump may be partially smoothed during seeding, but the material of the bump is not equally spread across the terrain following the bump.

An averaging distance of 0.2 m discretized into N_{span} points was selected as the distance over which the weighted average was taken. Feedback from the current position of the row unit was included by summing a portion of the row unit's displacement from its equilibrium position on deformable soil. Specifically, the new terrain elevation to be experience by the packer wheel in the future was computed by

$$Z_{PW}(t_i + t_{delay}) = \frac{\sum_{m_1=1}^{N_{span}} \left[m_1 \times Z_{OP}(t_{i-N_{span}+m_1}) \right]}{\sum_{m_2=1}^{N_{span}} m_2} + \frac{\delta_{OpenerEquilibrium}(t_i)}{C_{feedback}}, \tag{3.3}$$

where Z_{PW} is the packer wheel terrain input elevation experienced by the packer wheel in the future, $Z_{OP}(t)$ is the terrain height experience by the opener at time t, $\delta_{OpenerEquilibrium}(t)$ is the change from the opener's initial equilibrium position at time t, and $C_{feedback}$ is a factor controlling the amount of positional feedback.

Practically, Eq. (3.3) generates future terrain elevation points for input to the packer wheel from a N_{span}-point linearly weighted average of terrain immediately behind the opener, where terrain nearest the opener is more heavily weighted, summed with a fraction of the current displacement of the opener from its static equilibrium position on deformable soil.

Due to several openers ahead of the tail wheel modifying the terrain, a linear weighted smoothing procedure was also applied to the tail wheel terrain profile. This was applied prior to the beginning of the simulation as positional feedback was not included when modifying this profile. An averaging distance of 0.3 m was used.

3.4.4 Soil-tool interaction

The soil-tool interaction forces applied to the hoe opener were calculated based on the soil cutting model of McKyes and Ali (1977), presented in Section 2.2.1. The model was modified to consider soil-metal adhesion between the sides of the opener and the soil. The adhesion force acted opposite the direction of the opener's vertical velocity. This modification was included to reflect the simplification that the McKyes-Ali model does not consider vertical motion of the opener; i.e., it was developed to compute the draft and vertical forces on a tool working at a constant depth. This adhesion force was included to represent the resistance the opener would experience due to soil drag forces acting on the sides of the tool when changing depth. This form of damping improved the numerical stability of the simulation tool, but warrants future research.

The model allowed the direct calculation of draft and lift forces on the opener while only requiring prior knowledge of basic soil parameters: soil cohesion c, internal friction angle ϕ, soil-metal friction angle δ, and soil-metal adhesion c_a. An exponential activation function was used to improve numerical stability when the opener had a very small vertical speed (< 0.005 m/s); below this speed the adhesion force was reduced.

The soil-tool force calculations were performed outside the main program script so the specifics of the model can be quickly modified. The rake angle used to calculate these forces was assumed to be constant, as video observations indicated the orientation of the row unit relative to the soil surface varied little. Accordingly, the draft and vertical forces were assumed to act, respectively, horizontally and vertically at the opener tip.

3.5 Solution process

The governing dynamic equations were developed using Newtonian mechanics and were solved using matrix inversion in the time domain due to the non-linear nature of the random terrain inputs and soil contact problems.

At the beginning of the simulation, the static forces applied to the tires were determined, neglecting soil drag forces at the tires and opener draft/lift forces. The static forces on the

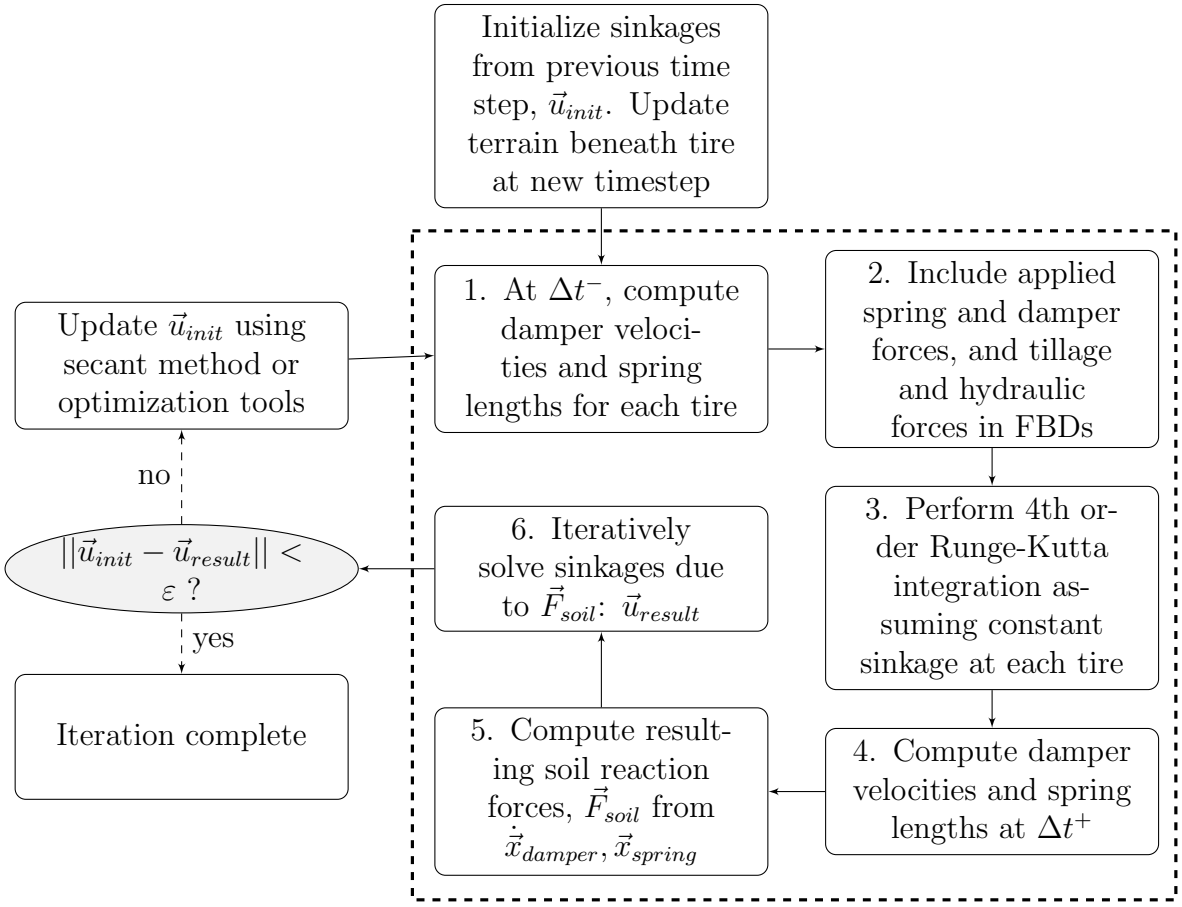

Figure 3.7: The procedure for iterating during each time step, for each tire in the plot drill model. The subroutine within the dashed box was programmed in a form where the inputs are the current machine states, the value of $\vec{u}_{init}$, and the new terrain beneath each wheel. The subroutine output is the root-mean-square-error (RMSE) $||\vec{u}_{init} - \vec{u}_{result}||$. This format enabled the use of optimization solvers within MATLAB®.

tires were used to calculate the static sinkage of each wheel. The static geometry was updated to reflect this static sinkage, and the process was repeated until the static configuration converged. This configuration represents the drill on flat deformable soil before encountering varying terrain. After the static configuration was found, the calculation procedure used at a given time step is shown in Fig. 3.7. In Fig. 3.7, Δt^- refers to quantities at the beginning of the time step, and Δt^+ refers to quantities computed after Runge-Kutta integration, but before the time step was advanced. A fixed time step length of $\Delta t = 0.0025$ *sec* was used for all simulations.

Solving for the states of the model during a given time step was an iterative process. State-

dependent forces, like the spring and damping forces of the tire sidewalls, depend on both the wheel center and treadband positions and velocities. However, the treadband position is defined by its current sinkage which depends on the force applied to the treadband from the sidewall spring and damper. Therefore, an iterative process was required to solve for the sinkage and wheel center position of each tire in the model.

As outlined in Section 2.2.2, the cumulative vertical force acting on the treadband is a function of the sinkage. As such, due to the random terrain involved in the calculation, a closed form expression for sinkage as a function of vertical load cannot be derived. Therefore, calculating the sinkage resulting from the forces computed in Step 6 of Fig. 3.7 was also an iterative process for each tire. Thus, solving for the sinkage of all tires along with the other states of the model required iterative calculations within an iterative cycle during each time step.

3.5.1 Main time-step iteration

Direct substitution of the calculated sinkage values $\vec{u}_{result}$ as the guess for the next iteration, $\vec{u}_{init}$, generally led to numerical divergence within a given timestep. Mathematically, the divergence occurred because the overall mapping from one iterate to the next was non-contractive when vertical compliance in the system was provided only by relatively stiff tire sidewalls and soil stiffness characteristics. Numerical methods research is an active field, and strategies for solving diverging systems are available, however many techniques require continuous mapping derivatives. The terrain characteristics contribute to the overall mapping by means of the numerical algorithm in Fig. 3.7, so techniques based on analytical derivatives were excluded.

The secant method was chosen for its simplicity in not requiring the determination of analytical derivatives (Mathews and Fink, 2004). This simplicity comes at the expense of needing two sets initial guesses, as the slope of the solution is approximated by two consecutive iterates. Iterates diverged slowly enough to allow the calculation of a 2^{nd} initial guess by direct substitution of the first iterate. After two iterations, the solution technique was changed to a secant-based method for each wheel.

An example of single-variable secant iteration follows, based on Fig. 3.8. For a given

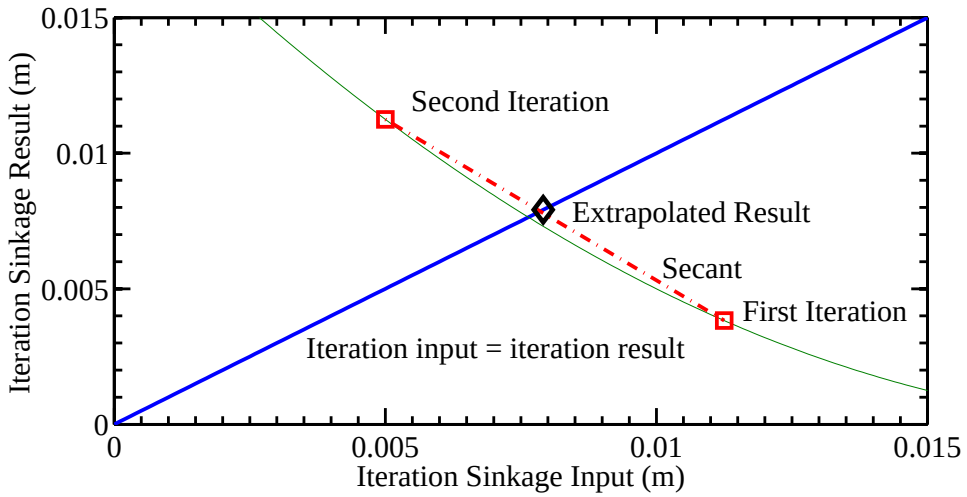

Figure 3.8: Secant iteration begins with two initial guesses (squares). From these 2 points, a secant line(dashed) is calculated and the crossing point with a $\vec{u}_{init} = \vec{u}_{result}$ solution line is calculated. The value of the $\diamond$ becomes the input for the next (third) iteration. A secant between the 2nd and 3rd iteration is computed, and the process is repeated until convergence is achieved.

wheel, two initial sinkage guesses are required, each with a corresponding sinkage "result" based on the iteration process shown in Fig. 3.7. A secant between these two pairs of points is calculated and its crossing point with the line $\vec{u}_{init} = \vec{u}_{result}$ is computed. This crossing point is used as the input for the next iterate. Following this iteration, the secant is updated to be between the most recent iteration and the one prior. Because the problem was generally non-linear, this process was repeated until the error tolerance $\varepsilon \leq 1e^{-7}\ m$ was achieved.

This scheme was a scalar approach to solving a vector-function problem because the sinkage of each wheel was solved for sequentially during each update of $\vec{u}_{init}$, rather than simultaneously as a vector-function problem would require. A more rigorous treatment would require the numerical approximation of partial derivatives with respect to the sinkage of each tire in every iteration. However, this simplification was permissible because step sizes are small, as this is a prerequisite to using a constant sinkage value during each time step.

Qualitative analysis of the test video revealed that some test configurations result in the packer wheel losing contact with the soil. From a numerical perspective, this causes sharp discontinuities in iteration results when the wheel is close to losing or regaining soil

contact. Thus, alternatives to the secant method were required for robust simulation of current technology throughout the operating range of interest. By formulating a given time step calculation as a function where a scalar error measure (RMSE) between initial tire sinkage guesses, $\vec{u}_{init}$, and resulting tire sinkages, $\vec{u}_{result}$, was to be minimized, established optimization methods were applied to the iteration process when soil-tire contact was lost or regained. This portion of the iterative process is contained in Fig. 3.7 by the dashed-line box: the inputs to the function are $\vec{u}_{init}$, and the output is a scalar RMSE value.

In particular, an implementation of the Nelder-Mead simplex direct search (Lagarias et al., 1998) was readily available within the MATLAB® environment using the *fminsearch* function (The Mathworks, Inc., 2014). This method does not guarantee a globally optimal result, however, an appropriate choice of initial values reliably produced a solution in the region of interest. Pattern search optimization methods were utilised in instances where *fminsearch* failed to satisfy convergence criteria. Discontinuous optimization methods (pattern search) can be much slower than many derivative-based methods, and thus were only activated when the secant method failed to converge.

3.5.2 Soil-tire iteration

As previously indicated, calculating the force required for a known sinkage of a given tire can be performed directly, but Step 6 of Fig. 3.7 required calculating the sinkage resulting from a given applied force. A closed form solution for this inverse calculation was not possible because of the random terrain that was under considered. Therefore, an iterative process was required to calculate the resulting sinkage of each tire at the end of the solution process based on the resulting vertical force applied to the soil. To clarify, within the iterative process of each time step, individual tire sinkage calculations also required iteration because tire sinkage could not be calculated explicitly for a given applied force. The single-variable secant iteration method was also used for this iterative process because analytical derivatives are not required, but again at the expense of needing two initial guesses. In instances where convergence could not be achieved using the secant method, single-variable Nelder-Mead simplex direct search methods were applied again.

Depending on the choice of the error residual limit (defined as the magnitude of the force

difference between consecutive iterations), convergence was not always numerically possible. This was due to discontinuities that result from the discretization of the rigid treadband. Only segments of the treadband that lie completely within the intersection of the original terrain surface and the rigid treadband in its current sinkage position were considered to be in contact with the terrain, and therefore, included in the calculation of soil reaction forces from Eqs. (3.1) and (3.2). Therefore, if sinkage estimates differed enough between iterations that the discretized leading point of contact moved along the treadband, the mapping from the previous iteration was discontinuous. This slight change in sinkage resulted in an additional treadband segment being included in the pressure integration calculation.

This was remedied by decreasing the treadband segment length; the gaps in the solution space became smaller than the residual limit used when iterating to find the sinkage corresponding to an applied soil force. However, the mesh size parameter had a significant effect on computational speed because the model required use of this soil-tire iteration process for each of the 6 tires during every main iteration cycle within one time step. Extremely fine tire discretization was not required during the vast majority of time steps. To avoid unnecessary computations due to fine discretization, segment size was only reduced when poor tire-sinkage convergence was apparent. If "hunting" between two leading contact points was still evident after discretization refinement, an average value of the previous iterations was used, and the simulation progressed.

3.6 Results and discussion

A direct comparison of model simulation results to measured plot drill response is presented, as the ability of the model to accurately represent the physical response of the plot drill was a key requirement.

3.6.1 Simulation results

To confirm model validity at speeds above typical operating speeds, simulation trials were compared to test results at 1.1, 2.2, and 3.3 m/s. The model was populated with geometry based on the dimensions of the plot drill, and system parameters (i.e., tire stiffness, soil

cohesion and internal friction angle) were collected from available engineering design data and published values in the literature (Kushwaha and Linke, 1996; Okello, 1991). A comparison of simulation results to field measurements for the row unit, main boom, and subframe follows.

In order to further understand model performance, spectral analysis techniques were used to analyze the acceleration response of the plot drill. Spectral analysis involves decomposing a signal into its constituent frequency content. As the characteristics of the response of the system result from both the characteristics of the inputs and the system itself, signal processing techniques can help in understanding if a response feature is due to the input, the system, or both.

As suggested by Lines and Peachey (1992), a point-to-point time domain comparison between simulated and measured dynamic data is ill-advised, even when the inputs to the measured response are known. This is due to the misalignment error in the time domain that can result from even small differences in the dominant frequencies of the two signals being compared. Furthermore, frequency domain representations further distinguish the relative contribution of a frequency range to the total response, providing much more information than total response metrics such as the RMS or total power of a signal. For example, if the difference in RMS acceleration between a simulated and measured response is significant, but the characteristics of spectral response are similar (i.e., a common frequency range of power concentration, similar relative amplitudes of power concentration), then perhaps differences in the input amplitude or in relative damping between the two systems are the cause. Similarly, a measure of total power may mask significant differences in the signal's frequency distribution stemming from poor model accuracy.

Row unit comparison

The PSD of measured and simulated row unit vertical acceleration at 1.1 m/s are presented in Fig. 3.9 (top). The overall amplitude differences between simulation and test were substantial; however, part of this difference was attributed to the difference between simulation input amplitude and actual test field terrain. The model only included friction and damping at the soil-tool interface, and within the tire side wall and soil-tire system. With little intentional damping included in the row unit design, and non-ideal friction and damping

sources absent from the simulation tool, increased terrain amplitude in simulations led to an unrealistic response of the row unit, and numerical instability in some cases.

Additionally, the simulation results at 1.1 m/s appeared to be significantly bandlimited above approximately 9.5 Hz, as compared to the gradually decreasing measured response. The model presented is much-simplified compared to the actual machine, therefore mechanical phenomena such as joint stiction, clearances between components, advanced tire characteristics, hydraulic cylinder friction, and other non-linearities were neglected. The inputs were also idealized by neglecting events such as stone impacts at the opener, localized soil hardening, and the random inclusion of crop residue into the track of the packer wheel. The measured data contains these non-linearities and impulse-like events (stone impacts, stiction events, intermittent contact due to component clearances), so it is conceivable that the resulting broad-spectrum noise that these events cause would not be captured by the idealized model, but are readily measured by the accelerometers rigidly fixed to the machine.

Though differences were to be expected, the two responses did share some similarities: both responses exhibit a small peak at 1.75 Hz, below which the amplitude drops off significantly (left dashed line), and the simulated data with the regular terrain containing furrows (red) also contained a large peak near the frequency of the major measured peak (3.5 Hz - right dashed line, versus 3.0 Hz in the simulated response).

Further analysis of the aforementioned frequency values revealed some interesting aspects of the row unit response. The packer wheel of the row unit was exposed to terrain modified by the opener which was also attached to the row unit, so a simple model for calculating the new terrain experienced by the packer wheel (outlined in Section 3.4.3) was included in this simulation tool. The distance between the opener tip and the packer wheel center was approximately 0.66 m which equated to a pass frequency of 1.67 Hz at 1.1 m/s. This closely aligned with the increased power at 1.75 Hz present in both the simulated and measured data. The simulated terrain was modified in a manner that correlated to the motion of the row unit, therefore, this response was expected. Good agreement between measured and simulated data at this frequency indicated this feedback phenomenon was likely the cause of this frequency peak in the measured data.

The largest peak at 3 Hz in the simulated response (3.5 Hz measured) at 1.1 m/s was

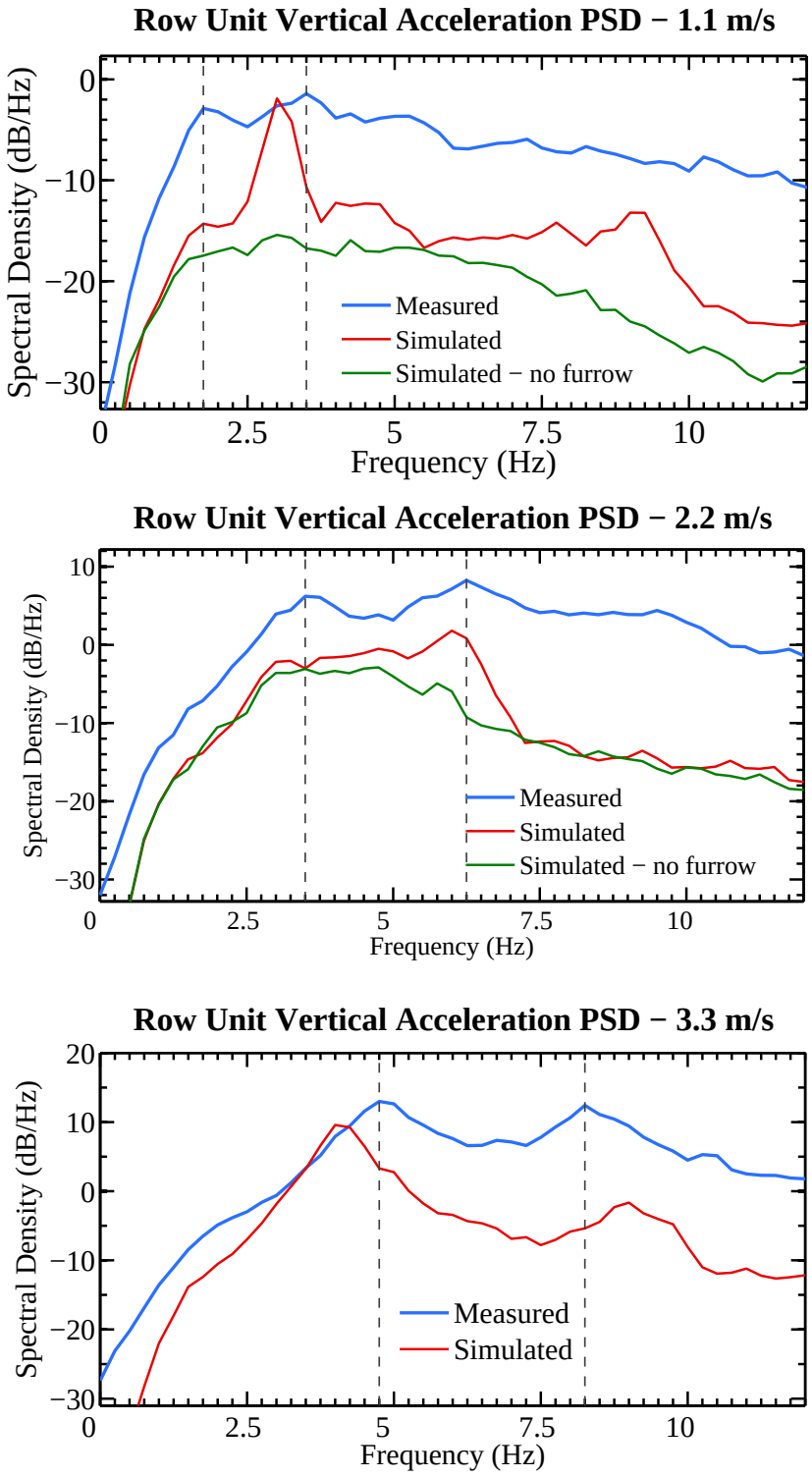

Figure 3.9: Power spectral density of row unit vertical acceleration, measured and simulated, at 1.1 m/s (top), 2.2 m/s (middle), and 3.3 m/s (bottom). The vertical dashed lines mark the peaks of interest in the measured data.

also related to important physical dimensions. When test data were collected, the test direction crossed the direction of seeding from the previous year at approximately 45° (not measured). The previous seeding operation used a hoe drill with lateral spacing of 0.254 m (10 in). Therefore, in the direction of testing the previous seeding furrows were spaced approximately 0.36 m apart. At 1.1 m/s, this resulted in a furrow pass frequency of 3.1 Hz, which closely corresponds to the largest peak in the simulation response. The slightly higher frequency of the measured peak (3.5 Hz) could be due to inconsistent tractor towing speed, or an actual relative heading angle of greater than 45°.

The simulated response at the furrow pass frequency was expected because the generated terrain had increased power content at this frequency. While the amplitudes and width of the peak at this frequency differed, it is an indication that the model performed in a similar manner to the actual test equipment, considering the elementary representation of the terrain. The simulated response behaved accordingly when the furrow component of the terrain was removed, as shown by the "no furrow" simulation results in Fig. 3.9 (top). That the model reflects the opener-to-packer wheel pass frequency was also a positive indication that the basic terrain generation method was capable of replicating a response similar to that of the actual test equipment.

The response of the row unit at 2.2 m/s followed a trend similar to that of the 1.1 m/s data. A comparison with measured data is presented in Fig. 3.9 (middle). At this velocity, the main response peaks of simulation and test results aligned well in frequency, and the amplitude difference was smaller in comparison to 1.1 m/s. Similar to the comparison at 1.1 m/s, the simulation response amplitude above 7.5 Hz was substantially less, indicating either a damped model response or reduced simulation inputs above this frequency.

In Fig. 3.9 (middle), the smaller measured peak at approximately 3.5 Hz correlated with the opener-to-packer wheel distance (left dashed line), although the simulated row unit vertical natural frequency may have also contributed to the modelled response above 3.5 Hz. The simulated feedback peak occurred at approximately 3.25 Hz. The higher-frequency peak (right dashed line) was partially due to the furrow pass frequency content in the terrain input. The simulation result without furrow content in the input terrain still contained a response peak at approximately 5.5 Hz, but at an amplitude approximately 6.75 dB lower

than the simulation with furrowed terrain.

Compared to the simulation results at 1.1 m/s, the furrow pass frequency peak at 2.2 m/s was less distinct. The model describing the terrain modification by the hoe opener included a contribution based the row unit's distance from its equilibrium position. The overall motion of the row unit at 1.1 m/s closely followed the terrain which contained a strong 3 Hz contribution at 1.1 m/s, so the dominant response at 3 Hz was expected. As the row unit began to bounce more at 2.2 m/s, the contribution from the terrain modification model would have increased with a corresponding increase in row unit acceleration below the furrow pass frequency. Because the terrain modification model employed a moving average filter, it attenuated more of the high frequency content present in the terrain profile under consideration.

Simulation results at 3.3 m/s were compared to measurement data in Fig. 3.9 (bottom) to verify model validity at greater-than-typical operating speeds. The overall shape of the two responses was quite similar, and the trend of generally under-predicting the response continued from the lower simulation speeds. The simulated peak at the opener-to-packer wheel pass frequency (4.0 Hz) was clearly present, but occurred at a frequency lower than the peak in the measured response (4.75 Hz). The frequency misalignment again may have been due to the presence of the vertical natural frequency of the row unit in the simulated results due to the parameters used in the model, and general lack of damping apparent in the simulation. Since the measured data at all three speeds only exhibit speed-related frequency peaks, the likelihood of this strong natural frequency-related response being present in the measured data is low. Interpretation of this lower frequency peak is further obscured by the fact that bumps created by the vertical motion of the row unit did not form at the tip of the actual opener (as assumed by the simulation tool). Rather, bump formation occurred over a period of time behind the opener tip, effectively shortening the distance between the bump and packer wheel.

The furrow pass frequency at 9.0 Hz was evident in the row unit response, although misalignment with the measured furrow pass frequency (8.25 Hz) was present when compared to the vertical dashed line of the measurement data. The amplitude at lower frequencies compared well; however, the amplitude of the furrow pass frequency peaks differed by ap-

proximately 13.8 dB. Based on the differences in amplitude of this pass frequency feature between simulated and measured data at both 2.2 and 3.3 m/s, greater furrow amplitude in the input terrain may have improved agreement between the simulated and measured row unit response. Similar to the other simulation speeds, the simulated response dropped off quickly beyond the furrow pass frequency.

Main boom comparison

The response of the main boom was measured by the IMU mounted on the main structural member between the castering walking axles.

Simulated and measured boom acceleration PSDs at 1.1, 2.2, and 3.3 m/s are presented in Fig. 3.10. The measured data were dominated by a large broad peak at a fixed frequency with a second peak at a frequency that increased with speed. Most of the response was below approximately 11 Hz. At 1.1 m/s (top), measured peaks at 2.75 and 4.5 Hz were present; at 2.2 m/s (middle), distinct peaks occurred at 3.75 and 5.5 Hz. Measured data at 3.3 m/s (bottom) also had a 3.75 Hz peak, with another peak at 8.25 Hz. Similar to the simulated row unit response, the boom acceleration response tended to fall off quickly above the first main peak.

Simulation results at all speeds had a large peak at 3-3.5 Hz. This peak did not shift with speed, therefore, it was hypothesized that this was the natural frequency of the vertical DOF of the boom. If the plot drill boom model was further reduced to a simple spring-mass system, where the mass was equivalent to the static load on one walk axle wheel, and an effective spring stiffness was derived by placing the tire spring in series with an equivalent soil spring, the natural frequency of this simple system was 3.2 Hz. This estimation agreed closely with the largest peaks in the simulated data at 2.2 m/s and 3.3 m/s in Fig. 3.10. If the simple spring-mass system was modified such that the spring stiffness was taken to be only the stiffness of the tires (without considering soil stiffness), the natural frequency of this simple system 3.9 Hz which closely agrees with what was thought to be the measured bounce natural frequency of the boom.

The boom natural frequency (simulated) was close to the furrow pass frequency at 1.1 m/s (3.1 Hz), so the large simulated amplitude response at this frequency was somewhat

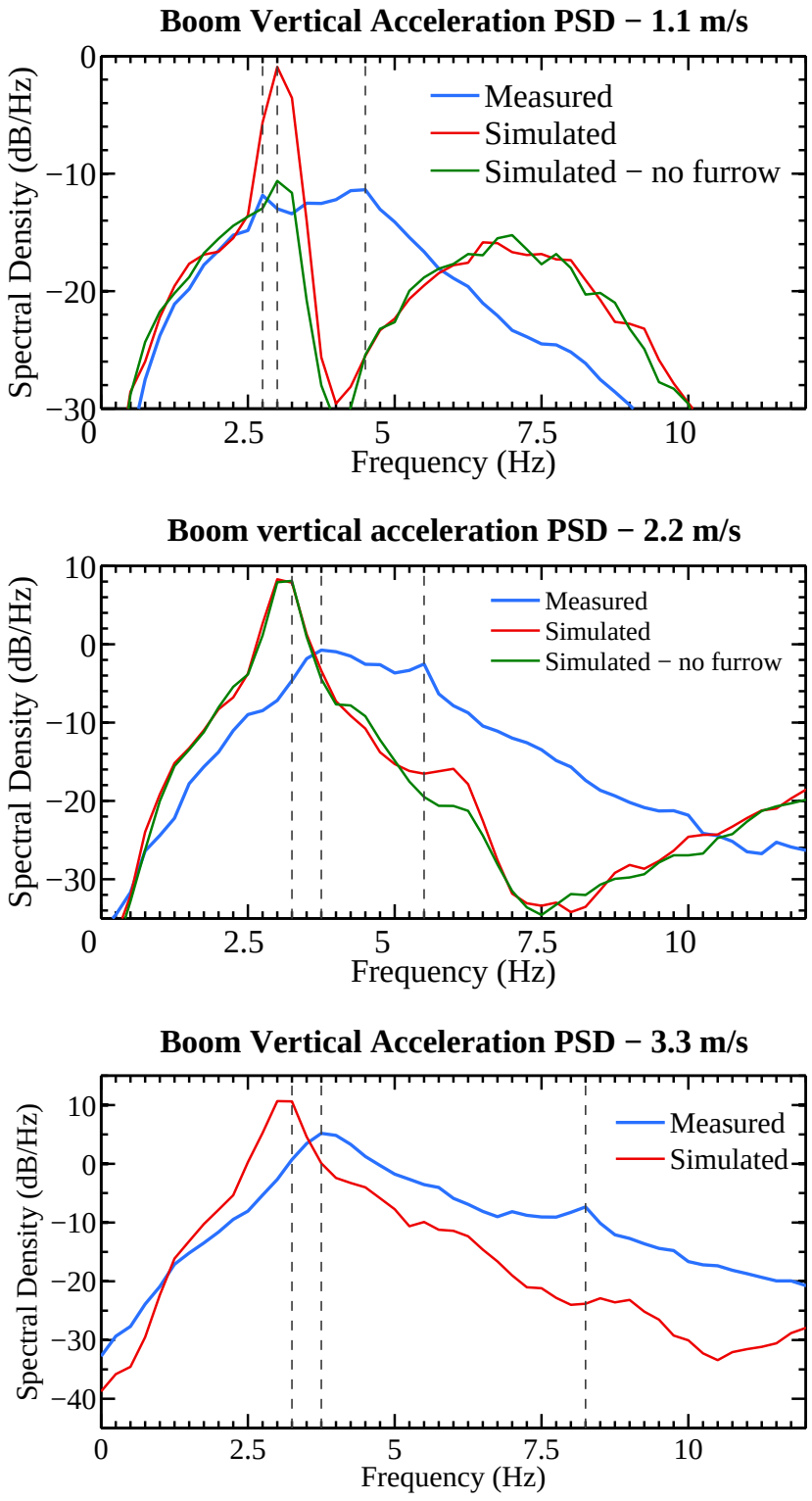

Figure 3.10: Power spectral density of boom vertical acceleration, measured and simulated, at 1.1 m/s (top), 2.2 m/s (middle), and 3.3 m/s (bottom). The left pair of dashed lines pass through the measured and simulated boom natural frequency. The right dashed line marks the measured peak due to the existing furrows in the field.

expected. The body was excited near its resonant frequency and very little damping was provided by the walking axle tires. The measured data did not exhibit as large of response due to possible disagreement between the simulated and actual boom natural frequency.

When the furrow-related spectral content was removed from the generated terrain profiles at 1.1 m/s, the simulated response amplitude at 3 Hz was reduced by 9.4 dB, and was much closer in magnitude to the measured results (Fig. 3.10 top). Above this frequency, the simulated response dropped off quickly, but was followed by another broad increase in response centered at 7 Hz. Due to this attenuation valley at 4.25 Hz, the 2^{nd} measured peak at 4.5 Hz was completely missing in the simulation data.

A comparison between the measured data at all three speeds in Fig. 3.10 indicated that the vertical natural frequency of the boom was closer to 3.75 Hz, versus the predicted peak at 3.25 Hz. This discrepancy was potentially due to stiffer soil characteristics than those used in the simulations, walking axle tires with an effective stiffness greater than the static tire stiffness parameters provided, or load transfer to the tractor hitch through the frame hydraulic cylinder resulting in a response not captured by the reduced-DOF model. The lack of a distinct resonance at 3.75 Hz in the measured 1.1 m/s data was possibly due to poor signal-to-noise ratio considering the low test speed. If the simulated resonant frequency was closer to the measured natural frequency (3.75 Hz), the severity of the over-predicted response in this region at 1.1 m/s (Fig. 3.10 (top)) could be reduced, and overall agreement between simulation and test would improve at this speed.

At 2.2 m/s, the simulated response in Fig. 3.10 (middle) had an additional peak at approximately 6 Hz that closely aligned with a peak in the measurement data. This was due to the furrow content in the input terrain. The peak effectively disappeared from the simulation results when the furrow content was removed from the input terrain. While some frequency misalignment was present, the modelled response of the boom responded to the presence of previous furrows in the terrain much like the actual boom of the plot drill.

An attenuation valley at approximately 7.5 Hz was present in the simulated data at 2.2 m/s, similar to the valley present at 4.25 Hz at 1.1 m/s. The frequency of maximum attenuation does not appear to be directly related to simulation speed, however the broad peak to the right of each valley (7 Hz at 1.1 m/s; approximately 14.5 Hz at 2.2 m/s - not

visible) do appear to be speed related. The mechanism causing this attenuation with a broad high frequency response was not identified during model development.

The furrow frequency was also present in the 3.3 m/s measurement data in Fig. 3.10 (bottom) at 8.25 Hz. Similar to the row unit results in Sec. 3.6.1, and the boom comparisons at lower speeds, the predicted furrow frequency was greater than the measured furrow frequency with a less distinct peak.

The differences between simulated and measured acceleration were due to difference in both input characteristics and model simplifications. In general, the natural frequency of the boom appeared to be less damped compared the measured response of the boom. Increased furrow amplitude may improve the agreement between simulation and measured data at higher frequencies. In general, the initial frequency agreement between simulated and measured performance of the boom was promising. With inputs that more accurately represent those of the test field, and better estimates of the tire damping parameters, the overall accuracy of the simulation results could likely be improved.

Subframe comparison

A vertically-oriented accelerometer was mounted on the subframe near the tail wheel to measure the motion of the subframe. The PSD of the measured and simulated responses at 1.1, 2.2, and 3.3 m/s are presented in Fig 3.11.

The general trends at all three speeds agree, however the simulation result at 1.1 m/s (Fig. 3.11 (top)) had a large peak at 3 Hz (left vertical dashed line) which was not present in the measured data, and a smaller peak at 4.5 Hz (right vertical dashed line). It was confirmed that the 3 Hz peak was partially due to the furrow inputs by running a simulation without distinct spectral content at the furrow pass frequency. The difference in simulation amplitudes near 3 Hz was approximately 10 dB (simulation with and without furrow inputs). However, even with the furrow profile removed, a smaller peak was still present at 3 Hz which was likely caused by coupling between the boom and subframe. The subframe acceleration measurement point (in both test and simulation) was not located at the tail wheel but rather near the end of the subframe. Therefore motion of the boom would result in measurable acceleration at the measurement location.

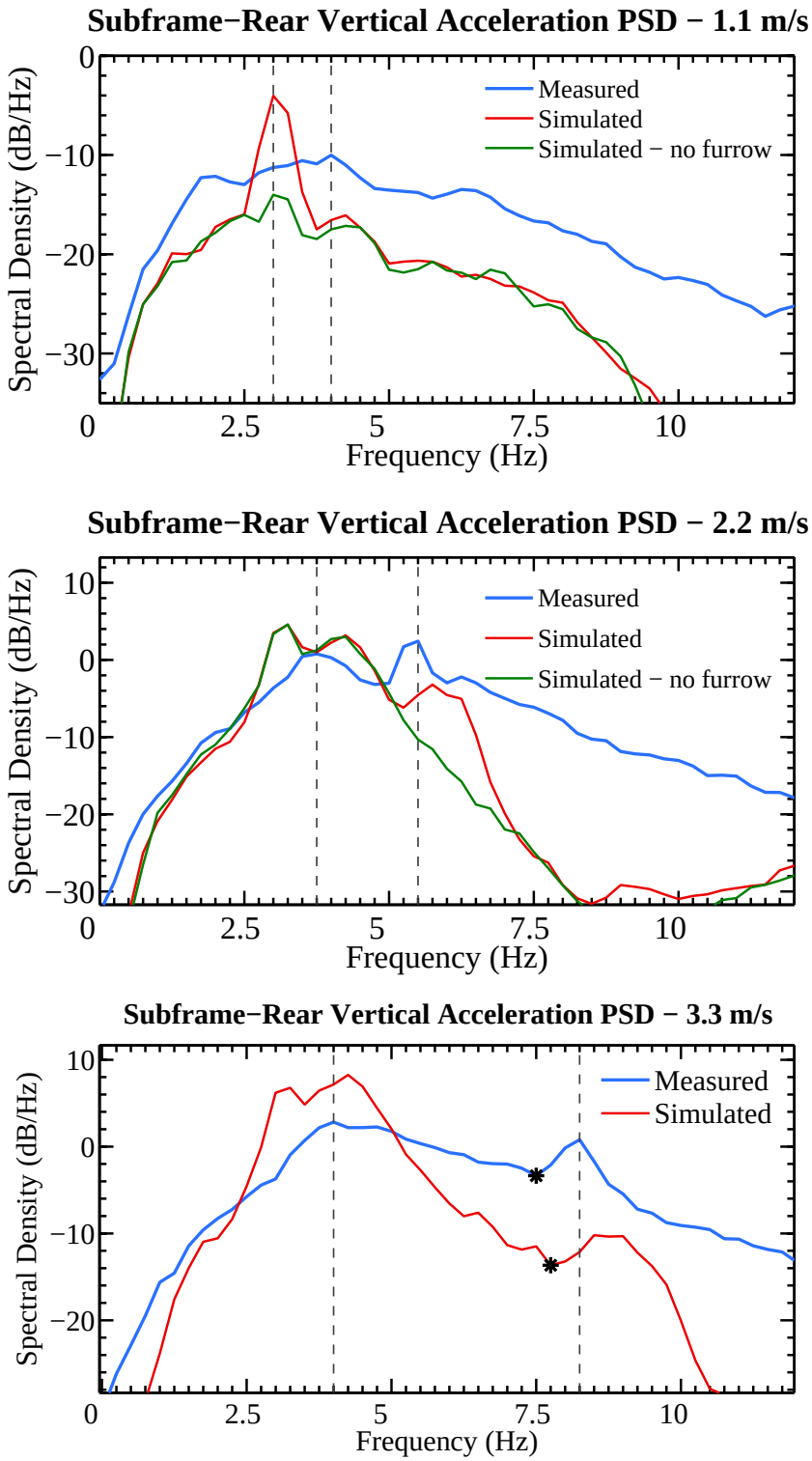

Figure 3.11: Power spectral density of subframe vertical acceleration, measured and simulated, at 1.1 m/s (top), 2.2 m/s (middle), and 3.3 m/s (bottom). The left vertical dashed line passes through the natural frequency of the subframe. The right dashed line passes through the measured peak excited by the existing furrows in the field.

At 2.2 m/s, the simulated response contained three distinct peaks at 5.75 Hz, 4.25 Hz, and 3.25 Hz. After removing the furrow-related spectral content from the 2.2 m/s simulation input, the simulated peak in Fig. 3.11 (middle) at 5.75 Hz (5.5 Hz measured), was confirmed to be related to the furrow input. By removing the furrows in the simulation input, the magnitude of the response at 6 Hz was reduced by approximately 8.4 dB. The amplitude difference between simulated and measured furrow pass frequency peaks at this speed was approximately 5.3 dB.

By modifying the mass of components in the model near the tail wheel, the mechanism related to the simulated peak at 4.25 Hz at 2.2 m/s was investigated. Significantly increasing the mass of the vertical hitch support link (between the subframe and the air cart hitch) by 200 kg shifted the simulated peak from 4.25 Hz to 3.75 Hz (not presented). This indicated that this portion of the response was indeed related to the resonant frequency of the subframe bouncing on the tail wheel. However, increasing the hitch support mass did not shift the 3.25 Hz peak. This further points to the 3.25 Hz peak resulting from to motion of the boom, considering the strong response of the boom at this frequency (see Fig. 3.10 (middle)). Above the furrow pass frequency the amplitude difference between simulation and measurement results increased significantly as previously observed.

At 3.3 m/s (Fig. 3.11 (bottom)), the furrow pass frequency was evident in the simulation results at 8.5 Hz (measured: 8.25 Hz), however the simulated peak was 9.73 dB below the measured response. Given the trends in the analysis of the row unit and boom, this is likely due to under-excitation of the model in this frequency range. The rise in response above the furrow pass frequency base ($\star$) at 3.3 m/s was similar between simulation and test (3.4 dB vs. 4.1 dB respectively). Similar to the simulated 2.2 m/s results, peaks at 3.25 Hz and 4.25 Hz were also present at this speed. The large magnitude of these peaks potentially indicates that the tail wheel and walking axle wheels required higher damping values than those used for the simulation. The damping parameters used were estimated from literature (Lines and Murphy, 1991a), as this data was not available during model development.

The subframe vertical natural frequency difference (4.25 Hz simulated compared to 3.75-4.0 Hz measured) was attributed to the mass difference between the model and the actual machine. Only three row units were present in the model, so the simulated subframe tended

to bounce on the tail wheel at a higher frequency compared to the actual machine.

3.7 Conclusion

Increased seeding equipment productivity is demanded by equipment manufacturers and farm managers alike, and increasing implement operating speed is the next challenge in meeting these productivity needs. It is known that depth consistency tends to degrade with speed, in part due to excessive row unit motion. However, the capability to simulate the dynamic performance of seeding implements is lacking in the literature. A limited-DOF dynamic model of a towed seeding implement is presented and compared to operational data of the machine in seeding conditions in western Canada.

The simulation results indicated that row unit motion was driven by two phenomena. The simulated terrain contained a residual furrow pattern that was a normal result of the seeding operation from the previous season. This distinct periodic input was present in the simulated motion of the row unit. Additionally, the row unit was excited by the modified terrain profile that resulted from the hoe opener operating ahead of the packer wheel. Upward vertical motion of the row unit (and consequently, the opener) created uneven terrain that the packer wheel then passed over, which fed back into upward motion of the row unit. The underdamped row unit response of the model amplified this effect during the simulations. Both of these phenomena point to the poor attenuation of displacement inputs to the packer wheel when the opener and packer wheel are both rigidly coupled to the row unit body.

Generally, the amplitude of simulated response was lower than the measured data used for model verification. Part of this amplitude response difference can be attributed to differences in the terrain surfaces (simulation vs. test). Simulated terrain amplitudes were intentionally smaller to avoid unrealistic, and occasionally unstable simulation results stemming from the underdamped row unit model. The rigid body natural frequencies were also more pronounced in the simulation results when compared to the measurement data. Differences in damping between the model and actual machine are likely the cause of these rigid body amplitude differences. The difference in response amplitude increased at higher frequencies, however this was an expected result because of simplifications made during the modelling process.

This work has also highlighted the complex relationship between resulting seed furrow profiles and the terrain experienced by a packing wheel. Further work to understand and ultimately predict the terrain profile resulting from the tillage action of the opener is needed to improve the accuracy of predicted row unit motion.

Acknowledgment

Funding contributions from CNH Industrial and Natural Sciences and Engineering Research Council of Canada (NSERC) toward this work are gratefully acknowledged.

Chapter 4

Measuring the dynamic response of a towed seeding implement

Ian W. P. Paulson, Allan T. Dolovich, Scott D. Noble

This chapter contains the manuscript describing the collection, analysis, and interpretation of the dynamic response of the plot drill during various operation conditions. This work focused on meetings Objectives #2 and #3 in Sec. 1.2. This manuscript will be submitted to either the *Journal of Terramechanics* or *Transactions of the ASABE* titled "Measuring the dynamic response of a towed seeding implement", upon degree completion. A description of the plot drill will be condensed from Chapter 2 and inserted into Sec. 4.2.1 in the following manuscript.

Data collection activities including the installation of instrumentation, test equipment operation, writing of data processing programs, and data analysis and document writing was performed by the lead author. Prof. A. Dolovich and Prof. S. Noble both provided guidance regarding aspects of data interpretation along with valuable editorial contributions.

4.1 Introduction

The validation and comparison of model performance to measured data was outlined as an objective of this project in Section 1.2. This chapter focuses on the data collection details and methods used in this research. Note that the measured data presented for comparison in Chapter 3 were a result of the experimental work outlined in this chapter.

The complexity of the processes that occur during dynamic soil/machine interaction at both the soil-tire and soil-tool interface are acknowledged. An experimental dataset

was deemed valuable early in the project in light of these complex phenomena, as well as in consideration of the potential reduced model fidelity stemming from using simple, low-computational cost analytical sub-models to represent soil-machine contact. Modelling provides the ability to investigate specific sensitivities of the machine in more detail; experimental results are valuable in both evaluating model accuracy, and capturing machine response that simple multibody simulation models cannot replicate. When data analysis can be informed by modelling insights, the value of measured data can be leveraged further yet.

This chapter begins with details of the test implement, field, instrumentation, and data analysis in Section 4.2. Test results are presented and discussed, considering insights developed from the prior modelling work, in Section 4.3, and Section 4.4 concludes.

4.2 Methods and materials

To quantify changes in operational characteristics due to adjustable machine settings available to the operator, the geometric depth setting of the row unit and hydraulic system pressures were treated as independent variables. The selected values were in the typical operating range for a hoe opener seeding drill in operation in western Canada. As changes in dynamic response with increased seeding speed were the main interest of the project, seeding speed was also an independent variable with four speeds selected, including speeds above the typical maximum speed of approximately 2 m/s. Table 4.1 lists the values of the test parameters.

Table 4.1: Three operational variables were changed during data collection activities

Operational Variable	SI Units
Ground Speed	1.1, 2.2, 3.3, 4.4 m/s
Hydraulic Pressure	5500, 8270 kPa
Row unit geometric depth	25, 50 mm

4.2.1 Apparatus

The apparatus used for testing was a narrow version of a New Holland Agriculture P2070 Precision Hoe Drill modified for testing by CNH Industrial staff at the Saskatoon R&D office.

For presentation in the thesis, the description of the plot drill was expanded and moved to Chapter 2.

4.2.2 Instrumentation

As multiple geometric DOFs of the plot drill were present, a variety of instrumentation was used to record the motion of the machine. Mounted rigidly to the boom/hitch structure was an IMU capable of measuring translational acceleration and angular velocity relative to three orthogonal axes whose orientation moved with the plot drill (Crossbow Technology, Milpitas, CA). A summary of the sensors used, including the range and error specifications is given in Table 4.2. An accelerometer was mounted to the subframe near the tail wheel linkage connection point. It was oriented vertically when the subframe was aligned with the horizon. An accelerometer was also mounted to the front-center row unit oriented vertically when the machine rested on flat level ground. These separate accelerometers were manufactured by Memsic Inc. (Andover, MA).

The relative angles between the boom and subframe, between the subframe and the front-center row unit links, and between both walking axles and the frame were measured using an angular potentiometer. The angular potentiometer sensors (Power Components of Midwest, Mishiwaka, IN) required an additional linkage to be installed, therefore, the measured values required geometric post-processing to compute the actual relative angle of interest. A mounting schematic of the angle sensor between the boom and subframe is shown in Fig. 4.1.

The hydraulic cylinder provided an overload trip mechanism. If the hoe opener struck an immovable stone or other rigid object, the hydraulic cylinder enabled the hoe opener arm to pivot relative to the row unit if horizontal forces on the opener overcame the applied hydraulic force applied to the top of the hoe opener arm; see Fig. 2.3 for reference. During normal operating conditions, this situation does not occur, therefore the row unit was assumed to act as a rigid body. However, to monitor this possible condition, a string potentiometer (Measurement Specialties, Hampton, VA) was installed to measure the length of the row unit hydraulic cylinder. When the trip mechanism does not activate, the length of the cylinder can be calculated through the geometric relations of the row unit links; by monitoring cylinder

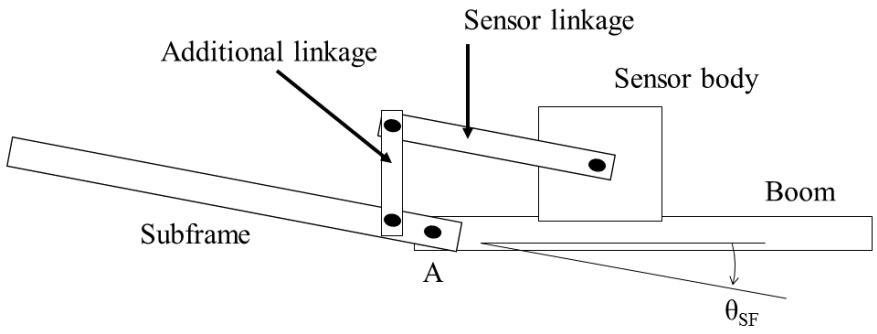

Figure 4.1: The mounting location between the boom and subframe is shown. Mounting the angle sensor required an additional linkage to be installed.

length independently, the trip condition could be identified.

Hydraulic pressure transducers (Panther Sensors - Hoskin Scientific, Burnaby, BC) were installed on the plot drill to measure the hydraulic pressures at the frame and row unit cylinders. An additional transducer measured the pressure in the return line from the row unit cylinder to the reservoir to ensure that pressure acting on this "raise" face of the cylinder piston was minimal.

The row unit of interest was modified to incorporate a load cell (Interface, Scottsdale, AZ) to measure a component of the resultant force at the packer wheel center. Due to geometry limitations, directly measuring both the vertical and horizontal force components at the wheel center was not possible. The load cell and mounting geometry are shown in Fig. 4.2. Referring to the figure, the body to which the packer wheel connects is normally rigidly bolted to the rest of the row unit by means of the depth adjustment bolt and a large bolted connection midway between the load cell and packer wheel. The load cell replaces the depth adjustment bolt; when the clamping pressure of the large bolted connection is released, the load cell measures the force required to counteract the moment created by packer wheel center forces acting normal to the moment arm between the wheel center and large bolted connection. Although the effect of this structural modification was not experimentally quantified, the published natural frequency of the load cell was 3350 Hz, so structural effects were assumed to be higher than the frequency range of interest.

Figure 4.2: The load cell used to measure a component of the resultant packer wheel force is visible on the row unit body.

4.2.3 Test field

The goal of the testing was to record the steady state operational response of the plot drill using the above instrumentation while seeding in a straight line. Operational data were used for validating the aforementioned plot drill dynamic model, as well as for further interpretation with the aid of the modelling tool. Data collection was conducted in a flat, level sandy-loam field near Saskatoon, Saskatchewan, Canada, after fall harvesting was completed in 2015. The previously seeded crop was canola. Due to the layout of the test area, measurement runs were divided by depth setting, and a fully randomized test order of speed and hydraulic pressure was created. Measurement runs at 25 mm depth were approximately 500 m in length, while the second block of 50 mm depth tests was approximately 300 m long.

All test runs crossed the previous seeding direction at approximately 45° (not measured), as shown in Fig. 4.3. The field was seeded using a hoe-opener style drill with lateral row spacings of approximately 0.254 m. Therefore, the terrain traversed by the plot drill during testing contained residual furrows from the previous seeding operation. Test runs alternated travel direction, and all overlap between neighboring measurement runs was avoided (including walking axle wheel paths).

Table 4.2: Description, manufacturer & model, and linearity specifications of sensors used for measurement

Description	Manufacturer (Model)	Range	Linearity (% FS)
IMU - 3 axis accelerometers	Crossbow Technology (IMU300CC)	± 2g	N/A
IMU - 3 axis gyrometers	Crossbow Technology (IMU300CC)	± 100°/sec	N/A
Accelerometer - 1 axis	Memsic Inc. (CXL25GP1)	± 25g	0.2% [1]
Angular position sensor	Power Components of Midwest (01142)	± 60°	3%
String potentiometer	Measurement Specialties (SP1-12)	0.3 m	0.025%
Hydraulic pressure	Panther Sensors (GPT101)	0-5000 psi	0.25% [1]
Load cell	Interface (SSM-1000)	1000 lbs	0.05%

[1] Total accuracy reported

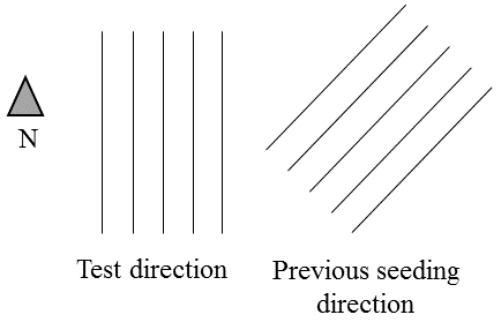

Figure 4.3: The testing direction crossed the previous seeding direction at approximately 45

Harvesting of the previous canola crop occurred in a direction approximately parallel to the testing direction, but residual plant matter was well spread across the test area. The canola crop yielded well, but without the decomposition processes that occur over winter the amount of plant residue present was significant, but not beyond what a seeding implement could experience during the spring seeding season.

4.2.4 Data processing

Meaningful metrics based on time domain data analysis were limited, given the apparent random nature of the measured kinematic response of the plot drill. Accordingly, spectral analysis in the frequency domain was preferred to identify major components of machine vibration. This approach assumes that the data can be considered stationary; i.e., statistical moments of the data do not have strong underlying trends. This is often the working

assumption of operational kinematic data. To support this working assumption, data were only used from periods of steady state operation. The plot drill directional heading was fixed, the operating speed of the tractor was set, the row units were lowered into the ground, the hydraulic circuits were engaged, then data recording commenced.

Overlapped segments (Welch, 1967) were used to compute the PSDs of kinematic parameters of interest. This approach reduced the variance of the PSD estimate at the expense of frequency resolution. 50% overlap and 0.25 Hz resolution were used in computing the presented PSDs. A PSD highlights the frequency range(s) which contribute the most power to the signal, thus it is useful in determining how underlying components of signals may differ. Reducing measurements down to a set single-value measures such as total power, mean values, etc., may be more appropriate for initial analyses.

Data were collected as time-varying voltage and current values with a National Instruments (Austin, TX) NI cDAQ-9174 data acquisition unit using a NI-9220 voltage module, a NI-9237 analog bridge voltage module, and a NI-9203 current module. Data were recorded by a ruggedized laptop stored in the instrumentation cabinet on the implement. Sensor calibrations were applied during post-processing, and the data were downsampled to 100 Hz in MATLAB® (The Mathworks, Inc., 2014) using a 30th-order FIR low pass filter to avoid aliasing during data decimation.

Accelerometer measurements include gravity contributions (Groves, 2015). As the plot drill moved during operation, its orientation (and that of the IMU) relative to an earth-fixed coordinate system was continuously changing during the measurement period. Therefore, a time-varying gravity contribution was present in the three IMU acceleration channels; correction for this variation was required. The IMU and angular position sensors enabled the orientation of all plot drill components to be calculated through time, relative to an earth-fixed coordinate system; the gravity contribution was then removed from the accelerometer measurements. Subsequently, the gravity-corrected accelerations of the plot drill were available in either an earth-fixed or machine-fixed coordinate system. Details of the mathematics in correcting the accelerometer readings can be found in Appendix B. Ultimately, the uncorrected and corrected data were very similar.

After the data were calibrated, low pass filtered, and corrected for gravitational contri-

butions when necessary, the steady-state portion of the test run was selected for further processing. Data prior to the row unit being lowered were discarded; only data beyond the start of a stable row unit link angle response was kept (several seconds after the row unit hydraulic pressure was applied). Data were trimmed prior to the row unit being lifted out of the ground at the end of the measurement run. This steady state segment of data was then used to calculate the various statistical quantities reported in Sec. 4.3. The PSDs presented are derived from data where the mean offset has been removed to reduce spectral leakage (Bendat and Piersol, 1986).

4.2.5 Comments on data variability

Considering the natural variation encountered in an agricultural field, noticeable variation both within a test run, and across different runs, was expected even with a constant machine configuration. While these measurement values will differ, comparing parameter values under the same machine configuration throughout the test area does give a sense of the underlying variation of the operating domain. Multiple"baseline configuration" runs (2.2 m/s, P_{Hyd} = 5500 kPa) were interspersed between treatments in each depth block test area. The expectation was not that a given parameter was to remain constant within a baseline run, or that metrics of different baseline runs were to be equal. Rather, when grouped together the baseline runs quantified the expected variability of a parameter due to test area variation.

Figure 4.4 displays PSD estimates of vertical row unit acceleration from three measurement runs at 2.2 m/s with P_{Hyd} = 5500 kPa and depth = 50 mm collected throughout the test area. The underlying trend is similar between all three runs with major power peaks occurring at similar frequencies with similar amplitudes. To quantify typical inter-run variability resulting from variable terrain and soil conditions, the minimum and maximum bounds were constructed from the three measurement runs in Fig. 4.4 between 2.5 Hz and 10 Hz – the frequency range that contains the majority of total power and several distinct peaks. In this frequency range of interest, the average difference between the maximum and minimum bound is 1.17 dB; or, the mean constructed from the three measured PSD curves in this range would, on average, be within 0.58 dB of the min/max bound of measured PSD estimates. Quantifying the average power range limits about a given power value (+/− 0.58

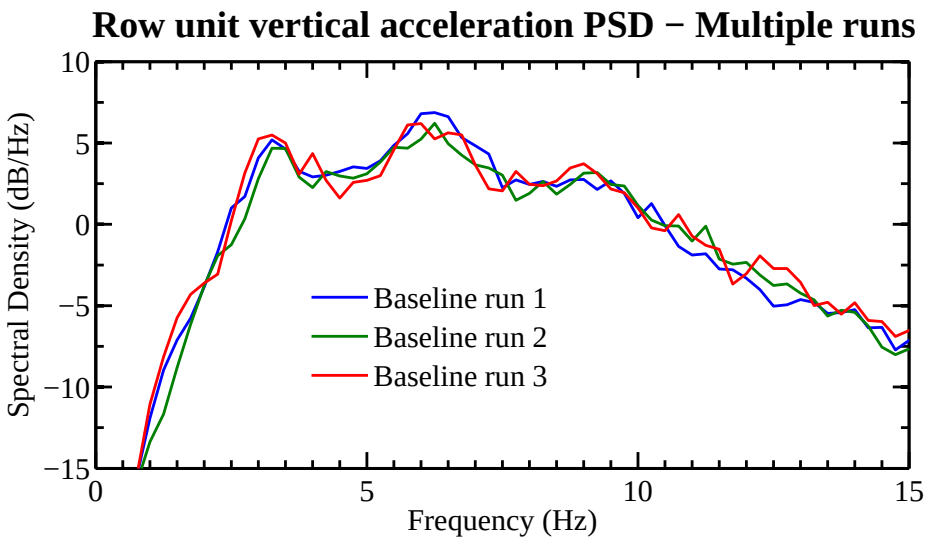

Figure 4.4: Multiple test runs at 2.2 m/s with P_{Hyd} = 5500 kPa and depth = 50 mm were recorded to measure the variation in machine response throughout the testing area.

dB) attributable to soil and terrain variability present between measurement runs was valuable in interpreting the changes in operational response due to machine configuration changes presented in later sections.

Although computing the average min/max range from multiple test runs was not a strict statistical test, it did give a sense of the within-group variation that should be expected from the measured data. Because of the exploratory motivation of the research project, this initial data collection program was not designed with the intention of determining strict quantitative differences between measurement runs or conditions. Therefore, statistical tests were not deemed appropriate in subsequent data analyses.

4.3 Results and Discussion

Measured row unit and frame vibration results are presented and discussed in the following section to understand how speed, depth and hydraulic settings affect row unit response and packer wheel loads. Excitation mechanisms related to increased hydraulic pressure are discussed, along with analysis of coupling between the frame and the instrumented row unit. Additionally, test video demonstrating plant residue motion relative to the row unit are

discussed and contrasted to the performance of the model presented in Chapter 3.

4.3.1 Row unit vibration

The variance of the row unit acceleration in the vertical direction is presented in Fig. 4.5. The average acceleration was near 0, therefore a metric reflecting changes in acceleration was preferred to describe the motion of the row unit, hence variance was used.

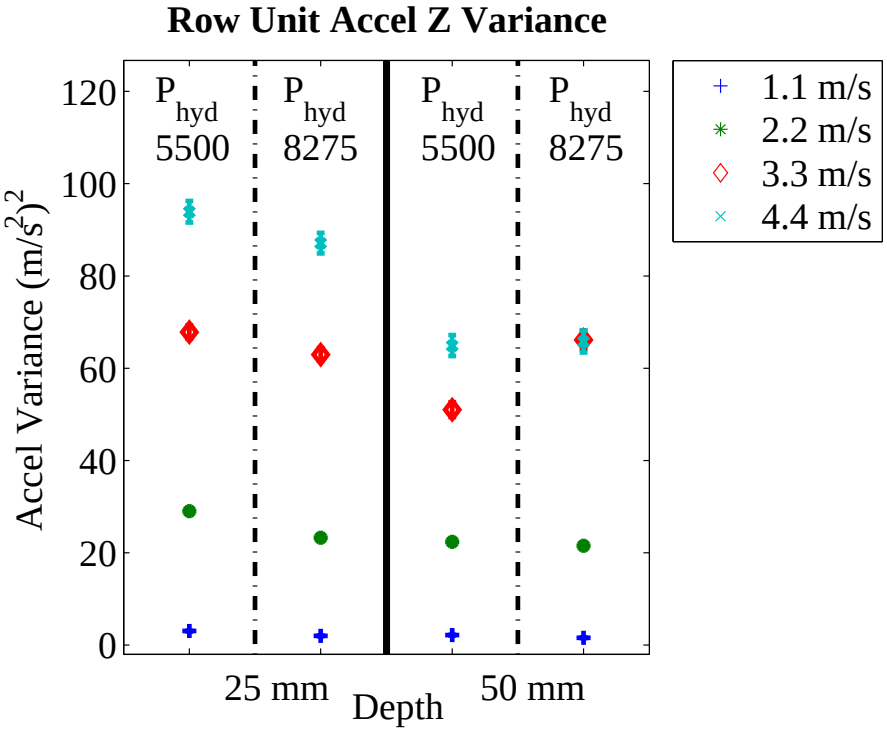

Figure 4.5: Variance of the measured row unit vertical acceleration in a coordinate system fixed to the subframe, grouped by speed, geometric depth setting (L/R), and hydraulic system pressure (column), with error bars indicating the 95% confidence interval of the variance estimate.

As expected, increases in acceleration variance are most strongly correlated with ground speed. The increase in ground speed from 2.2 m/s to 3.3 m/s generally resulted in the largest increase in acceleration variance across all machine configurations. In general, increased hydraulic pressure was more effective in reducing the acceleration variance at the shallower depth setting compared to the deeper depth setting. At 25 mm depth, increased hydraulic pressure provided a similar *magnitude* decrease in acceleration variance at all speeds above 1.1 m/s. Except for the difference between hydraulic pressures at 3.3 m/s and 50 mm depth,

increasing hydraulic pressure at the 50 mm depth setting had little effect on acceleration variance.

At the two highest speeds, increasing the depth while maintaining $P_{Hyd} = 5500$ kPa resulted in a larger variance reduction than an increase in hydraulic pressure while maintaining a depth of 25 mm. At 3.3 m/s, increasing only the pressure reduced acceleration variance by 7% at 25 mm depth, whereas a depth increase reduced acceleration variance by 25%. At 4.4 m/s, these changes resulted in reductions in acceleration variance of 7% and 31% , respectively. In contrast, reductions in acceleration variance were similar between system parameter changes at lower speeds. At 2.2 m/s, increasing the hydraulic pressure reduced acceleration variance by 20% at a depth of 25 mm, and increasing depth reduced acceleration variance by 22%.

To explore further differences in the measured results, PSD estimates were generated from steady state operating data using Welch's overlapped segment method. PSDs from each test speed are shown in Fig. 4.6. Analysis of the PSDs at each operating condition follow.

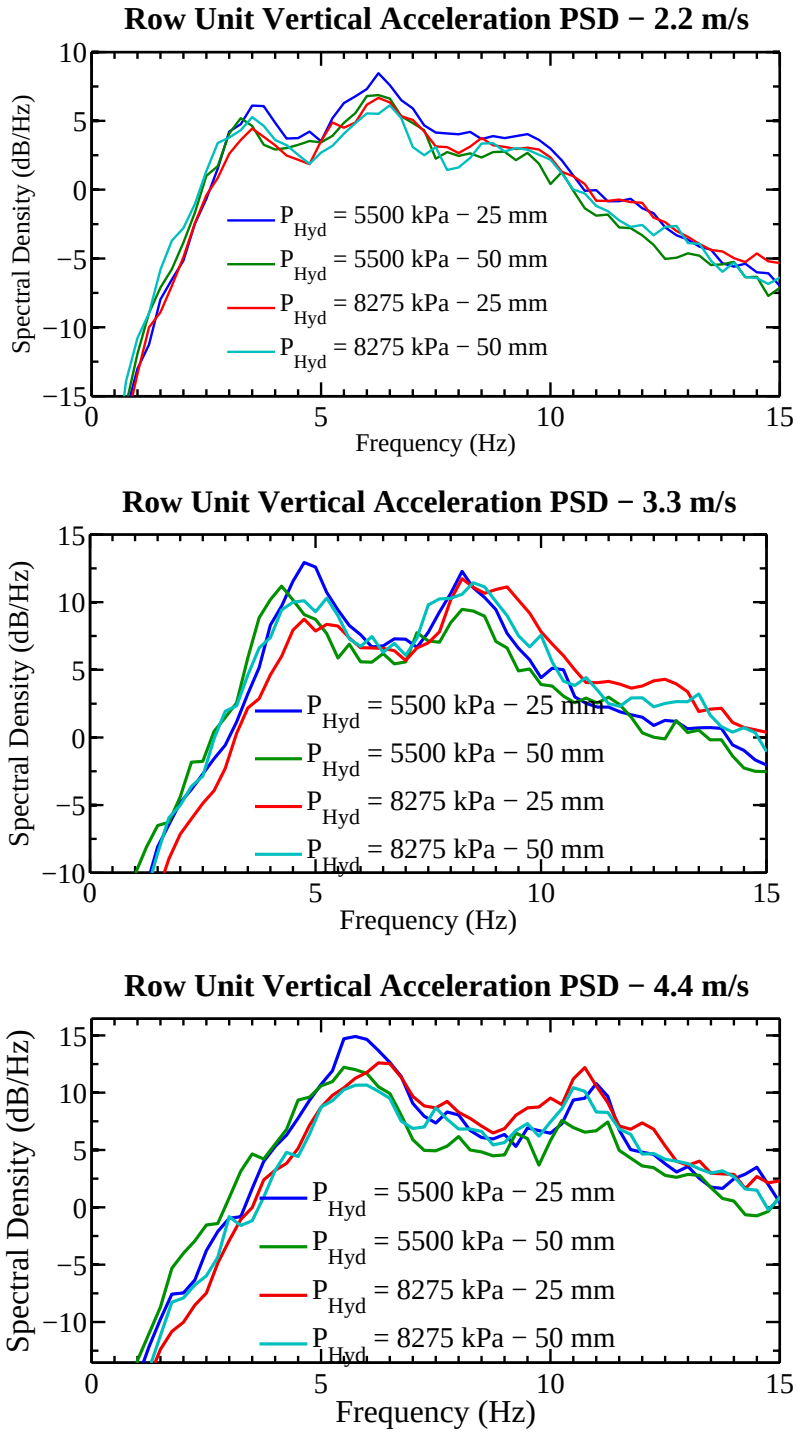

Figure 4.6: PSD of row unit acceleration comparing the effects of depth and hydraulic pressure changes at 2.2 m/s (top), 3.3 m/s (middle), and 4.4 m/s (bottom).

The high row unit acceleration at the 25 mm depth and P_{Hyd} = 5500 kPa condition is evident in Fig. 4.6 (top), which shows the PSDs of the row unit vertical acceleration in the four test configurations at 2.2 m/s. Between 3.25 and 10.5 Hz, the power measured in this configuration is greater than the power when either the pressure or depth is increased. Based on the insights gained from model development in Chapter 3, the two major peaks at 3.5 Hz and 6.25 Hz were caused by feedback between the hoe opener and packer wheel, and the furrow pass frequency of the previous seeding operation as discussed in Section 4.2.3, respectively. The lower frequency peak was a result of dynamic changes in hoe opener depth changing the terrain experienced by the packer wheel at a time delay related to the plot drill speed. The changes in packer wheel terrain then further affected the motion of the row unit, which caused changes in opener depth. Modelling insights also highlighted the speed-dependent nature of both of these peaks.

At 2.2 m/s, increasing hoe opener depth potentially shifted the lower response peak from between 3.5-3.75 Hz to 3.25 Hz, and generally reduced the response amplitude by about 1.5 dB overall when P_{Hyd} = 5500 kPa, and even more so when P_{Hyd} = 8275 kPa, when compared to the 25 mm depth and P_{Hyd} = 5500 kPa condition. Increasing hydraulic pressure while maintaining depth at 25 mm also reduced the overall amplitude of the response. However, the higher frequency amplitude (> 11 Hz) when P_{Hyd} = 8275 kPa is nearly unchanged from the results at the depth = 25 mm and P_{Hyd} = 5500 kPa condition. At 2.2 m/s, the lowest amplitude was achieved when P_{Hyd} = 8275 kPa in the 50 mm depth configuration (Fig. 4.5) evidently due to the reduced response near the furrow pass frequency peak in Fig. 4.6 (top).

Tillage forces are proportional to tool depth (Godwin and Spoor, 1977), and intuitively the magnitude of time-varying changes in tillage forces might also be expected to increase with tool depth, therefore, an increase in acceleration variance with depth was expected. However, the row unit appeared to be more effectively damped when the depth was increased to 50 mm in Fig. 4.6 (top) at both low and high hydraulic pressure settings. At the 50 mm depth setting, soil-tool contact area increased and more soil was present above the winged portion of the hoe opener (Fig. 2.4), compared to the 25 mm depth setting. Therefore, it was hypothesized that the hoe opener effectively dampens the motion of the row unit at a greater depth setting. This could be due to either an increase in soil-tool friction forces as

the contact area of the tool increased, and/or the increase in soil above the opener wing acts to anchor the wing portion of the hoe opener as the depth was increased. In addition to adhesion and anchoring effects, it would be expected that a deeper opener setting would loosen (and thus soften) a deeper cross-section of soil, lending to a more compliant terrain surface experienced by the packer wheel.

To explore differences in acceleration variance at 3.3 m/s, PSDs of measured row unit accelerations in several configurations are shown in Fig. 4.6 (middle). Similar to the 2.2 m/s data, increased opener depth resulted in a general downward shift of acceleration power below approximately 11 Hz, and a downward shift in frequency of the lower peak (again, related to feedback from the hoe opener terrain modification through the packer wheel) of about 0.5 Hz. Increasing depth reduced the amplitude of the two main peaks by 1.75 dB (4.25 Hz) and 2.8 dB (8.25 Hz), respectively, when $P_{hyd} = 5500$ kPa.

In contrast to the response from increased hydraulic pressure at 2.2 m/s, changing the hydraulic system pressure at 3.3 m/s without increasing depth only affected the amplitude of the low frequency (feedback) peak. The amplitude was reduced by approximately 4.2 dB, but the peak at 8.25 Hz (furrow input) remained basically unchanged. Furthermore, high-frequency response increased with increased hydraulic pressure at 3.3 m/s.

Row unit vibration PSDs measured at 4.4 m/s are shown in Fig. 4.6 (bottom). The response at $P_{Hyd} = 5500$ kPa and 25 mm depth was dominated by the opener-to-packer pass frequency peak at 5.75 Hz and the furrow pass frequency at 11 Hz. At this speed, increasing opener depth to 50 mm reduced the opener-to-packer pass frequency peak amplitude by about 2.7 dB, and suppressed the furrow pass frequency peak by 4.75 dB making this peak almost indistinguishable from the response at nearby frequencies. When the depth was maintained at 25 mm and the hydraulic pressure was increased to $P_{Hyd} = 8275$ kPa, the opener-to-packer peak was reduced by 2.3 dB and the amplitude of the furrow pass frequency peak *increases* by 1.6 dB. From Fig. 4.6, as the speed increases a higher hydraulic pressure generally resulted in an increased amplitude of the furrow pass frequency peak relative to the $P_{Hyd} = 5500$ kPa and depth = 25 mm operating condition at each speed.

At both 3.3 and 4.4 m/s, increasing both depth and pressure further suppressed the opener-to-packer frequency peak below that of the $P_{Hyd} = 5500$ kPa and depth = 25 mm

response. However, higher hydraulic pressure increased the amplitude of the furrow pass frequency peak above the peak at the same depth (50 mm) but lower hydraulic pressure (P_{Hyd} = 5500 kPa). Increasing the hydraulic pressure at this depth essentially traded off reduced opener-to-packer frequency response for increased response at the furrow frequency. This may explain why hydraulic pressure appeared to have little effect on acceleration variance values at the 50 mm depth in Fig. 4.5.

Although soil strength was not characterized with respect to furrow cross sectional profile, spatial dependency is probable. Inconsistencies such as remnants of the root system of plants previously seeded in the existing furrows were undoubtedly present near the center of the furrow. A tillage operation at a depth of 50 mm was more likely to remove these inconsistencies from the path of the packer wheel than when operating at 25 mm, particularly at higher speeds due to greater volumes of soil being moved and increased soil throw. Therefore, it was hypothesized that the reduction in the amplitude of the furrow pass frequency peak at the P_{Hyd} = 5500 kPa and depth 50 mm configuration in Fig. 4.6 (bottom) was due to more aggressive tillage resulting at a greater depth and speed.

Soil throw and furrow width are known anecdotally to increase with increased speed during tillage operations with hoe openers. This trend is likely due to the more aggressive tillage that results as speed increases. The packer wheel was wider than the opener, so more of the terrain experienced by the packer wheel was tilled as the cross-sectional area resulting from the opener increases with speed. The tillage process smoothed the furrows present from the previous seeding year, thus reducing the input at this furrow pass frequency.

The relative amplitudes of the two dominant peaks changed with speed and hydraulic pressure. To quantify this, the power in 0.5 Hz bands centered at both peaks was calculated and normalized by the total power in each test run to give a percentage-contribution of power from each peak. The difference in percentage-contribution between the furrow pass frequency peak and opener-to-packer peak is shown in Fig. 4.7. Positive values indicate the furrow pass frequency percentage contribution was larger than the opener-to-packer percentage contribution.

At 1.1 and 2.2 m/s, the larger power contributor was consistently the furrow pass frequency peak, and the relative contribution of this peak generally increased from 1.1 to 2.2

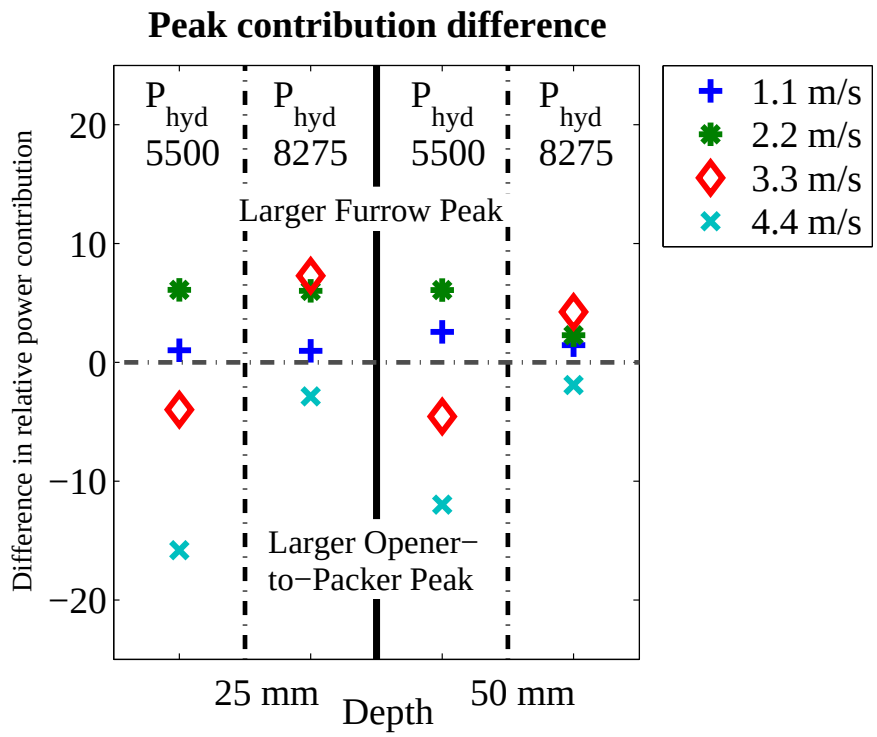

Figure 4.7: Difference in relative power contribution of each peak at the different operating conditions. Positive values indicate the percentage of power in the Furrow Peak is larger than the percentage of power of the Opener-to-Packer Peak.

m/s, however the configuration with $P_{Hyd} = 8275$ kPa and depth = 50 mm indicated relatively little sensitivity to speed. Above 2.2 m/s, sensitivity to hydraulic pressure was more apparent. Increasing the hydraulic pressure at 3.3 m/s shifted the largest power contribution from the opener-to-packer peak to the furrow pass frequency peak at both depths. At 4.4 m/s, increased pressure reduces the difference between peak contributions, but the opener-to-packer peak remained the larger contributor at all operating conditions.

Effects from increased hydraulic pressure appeared to be non-linear. Theoretically, increased hydraulic pressure was accompanied by a small increase in depth (due to increased static deflection of the packer wheel and increased static soil sinkage), so a result similar to increasing the depth setting of the row unit was expected. However, the changes in PSD characteristics summarized in Fig. 4.7 indicate that the effects of increased hydraulic pressure depend on the operating speed. Increased hydraulic pressure at higher speeds appeared to increase the vibration at the frequency of existing furrows in the terrain. This was possibly due to the deeper working depth of the opener resulting from greater packer wheel static

deflection and static sinkage, or it was a result of more subtle soil-tire interaction effects. The opener acts to homogenize the soil properties down to its working depth. If the suspected spatial dependency correlated with the presence of existing furrows was still present below this working depth, increasing the load on the packer wheel may have amplified spatial differences in terrain properties.

Consider an example of two hypothetical pressure-sinkage relationships plotted in Fig. 4.8, where P_1 is the pressure-sinkage relationship of firm soil (e.g., near an existing furrow), and P_2 is the pressure-sinkage relationship of a less firm soil (e.g., further from the existing furrow). Both curves are generated using Eq. (2.8). P_1 was generated using $k = 2500\ \frac{kPa}{m^n}$ and $n = 0.6$, and P_2 was generated using $k = 2600\ \frac{kPa}{m^n}$ and $n = 0.65$.

When a static pressure of P = 125 kPa is applied to both soil regions (representing an approximate soil contact pressure when $P_{hyd} = 5500$ kPa), a difference in static sinkage between P_1 and P_2 of $\Delta u = 0.0026$ m occurs. When the static pressure is increased to P = 150 kPa (representing soil contact pressure when $P_{hyd} = 8275$ kPa), the sinkage difference between the two regions increases to $\Delta u = 0.00325$ m: a static sinkage increase of 25% for a static pressure increase of only 20%.

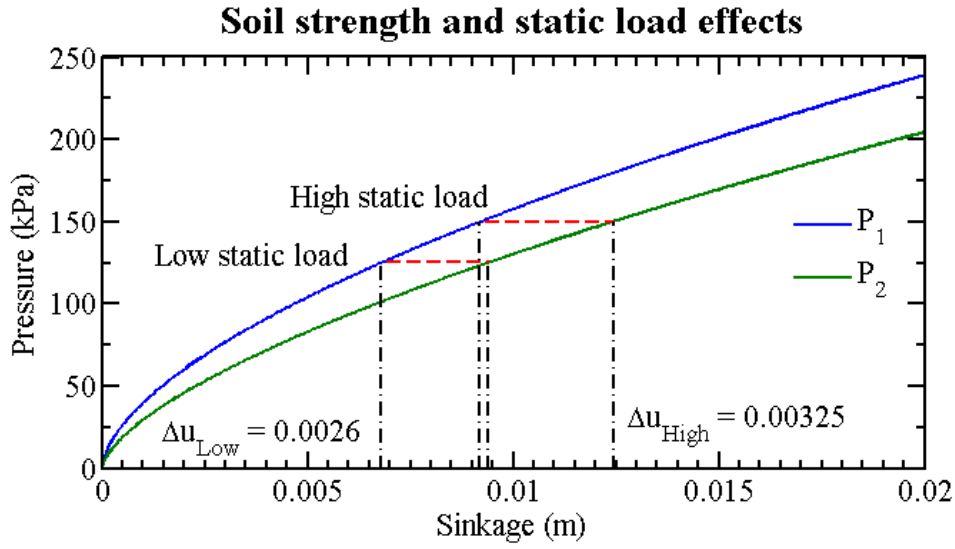

Figure 4.8: Changes in sinkage between two different hypothetical pressure-sinkage relationships, at two different static loads. Increased static load changes the amount of relative sinkage (Δu).

Although the spatial variation of soil strength was not quantified, and this simple example

assumes static conditions, the differences in Fig. 4.8 illustrate how increasing the static load on the row unit packer wheel by raising the hydraulic pressure could amplify the sinkage changes that a wheel experiences due to varying soil conditions. The variation in sinkage is a potential source of excitation to the row unit.

The complexity of interaction between the packer wheel and tilled soil was further highlighted by trends in the packer wheel reaction force measured by the load cell shown in Fig. 4.2. Mean values of the packer wheel reaction force from the steady state portion of the measurement run are presented in Fig. 4.9. Values are negative in sign due to the compression of the load cell when hydraulic cylinder forces are applied to the row unit.

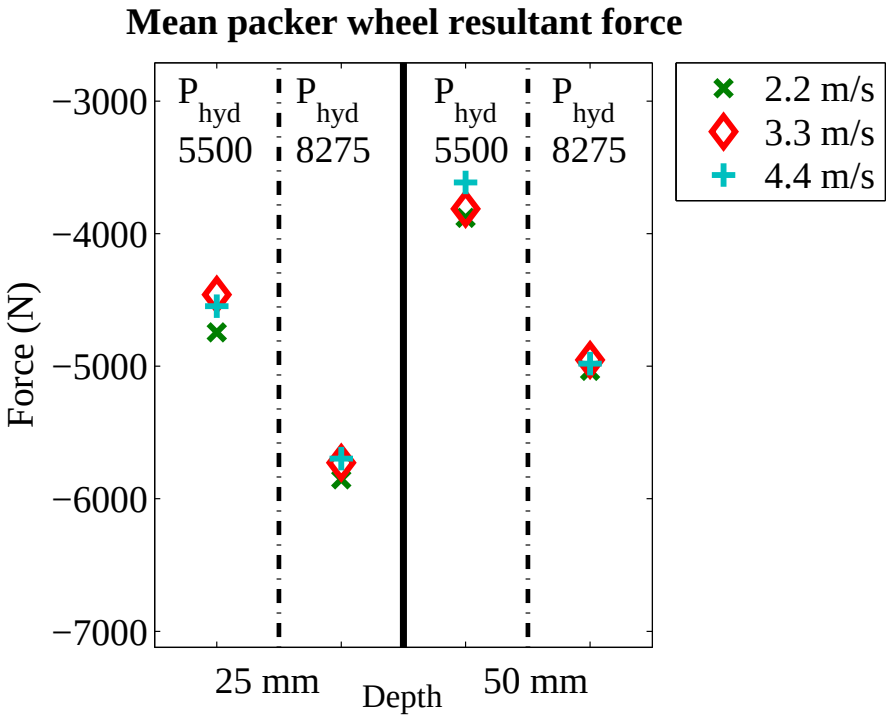

Figure 4.9: Mean values of the packer wheel reaction force measured via the load cell installed on the row unit. Mean values are grouped by speed (symbol), geometric depth setting (L/R), and hydraulic system pressure (column).

As expected, mean reaction forces increased in magnitude when the hydraulic pressure was increased. The average increase in the magnitude of the mean reaction force due to hydraulic pressure increase was approximately 1200 N. Across all depths and pressures, the mean values at 2.2 m/s were the largest in magnitude, and generally decreased as speed increased. Changing the hoe opener depth from 25 mm to 50 mm decreased the magnitude

of the packer wheel reaction force by an average of approximately 800 N. The decrease in the magnitude of the reaction force at the greater depth was likely due to two factors:

1. The increased tillage depth loosened more soil in the furrow, reducing the rolling resistance force experienced by the packer wheel;

2. The increased lift and draft forces on the tillage tool reducing the reaction force at the packer wheel. The opener lift forces directly reduce vertical packer wheel reaction force. The magnitude of the effect of draft forces depends on the angle of the parallel links of the row unit.

The installed instrumentation did not facilitate directly measuring the forces acting only on the hoe opener, so the simulation tool was used to explore soil-tool force effects. In addition to minimizing the opener-to-packer-wheel feedback, the model was modified such that forces at the soil-tool interface were ignored. These results were compared to simulations where soil-tool forces were included. Identical row unit terrain profiles were used between these two simulations, and inputs to the other tires were set to 0. Similar to other simulations where feedback was minimized, the opener still performed the averaging operation to smooth the terrain experienced by the packer wheel (see Section 3.4.3 for details of the terrain modification model).

The effect of hoe opener forces on packer wheel reaction force was evident when packer wheel reaction forces were compared between the two simulation trials. Similar to the measurement data where depth was increased, including soil tool forces reduced the average packer wheel reaction force compared to the simulation where soil-tool forces were ignored. The PSDs of the row unit vertical acceleration (not presented) were nearly identical; the variance of the row unit's vertical acceleration was reduced by approximately 2% when the soil-tool forces were not included in the dynamic simulation of the plot drill.

In comparison, when the simulation was modified to minimize the feedback between the packer wheel and the opener, the row unit acceleration variance was reduced by approximately 42% compared to simulation results where the feedback mechanism was included. The reduced high frequency agreement between simulation and measurement results likely biased this difference upward because the simulated feedback peak accounted for a larger

percentage of the total acceleration variance compared to the measurement data. Regardless of exact magnitudes, the motion of the row unit appeared to be dominated by poorly attenuated displacement inputs to the packer wheel.

4.3.2 Frame motion

Further inspection of the row unit schematic in Fig. 2.3 reveals that, although the row unit can move independently of the subframe, rotation of the subframe will effect the row unit's motion. Additionally, friction in the link connection points will act to couple the row unit and subframe motion. Friction within the row unit hydraulic cylinder, along with fluid resistance in the components of the hydraulic circuit will also couple these two bodies together. Therefore, motion of the frame was considered for further analysis.

Similar to the row unit, vertical vibration of the subframe measured by an accelerometer near the tail wheel increased with speed. Acceleration variance results are shown in Fig. 4.10; although the amplitudes were approximately 1 order of magnitude less than those of the response of the row unit (Fig. 4.5), a general trend of increased vibration with higher speed was evident. Therefore, a high degree of coupling between the row unit and subframe would be detrimental to row unit performance at high speed.

To investigate how frame motion and inputs to the frame wheels (walking axle and tail) affected row unit motion, the previously-developed dynamic model of the plot drill was used because knowledge of the time-domain input terrain was required. Simulations were performed at 2.2 m/s where terrain inputs were provided to only one input location; all other terrain profiles were set to flat terrain. Row unit vertical acceleration PSDs from the different simulations are shown in Fig. 4.11. Separate simulations with terrain inputs at the walking axle wheels, tail wheel, and opener/packer wheel are shown, along with the response when inputs were provided to all locations (the typical simulation input).

The response of the row unit when terrain input was only present at the hoe-opener/packer wheel was very similar to the response when terrain inputs are provided to all wheels. Differences near the estimated boom natural frequency (3 Hz), subframe natural frequency (4.25 Hz), and furrow pass frequency (6 Hz) were present. The largest difference between the "all wheel" and "row unit only" input conditions occurred at the subframe natural frequency.

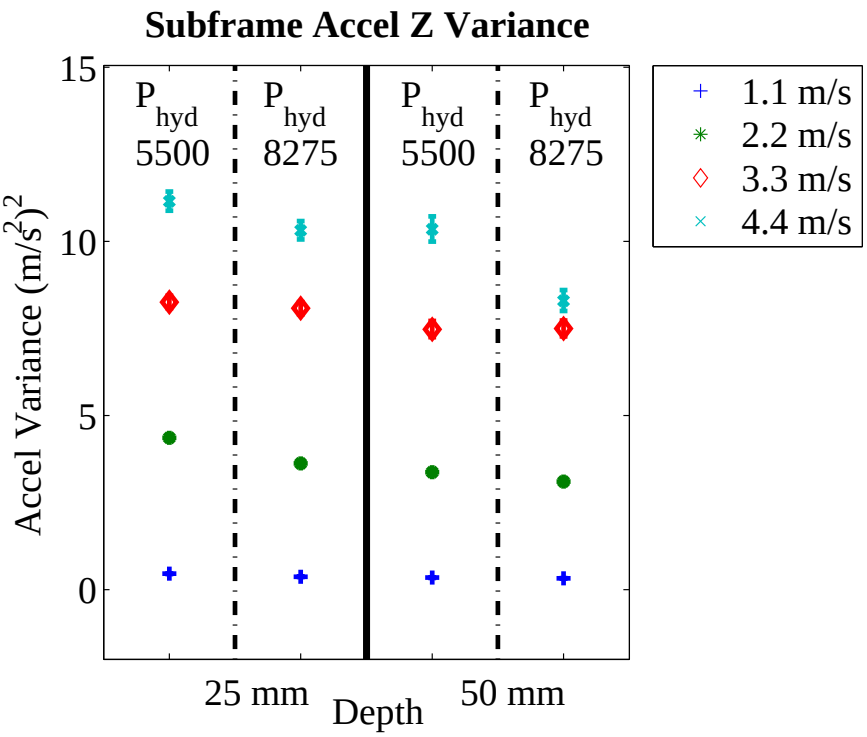

Figure 4.10: Variance of the measured subframe vertical acceleration in a coordinate system fixed to the subframe, grouped by speed (symbol/colour), geometric depth setting (L/R), and hydraulic system pressure (column). Error bars indicate the 95% confidence interval of the variance estimate.

Rotation of the subframe causes row unit rotation due to the parallel linkage mounting system, so it was expected that tail wheel excitation would result in row unit vibration (Fig. 4.11 - red line). However, considering the logarithmic vertical scale of Fig. 4.11, the modelled response of the row unit attributed to inputs at the tail and walking axle wheels was negligible compared to the row unit response when the opener and packer wheel were exposed to varying terrain; the acceleration variance under 11 Hz from tail wheel inputs only was less than 1% of the acceleration variance experienced from opener and packer wheel inputs. While the response was small, simulation results indicated that the row unit appeared to be more sensitive to terrain inputs at the tail wheel than at the walking axle wheels.

As the exact terrain of the test field was unknown, direct input/output relationships could not be computed from measurement data, and measuring the row unit response from isolated inputs was not possible. Differences between simulated and measured natural frequencies were noted in Chapter 3 and damping parameters were estimated during model

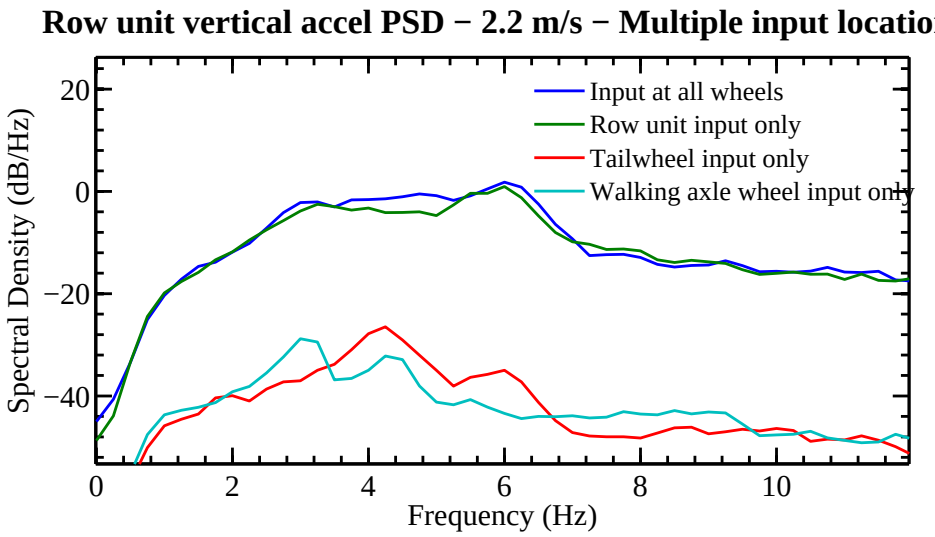

Figure 4.11: Simulated vertical acceleration response of the row unit. Results from simulations with single inputs at the opener and packer wheel, tail wheel, and walk axle wheels, along with terrain inputs at all tires are shown.

development, so cross-spectral characteristics were computed between measured signals as a final check of frame/row unit coupling. Multiple inputs and internal feedback mechanisms were present in the actual system, so caution is needed in interpreting causation from cross-spectral quantities. For power spectrum $G_{xx}(f)$ and $G_{yy}(f)$, the magnitude-squared coherence between signals x and y is given by

$$\gamma^2_{xy}(f) = \frac{|G_{xy}(f)|^2}{G_{xx}(f)G_{yy}(f)}$$

where G_{xy} is the cross-spectrum between signals x and y (Bendat and Piersol, 1986).

Magnitude-squared coherence values (γ^2) between the acceleration of the row unit and the boom are presented in Fig. 4.12 from data measured at 3.3 and 4.4 m/s. In general, coherences between the row unit and boom accelerations were low. Uncorrelated random signals have a coherence function value of 0. Conversely, a system whose output is completely related to the input through a linear time-invariant system corresponds to $\gamma^2 = 1$. The horizontal dashed lines in Fig. 4.12 indicate an average maximum spurious coherence based on a 95% confidence level. From Bendat and Piersol (1986), coherence values between 0 and 1 indicate results from three possible situations: noise is present in the input and/or output measurements, the system is non-linear, and/or the system output is due to the input

considered and other inputs.

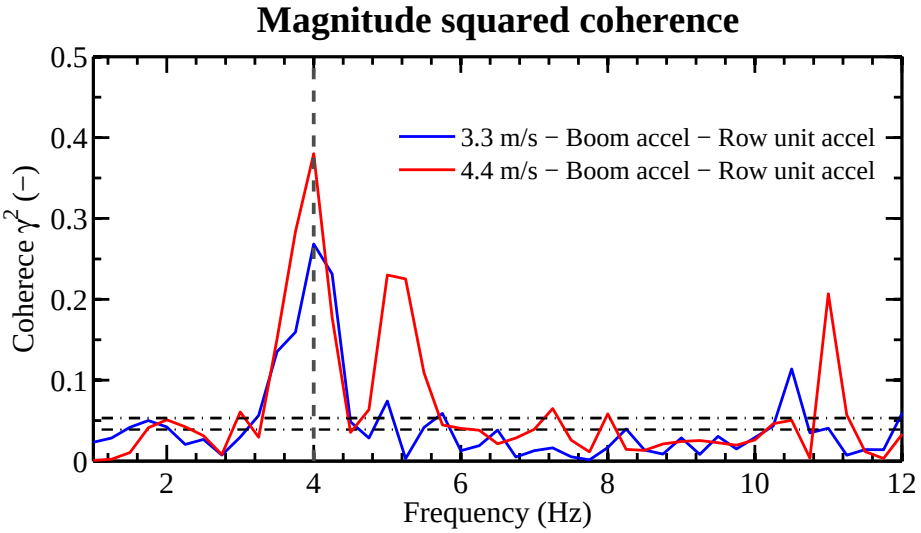

Figure 4.12: Measured row unit acceleration coherences with the boom accelerations at 3.3 and 4.4 m/s.

Based on Fig. 4.12, the acceleration of the row unit was generally uncorrelated with the acceleration of the plot drill boom. Increased correlation was present near 4 Hz at both speeds; therefore, if there is a risk of coupling between the boom and row unit, it appears to be near 4 Hz. Coherence between the row unit and boom acceleration was greater at 4.4 m/s compared to 3.3 m/s, however this does not prove that boom motion *causes* the row unit vibration at this frequency. Although the threshold is typically application-dependent, a γ^2-value of at least 0.5 is often used as a cutoff for further interpretations of potential causality.

The peak in the coherence signals did align with the peaks in the PSDs of the vertical boom acceleration shown in Fig. 4.13 (vertical dashed lines are located at 4 Hz in both Figs. 4.12 and 4.13), as the measured natural frequency of the boom was near 4 Hz. Due to the geometry of the drill, vertical motion of the boom resulted in motion of the subframe/boom pivot point. While coupling with the frame should not be interpreted as the main cause of row unit vibration at high speeds, it is a mode of row unit excitation that should continue to be managed and minimized in future equipment designs.

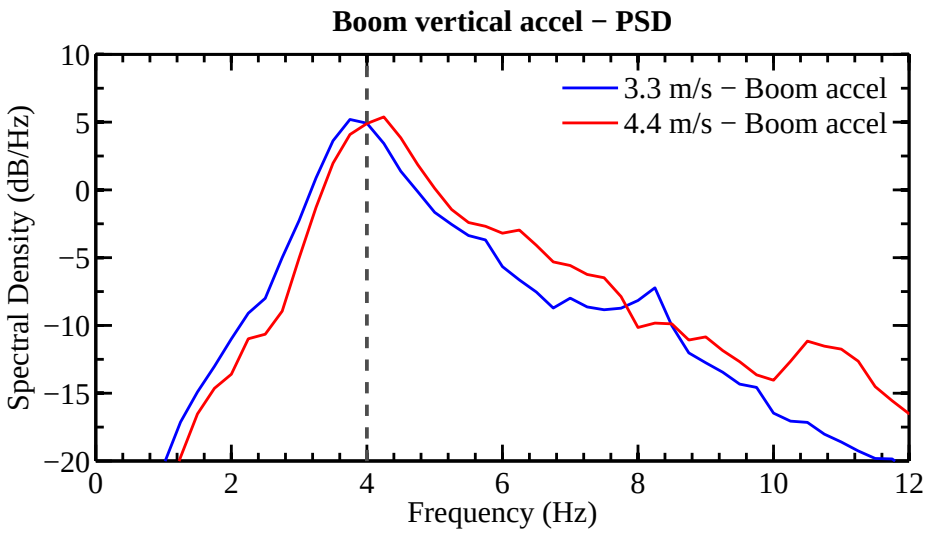

Figure 4.13: Measured boom vertical acceleration PSDs at 3.3 and 4.4 m/s, P_{Hyd} = 5500 kPa, depth = 25 mm.

4.3.3 Qualitative comments on plant residue effects

A fundamental aspect of minimum-tillage farming systems includes leaving a significant amount of plant residue on the terrain surface after harvest to preserve moisture and provide organic matter to improve soil conditions. However, if this plant residue cannot break down sufficiently before seeding (typically the following spring), it can collect among the hoe opener arms and packer wheels of a seeding drill. This leads to poor surface finish, seed placement problems, and issues with the pneumatic conveying of seed to the hoe opener as large clumps of plant residue are dragged through the field beneath the seeding implement.

While severe plugging of residue among row units did not occur during testing, existing plant residue can effect row unit motion as smaller clumps of the material pass beneath the seed drill frame. The ability for the machine to maintain consistent depth in challenging residue conditions is important characteristic of machine performance. The model presented in Chapter 3 did not represent residue on the terrain surface.

The formation and release of residue clumps around the hoe opener is evident in Figs. 4.14-4.18. These images were extracted for further analysis from test video collected at 2.2 m/s. A residue clump forms near the start of the sequence, and is then released, passing under the packer wheel and causing upward motion of the row unit. The selected frames captured

the opener-packer wheel feedback phenomenon present in the acceleration data. The elapsed time between the first and last video frame presented was approximately 1 second.

Figure 4.14: The hoe opener before crop residue started accumulating residue is shown in the top image. The opener begins to push residue along the soil surface in the bottom image as an area of heavier residue was encountered.

Figure 4.15: Residue continued to collect and extend up the front of the opener. The clump became wider in the top image. The residue clump began to release and pass alongside the opener in the bottom image.

Figure 4.16: The clump was pulled from the opener in the top image. The row unit began to move upward in the bottom image as the packer wheel engaged the residue.

Figure 4.17: The row unit has moved upward as the packer wheel passes over the residue clump in the top image. The red circle marks the longitudinal location where the row unit is at its maximum position. In the bottom image, the row unit has started to move downward as the packer wheel has completely passed over the residue clump. A gap between the upper row unit link and the frame member in the background is visible in this lower position. The packer wheel has not yet reached the marked straw stalk in the bottom image.

Figure 4.18: As the packer wheel reached the point were the row unit was previously at its maximum height while passing over the residue clump, the row unit began to move upward. In the bottom image, the packer wheel has passed the marker stalk and has moved downward again.

Based on the images presented in Figs. 4.14-4.18, residue clumps appeared to create additional variability in the terrain experienced by the packer wheel. A test field with less residue likely would result in less row unit motion because the packer wheels would not be forced to pass over these new terrain features. The passage of the packer wheel over the residue clump in Figs. 4.14-4.18 further highlighted the feedback mechanism between the hoe opener and packer wheel. The clumping and eventual release of the residue from the row unit was a consistent aspect of row unit response, but without underlying regular periodicity, the process does not cause distinguishable PSD peaks in the acceleration data; rather, the overall amplitude would increase due to the random presence of residue clumps.

The neglected effect of residue, and its potential to increase the input amplitudes experienced by the packer wheel, may explain generally lower-than-measured row unit acceleration presented in the model results and discussion of Section 3.6. Without the apparent random inclusion of simulated plant residue clumps into the path of the packer wheel, the under-excited response of the simulated row unit was expected.

4.4 Conclusion

As productivity demands of seeding equipment increase, a better understanding and a greater predictive capability of the dynamic performance of seeding implements during their design phase will be required to ensure consistent seeding depth at greater operating speeds. To support these demands, data were collected from a hoe-opener plot drill based on a production model of a New Holland Agriculture P2070 Precision Hoe Drill while in operation in typical seeding conditions in western Canada at speeds ranging from 1.1 to 4.4 m/s. The time-varying position and acceleration of several points on the plot drill were recorded, along with resultant packer wheel force.

Opener depth setting and the system hydraulic pressure have subtle effects on the motion of the row unit and frame; increased speed was the largest contributor to increased row unit motion by a significant margin. In general, the majority of row unit motion appeared to be caused by poor attenuation of the displacement inputs to the row unit (particularly to the packer wheel) that arise from operating in the varying terrain of agricultural fields.

Specifically, the effects stemming from the feedback system created by rigidly coupling the packer wheel behind the row unit body were particularly detrimental to the depth consistency performance of the row unit at high speed. The collection and release of plant residue clumps at the hoe opener created another source of displacement input for the packer wheel beyond the rough terrain surface. The non-linear interaction between speed and the system hydraulic pressure highlights the complex nature of the terrain modification and furrow backfill processes occurring at the hoe opener.

Acknowledgment

Funding contributions from CNH Industrial and Natural Sciences and Engineering Research Council of Canada (NSERC) toward this work are gratefully acknowledged. Assistance from Joel Gervais of CNH Industrial - Saskatoon test equipment preparation was greatly appreciated.

Chapter 5

Project conclusion and recommendations

5.1 Conclusion

The demands placed on the modern food production system continue to grow with increasing global population. Growth of farm size in western Canada also continues to push the productivity expectations of seeding equipment by farm managers and agricultural equipment manufacturers. Increased equipment speed will be the primary means of increasing equipment productivity as the physical limitations of equipment size are approached.

To support this broad goal of increasing equipment operating speed, three major objectives were established to guide this research, namely

1. develop a mathematical simulation tool to be used in predicting the motion of a seeding implement as it operates in an agricultural field;

2. deasure the dynamic motion of a seeding implement when operating at different speeds; and

3. develop an understanding of the mechanism(s) that cause depth consistency problems at higher speed.

To meet Objective #1, a simulation tool was developed in MATLAB® (The Mathworks, Inc., 2014) to model the 2-D motion of a simplified seeding implement while operating in an agricultural field; this was presented in Chapter 3. The sub-models for describing soil-opener and soil-tire contact were developed from the background literature presented in Chapter 2. Simulation results were compared to a measured data set. To meet the Objective #2, measurement data of the modelled machine were acquired, with testing details given in

Chapter 4; differences resulting from varying the operating parameters of the equipment were discussed. The developed simulation tool recreated several distinct features present in the measurement data. In pursuit of Objective #3, two major mechanisms of row unit vibration were identified by using both the simulation tool and the measurement data; specifically these mechanisms were:

- Periodic inputs from existing furrows in the terrain were evident in the resulting motion of the row unit. The small, stiff packer wheel provided the only compliance between the soil and the row unit, and little damping was present to absorb the kinetic energy of the row unit. Thus, the row unit was unable to effectively attenuate the terrain inputs. As seeding speed increased, so too did the amplitude of row unit vibration during both simulation and testing.

- Feedback at the pass frequency related to the opener-packer wheel separation distance tended to increase with seeding speed. This mechanism was due to the packer wheel encountering bumps created by the hoe-opener; because both components were rigidly coupled to the row unit, additional bumps were created as the packer wheel passed over previous bumps, and the feedback cycle continued.

Rather than pursue one possible design solution to improving depth consistency, this further understanding of row unit dynamics and the subsequent simulation tool that was developed gives equipment designers the capability to compare possible design strategies early in the prototype phase of equipment development.

5.2 Research limitations

As the intention of this model was to augment the simulation capabilities that are available for early-phase equipment design, simplifications were required to maintain model usability. Therefore, an understanding of these simplifications is required to ensure appropriate use of the model.

The origin of the Bekker soil-tire interaction model was in the quasi-static determination of the empirical pressure-sinkage relationship of a given soil. Data were usually acquired

at low penetration rates, which do not capture the rate-dependency that soil strength typically exhibits. Grahn (1991), with later implementation work by Fassbender et al. (1997), presented an advanced Bekker-based model where sinkage rates were considered. However, determining the additional coefficients for this model would require greater data collection efforts prior to model use, and test equipment capable of these increased penetration rates. Acquiring these parameters was beyond the scope of this work. Given that the dynamic response of the machine was a primary interest of the modelling efforts, incorporating velocity dependence in the soil-tire interaction model should be explored.

The damping parameters used when generating the simulation results were estimated based on similar values in the literature with adjustments made to obtain reasonable model performance. Sensitivity in some ranges of the damping and friction values were evident during model development, therefore inaccuracy in these values could potentially have significant effects on the effectiveness of the simulation tool. For example, the presence of a peak in the subframe response related to the natural frequency of the boom is evident in the simulated subframe response in Fig. 3.11, but this feature was absent in the measured data. With improved damping parameters, future simulation results should more closely match the measurement data.

During ideal operation, as the opener passes through the soil, failed soil passes around the sides of the opener and fills the furrow, covering the seed before being compressed by the packer wheel to improve soil-to-seed nutrient and moisture transfer. Even at low speeds, soil density and other characteristics of the loosened, failed soil are modified by the passage of the hoe opener. Additionally, the terrain which the packer wheel experiences is certainly different than the original terrain through which the knife passed. The first order model presented in Section 3.4.3 is a heuristic approach to describing the packer wheel terrain based on qualitative analysis and anecdotal observations. While this approach provided reasonable success in replicating the feedback phenomenon through this initial stage of model development, this heuristic approach may not extrapolate to other operating conditions. To the authors' knowledge, explicit methods of predicting the terrain profile experienced by the packer wheel are absent in the literature, save for DEM; however, Solhjou et al. (2012, 2013) present changes in soil trans-location tendencies with varying opener rake angle and

geometry. Furthermore, video observations, anecdotal operator comments, and work by Hasimu and Chen (2014) on characterizing the soil throw tendencies of different opener designs would indicate the amount of soil that remains in the furrow is dependent on tool geometry, velocity, and soil conditions. This indicates the complexity of characterizing and predicting the soil flow characteristics of a given tillage tool design in a particular operating environment.

The presence of crop residue had an obvious effect on the operation of the row unit as evidenced by the large vertical displacement of the row unit resulting from the inclusion of plant residue in Section 4.3.3. Predicting the complex nature of machine-residue interaction was deemed outside the scope of this work, but the effects are undeniable, and discrepancies between measured and simulated performance should be expected when plant residue has an observable effect. However, if the presence of residue only results in larger effective terrain inputs to the packer wheels, insights from the model can still be useful in evaluating row unit performance to a limited extent.

A lack of row unit damping was highlighted during model development. While some of the unaccounted damping can be attributed to joint friction, hydraulic components, and uncertainties at the packer wheel, the simple representation of the interaction between the opener and soil may also have contributed to discrepancies in modelled results. Classical soil-tool models do not account for the effects of a tool having a vertical (sinkage) velocity. Resistance to the motion of the tool entering or exiting the soil vertically is probable, but unaccounted for by the basic models in the literature. Adhesion stress acting on the sides of the tool was introduced in this work to counter tool plunging effects with the desired damping outcome evident in the simulation results, but frictional and velocity-related stresses may also be appropriate to include.

5.3 Recommendations for future research

Considering the limitations outlined previously, several opportunities for future research exist, namely

- advanced parameter collection to improve model fidelity. This could include parameters for implementing the velocity-dependent soil-tire contact model by Grahn (1991), characterizing terrain profiles for minimum-tillage field surfaces in western Canada, and quantifying the damping characteristics of packer and frame tires.

- An improved understanding and characterization of furrow shape and backfill characteristics as a function of soil-engaging tool geometry would benefit the fidelity of the simulation tool and designers of these soil-engaging components. As computational power and numerical methods advance, using DEM to predict the resulting furrow shape and complex effects of an opener with a vertical velocity component may prove highly beneficial to model accuracy.

- Crop residue effects were not addressed but observed in the video data. Future work quantifying the effect that the presence or removal of residue has on row unit vertical motion would benefit future designs given the likelihood of continued no-till farming practices in western Canada.

Considering the volume of data collected and the significant instrumentation required to capture the motion of the plot drill, several opportunities for improving data collection were also noted, including

- further analysis of the video collected during test operation to potentially quantify soil and plant residue flow characteristics, and the kinematic response of the row unit (reducing future instrumentation burdens). Additionally, stereo imaging or other profilometry techniques could be leveraged in a future test apparatus to capture the terrain profile experience by the each row unit during physical tests;

- instrumentation improvements to measure packer wheel center forces and hoe-opener forces in three directions to allow further validation of the soil-tire and soil-tool submodels; and

- development of on-board depth measurement techniques that can deal with local terrain variation and the 3-D movement of the implement relative to the terrain. Improvements

in this instrumentation area could lessen the burden of labour-intensive seed digs to verify the operating depth of the openers.

5.4 General design recommendations

While frame/row unit redesign was outside of the objectives of this work, several aspects of general design improvement were noted during the course of this research:

- including spring/damper elements in the design to improve attenuation of inputs from the terrain and absorb the kinetic energy of the row unit to reduce vibration amplitude,
- decouple the packer wheel from the hoe opener to reduce the feedback phenomenon identified by introducing additional compliance between the packer wheel and row unit body, and
- decouple the packer wheel inputs from the hoe opener terrain modification by depth-gauging with a wheel in front of the hoe opener.

With appropriate modification, the dynamic model presented in this work could be used to explore the potential benefits of these suggested design changes, before physical prototyping resources are dedicated to experimental evaluation.

References

Ahmed, O. B., Goupillon, J. F., Jan. 1997. Predicting the ride vibration of an agricultural tractor. Journal of Terramechanics 34 (1), 1–11.

Armin, A., Fotouhi, R., Szyszkowski, W., 2014. On the FE modeling of soil-blade interaction in tillage operations. Finite Elements in Analysis and Design 92, 1–11.

ASTM International, 2011a. Direct shear test of soils under consolidated drained conditions. Tech. Rep. D3080, ASTM International.

ASTM International, 2011b. Standard test method for consolidated drained triaxial compression test for soils. Tech. Rep. D7181, ASTM International.

ASTM International, 2011c. Standard test method for consolidated undrained triaxial compression test for cohesive soils. Tech. Rep. D4767.

ASTM International, 2016. Standard test method for mechanical cone penetration tests for soil. Tech. Rep. D3441, ASTM International.

Bekker, M. G., 1956. Theory of land locomotion;the mechanics of vehicle mobility. Ann Arbor,.

Bekker, M. G., 1960. Off-the-road locomotion; research and development in terramechanics. University of Michigan Press, Ann Arbor.

Bekker, M. G., 1969. Introduction to terrain-vehicle systems. The University of Michigan Press, Ann Arbor.

Bendat, J. S., Piersol, A. G., 1986. Random data: analysis and measurement procedures. John Wiley & Sons.

Bernstein, R., 1913. Problems of experimental mechanics of motor ploughs. Der Motorwagen 16.

Canola Council of Canada, 2014. What are some factors that impact canola emergence? URL http://research.canolacouncil.org/database-queries?id=8

Chen, Y., Gao, Q., Zhou, H., Sadek, M. A., 2015. Simulation of soil dynamic properties of a seed opener using the discrete element method (dem). Agricultural Engineering International: CIGR Journal 17 (3).

Chi, L., Kushwaha, R., 1989. Finite element analysis of forces on a plane soil blade. Can. Agr. Eng. 31 (2), 135–140.

Chi, L., Kushwaha, R., 1991. Finite element analysis of soil forces on two shapes of tillage tool. Can. Agr. Eng. 33 (1), 39–45.

Chi, L., Kushwaha, R., 1993. Nonlinear 3-D finite element analysis of soil forces on curved tillage tools. Can. Agr. Eng. 35 (1), 11–15.

Cosin Scientific Software, 2014. FTire - Flexible ring tire model: Modelization and parameter specification. Tech. rep., Cosin Scientific Software, Munchen, Germany.

Cosin Scientific Software, 2016. FTire Parameterization: Proposed measurement and data processing procedures for use with FTire/fit. Tech. rep., Cosin Scientific Software, Munchen, Germany.
URL https://www.cosin.eu/wp-content/uploads/ftire_param.pdf

Coulomb, C. A., 1776. Essai sur une application des règles de maximis & minimis à quelques problèmes de statique, relatifs à l'architecture. De l'Imprimerie Royale.

Cowell, P. A., 1969. Automatic control of tractor mounted implements - an implement transfer function analyser. J. Agr. Eng. Res. 14 (2), 117–125.

Crolla, D. A., Horton, D. N. L., Stayner, R. M., 1990. Effect of tyre modelling on tractor ride vibration predictions. J. Agr. Eng. Res. 47, 55–77.

Dwyer, M. J., Crolla, D. A., Pearson, G., 1974. An investigation of the potential for improvement of tractor draught controls. J. Agr. Eng. Res. 19 (2), 147–165.

Fassbender, F. R., Fervers, C. W., Harnisch, C., 1997. Approaches to predict the vehicle dynamics on soft soil. Vehicle System Dynamics 27, 173–188.

Gan, Y. T., Miller, P. R., McDonald, C. L., 2003. Response of kabuli chickpea to seed size and planting depth. Canadian Journal of Plant Science 83 (1), 39–46.

Godwin, R. J., Spoor, G., 1977. Soil failure with narrow tines. J. Agr. Eng. Res. 22 (3), 213–228.

Goriatchkin, B., et al., 1936. Tieoria i proisvodstvo sielskohosiaynik mashin (Theory and production of agricultural equipment). Moscow, USSR.

Government of Alberta Agriculture and Rural Development, 2002. Cereal seeding depth.
URL http://www1.agric.gov.ab.ca/$department/deptdocs.nsf/all/crop4690

Grahn, M., Jan. 1991. Prediction of sinkage and rolling resistance for off-the-road vehicles considering penetration velocity. J. Terramech. 28 (4), 339–347.

Groves, P., 2015. Navigation using inertial sensors [Tutorial]. IEEE Aerospace and Electronic Systems Magazine 30 (2), 42–69.

Harker, K. N., O'Donovan, J. T., Blackshaw, R. E., Johnson, E. N., Lafond, G. P., May, W. E., 2012. Seeding depth and seeding speed effects on no-till canola emergence, maturity, yield and seed quality. Canadian Journal of Plant Science 92 (4), 795–802.

Harnisch, C., Lach, B., Jakobs, R., Troulis, M., Nehls, O., 2005. A new tyre-soil interaction model for vehicle simulation on deformable ground. Vehicle System Dynamics 43 (1), 384–394.

Hasimu, A., Chen, Y., 2014. Soil disturbance and draft force of selected seed openers. Soil and Tillage Research 140, 48–54.

Hettiaratchi, D. R. P., Witney, B. D., Reece, A. R., 1966. The calculation of passive pressure in two-dimensional soil failure. J. Agr. Eng. Res. 11 (2), 89–107.

Janosi, Z., Hanamoto, B., 1961. The analytical determination of drawbar pull as a function of slip for tracked vehicles in deformable soils. In: First International Conference on Terrain-Vehicle Systems, Turin, Italy.

Jazar, R. N., 2013. Vehicle dynamics: theory and application. Springer Science & Business Media.

Kushwaha, R. L., Linke, C., 1996. Draft-speed relationship of simple tillage tools at high operating speeds. Soil Tillage Res 39 (12), 61–73.

Kushwaha, R. L., Shen, J., 1995. Finite element analysis of the dynamic interaction between soil and tillage tool. Transactions of the ASAE 37 (5), 1315–1319.

Lagarias, J. C., Reeds, J. A., Wright, M. H., Wright, P. E., 1998. Convergence properties of the NelderMead simplex method in low dimensions. SIAM Journal on optimization 9 (1), 112–147.

Laib, L., 1977. Measurement and mathematical analysis of agricultural terrain and road profiles. J. Terramech. 14 (2), 83–97.

Lines, J., Peachey, R., 1992. Predicting the ride vibration of a simple unsuspended vehicle. J. Terramech. 29 (2), 207–221.

Lines, J. A., Murphy, K., 1991a. The radial damping of agricultural tractor tyres. J. Terramech. 28 (23), 229–241.

Lines, J. A., Murphy, K., 1991b. The stiffness of agricultural tractor tyres. J. Terramech. 28 (1), 49–64.

Lines, J. A., Peachey, R. O., Collins, T. S., 1992. Predicting the ride vibration of an unsuspended tractor using the dynamic characteristics of rolling tyres. J. Terramech. 29 (3), 307–315.

Mak, J., Chen, Y., Sadek, M., 2012. Determining parameters of a discrete element model for soil–tool interaction. Soil and Tillage Research 118, 117–122.

Mathews, J. H., Fink, K. D., 2004. Numerical methods using MATLAB, 4th Edition. Prentice hall Upper Saddle River, NJ.

McKyes, E., 1989. Agricultural Engineering Soil Mechanics. Else.

McKyes, E., Ali, O., 1977. The cutting of soil by narrow blades. J. Terramech. 14 (2), 43–58.

Nakashima, H., Oida, A., 2004. Algorithm and implementation of soil-tire contact analysis code based on dynamic FE-DE method. J. Terramech. 41 (2-3), 127–137.

New Holland Agriculture, 2010. P2070 Precision Hoe Drill Sales Information. URL http://agriculture.newholland.com/us/en/Products/Seeding-and-Application-Equipment/Air-Hoe-Drills/Documents/P2070_2010.pdf

Obermayr, M., Dressler, K., Vrettos, C., Eberhard, P., Oct 2011. Prediction of draft forces in cohesionless soil with the discrete element method. Journal of Terramechanics 48 (5), 347–358.

O'Callaghan, J., Farrelly, K., 1964. Cleavage of soil by tined implements. J. Agric. Engng Res. 9 (3), 259.

Okello, A., 1991. A review of soil strength measurement techniques for prediction of terrain vehicle performance. J. Agric. Eng. Res. 50, 129–155.

Olson, D. J., Weber, J., 1965. Effect of speed on soil failure patterns in front of model tillage tools. Tech. rep., SAE Technical Paper.

Owen, G. T., McRae, K. B., McRae, S. M., Misener, G. C., 1990. Spectral analysis of subsoiling forces with a rigid tillage tool. Can. Agr. Eng. 32 (1), 57–62.

Park, S., Popov, A. A., Cole, D. J., 2004. Influence of soil deformation on off-road heavy vehicle suspension vibration. J. Terramech. 41 (1), 41–68.

Paulson, I. W., Noble, S. D., Dolovich, A. T., 2016. Seeding equipment dynamics at high ground speed. In: Proceedings of the ISTVS 8th Americas Regional Conference, Detroit, Michigan, U.S.A. International Society for Terrain Vehicle Systems.

Payne, P., 1956. The relationship between the mechanical properties of soil and the performance of simple cultivation implements. Ph.D. thesis, University of Reading.

Pazooki, A., Rakheja, S., Cao, D., 2011. Modeling and validation of off-road vehicle ride dynamics. Mechanical Systems and Signal Processing 28, 679–695.

Reece, A., 1964. The fundamental equation of earth-moving mechanics. In: Proceedings of the Institution of Mechanical Engineers, Conference Proceedings. Vol. 179(6). SAGE Publications, pp. 16–22.

Rubinstein, D., Hitron, R., 2004. A detailed multi-body model for dynamic simulation of off-road tracked vehicles. J. Terramech. 41 (23), 163–173.

Sadek, M. A., Chen, Y., 2015. Feasibility of using pfc3d to simulate soil flow resulting from a simple soil-engaging tool. Trans. ASABE 58 (4), 987–996.

Shmulevich, I., Dec 2010. State of the art modeling of soil–tillage interaction using discrete element method. Soil and Tillage Research 111 (1), 41–53.

Shmulevich, I., Asaf, Z., Rubinstein, D., 2007. Interaction between soil and a wide cutting blade using the discrete element method. Soil Tillage Res. 97 (1), 37–50.

Söhne, W., 1956. Some basic considerations of soil mechanics as applied to agricultural engineering. National Institute of Agricultural Engineering.

Solhjou, A., Desbiolles, J. M. A., Fielke, J. M., 2013. Soil translocation by narrow openers with various blade face geometries. Biosystems Engineering 114 (3), 259–266.

Solhjou, A., Fielke, J. M., Desbiolles, J. M. A., 2012. Soil translocation by narrow openers with various rake angles. Biosystems Engineering 112 (1), 65–73.

Stafford, J. V., 1979. The performance of a rigid tine in relation to soil properties and speed. J. Agr. Eng. Res. 24 (1), 41–56.

Stafford, J. V., 1981. An application of critical state soil mechanics: The performance of rigid tines. J. Agr. Eng. Res. 26 (5), 387–401.

Stafford, J. V., 1984. Force prediction models for brittle and flow failure of soil by draught tillage tools. J. Agr. Eng. Res. 29 (1), 51–60.

Stafford, J. V., Tanner, D. W., 1983a. Effect of rate on soil shear strength and soil-metal friction I. Shear strength. Soil Tillage Res. 3 (3), 245–260.

Stafford, J. V., Tanner, D. W., 1983b. Effect of rate on soil shear strength and soil-metal friction II. Soil-metal friction. Soil Tillage Res. 3 (4), 321–330.

Statistics Canada, 2016. Saskatchewan Provincial Trends.
URL http://www.statcan.gc.ca/pub/95-640-x/2011001/p1/prov/prov-47-eng.htm

Stayner, R., Collins, T., Lines, J., 1984. Tractor ride vibration simulation as an aid to design. Journal of Agricultural Engineering Research 29 (4), 345–355.

Taheri, S., Sandu, C., Taheri, S., Pinto, E., Gorsich, D., 2015. A technical survey on terramechanics models for tire-terrain interaction used in modeling and simulation of wheeled vehicles. J. Terramech. 57, 1–22.

Tamás, K., Jóri, I. J., Mouazen, A. M., Nov 2013. Modelling soil–sweep interaction with discrete element method. Soil and Tillage Research 134, 223–231.

Terzaghi, K., 1943. Theoretical Soil Mechanics, 2nd Edition. John Wiley and Sons, New York.

The Mathworks, Inc., 2014. MATLAB.
URL http://www.mathworks.com/products/matlab/

United Nations: Department of Economic and Social Affairs, Population Division, 2015. World Population Prospects: The 2015 Revision, Key Findings and Advance Tables. Tech. Rep. ESA/P/WP.241., United Nations, New York.
URL https://esa.un.org/unpd/wpp/Publications/

Upadhyaya, S., Ma, T., Chancellor, W., Zhao, Y., 1987. Dynamics of soil-tool interactions. Soil Tillage Res. 9, 187–206.

Wakui, F., Terumichi, Y., 2011. Numerical simulation of tire behavior on soft ground. Journal of System Design and Dynamics 5 (3), 486–500.

Welch, P., 1967. The use of fast Fourier transform for the estimation of power spectra: A method based on time averaging over short, modified periodograms. IEEE Trans. Audio Electroacoust. 15 (2), 70–73.

Wheeler, P. N., Godwin, R. J., 1996. Soil dynamics of single and multiple tines at speeds up to 20 km/h. J. Agr. Eng. Res. 63 (3), 243–249.

Wong, J., 1978. Theory of Ground Vehicles. Wiley, New York.

Wong, J., 1989. Terramechanics and off-road vehicles. Elsevier.

Yong, R., Fattah, E., 1976. Prediction of wheel-soil interaction and performance using the finite element method. J. Terramech. 13 (4), 227–240.

Zhang, J., Kushwaha, R. L., 1995. A modified model to predict soil cutting resistance. Soil Tillage Res. 34 (3), 157–168.

Zhao, C., Zang, M., 2014. Analysis of rigid tire traction performance on a sandy soil by 3d finite element–discrete element method. Journal of Terramechanics 55, 29–37.

Appendix A

Development of dynamic equations

A.1 Kinematic and kinetic relationships

The plot drill was simplified and represented by the 2-D schematic shown in Fig. A.1. It consisted of the front hitch and boom structure which were reduced to one lumped mass, the front walking axle, the subframe that the row units mount to, the air cart hitch used when towing the air cart behind the plot drill, and its support link, the tail wheel link and its support link, and three row units that connect to the subframe via parallel links. The walking axle was moved to directly below the boom structure's center of gravity. The rear walking axle wheel experienced a delayed version of the terrain experienced by the front walking axle wheel. The boom is restricted to only a vertical degree of freedom. The tail wheel experienced a unique terrain profile. Each row unit experienced a unique random terrain profile because of the lateral offsets between row units on the actual machine. All terrain profiles were generated from a common underlying power spectral density. Details of the terrain experienced by the packer wheel are given in Sec. 3.4.3.

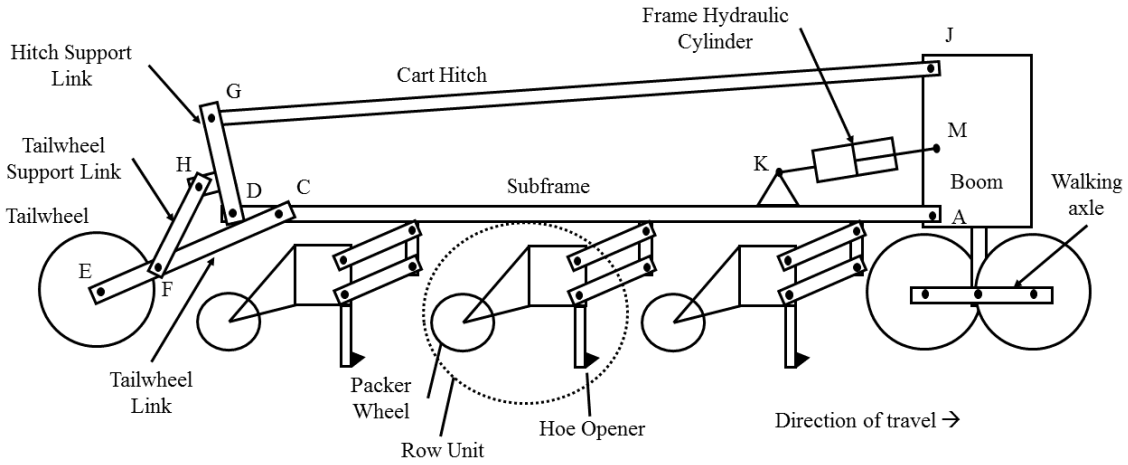

Figure A.1: A schematic of the 2-D plot drill model that was developed for dynamic modelling

The kinetic equations were developed from the free body diagrams (FBDs) of the individual components of the plot drill. Geometry, mass, and inertia data were taken from available engineering design drawings. The kinematics describe the relative motion of the plot drill components, and the kinetic equations reflect the accelerations that result from internal forces (at the connections between components) and external forces (from soil-tire and soil-tool contact) acting on the plot drill components. The equations were developed in a non-rotating, non-accelerating reference frame, using a coordinate system common to all FBDs.

The time-domain integration of the state variables of the model (using 4th order Runge-Kutta integration) allowed the motion of the machine to be predicted as the plot drill passed over given terrain inputs with the openers engaging the soil. The development of the dynamic equations follows in this appendix.

Because of the right hand coordinate system selected for modelling ($+y$ into the page), positive angles were clockwise as viewed in the following FBDs. A list of symbols is given in Appendix C.

A.1.1 Boom FBD

Equations based on Newtonian mechanics were developed for the boom using the FBD in Fig. A.2. Because the forward velocity of the boom was constant, the x-direction acceleration, $a_{O_{BOOM_x}}$, was zero in Eq. (A.1) and a dummy force, F_{TOW} was applied at the center of gravity (CG) of the boom, o_{BOOM}, to mimic the boundary condition of being towed at a constant velocity. Because the boom did not rotate, a boundary condition moment, M_{TOW}, was also applied at o_{BOOM}, and the angular acceleration of the boom, α_{BOOM}, was set to zero in Eq. (A.3). Reaction forces acting at pinned connections are labeled by capital, non-bold letters with subscripts along their direction of action.

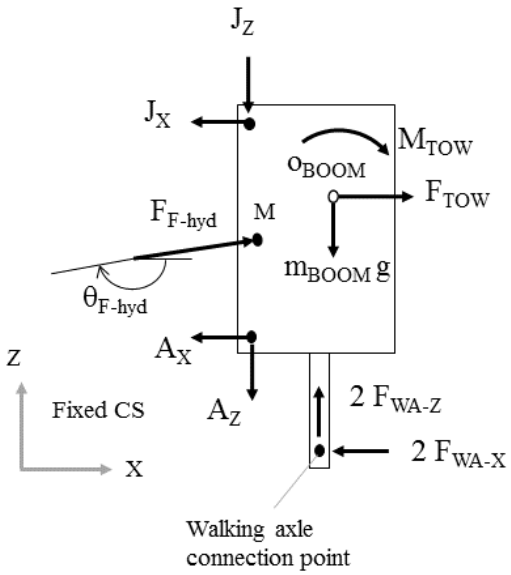

Figure A.2: Free body diagram of modelled boom. To maintain proper absolute walking axle tire loads in 2-D, the walking axle pivot reaction forces were scaled accordingly.

To minimize the number of angles tracked in the simulation tool, one angular quantity was used to describe the orientation of the frame hydraulic cylinder force, F_{F-hyd}, even though an equal and opposite force is applied at both connection points of the cylinder. To remain consistent with Newton's Law third law, this angle, θ_{F-hyd}, aligned with the tail of the force vector, F_{F-hyd}, in Fig. A.2, and aligned with the force vector in Fig. A.4 where the opposite end of the cylinder connects at point K. This explains the modification of angular quantities by 180° in the kinetic equations derived throughout this appendix. An example highlighting

the angular convention used at the frame hydraulic cylinder is given in Fig. A.3. Because of the selected right-hand coordinate system, all *sin* functions included a leading negative sign.

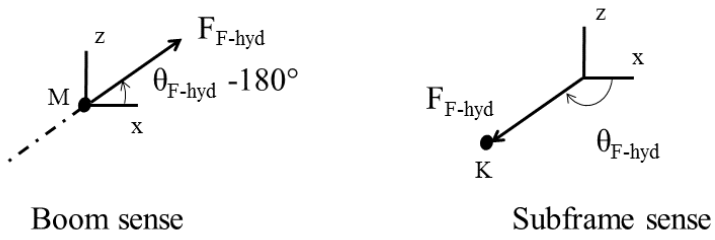

Figure A.3: The same angular quantity was used to describe the force vector in both diagrams by shifting the phase by 180°. Given the chosen coordinate system, the vertical component of F_{F-hyd} in the subframe sense was computed by $-F_{F-hyd}\sin(\theta_{F-hyd})$.

The absolute force acting on the tire treadband was required in soil-tire interaction calculations (compared to modelling changes from the static equilibrium force), therefore, the simplification to a single walking axle in the model required scaling the reaction forces between the boom and the walking axle by a factor of two. This is shown in Fig. A.2, and reflected in Eqs. (A.1) and (A.2).

$$\begin{aligned} &\sum F_x = m_{BOOM} a_{O_{BOOM_x}} = 0 \\ &F_{F-hyd}\cos(\theta_{F-hyd} - 180°) - A_x - J_x - 2F_{WA-X} + F_{TOW} = 0 \end{aligned} \tag{A.1}$$

$$\begin{aligned} &\sum F_z = m_{BOOM} a_{O_{BOOM_z}} \\ &2F_{WA-Z} - A_z - J_z - m_{BOOM} g - F_{F-hyd}\sin(\theta_{F-hyd} - 180°) = m_{BOOM} a_{O_{BOOM_z}} \end{aligned} \tag{A.2}$$

The moment equations were developed using vector cross products to maintain geometric generality, however only moments about the Y-axis of the fixed coordinate system resulted. In Eq. (A.3), $\vec{r}_{X/Y}$ is the relative position vector of point X with respect to point Y in the fixed coordinate system. In the moment equations, the reaction forces are presented in vector form (e.g., $\vec{A}$). The moment equation of the boom was equal to 0 because of the applied towing moment. Because of the restriction to 2-D planar motion, the inertia term I_{BOOM} in Eq. (A.3), and subsequent moment equations, was equal to the moment inertia about the y-axis of the boom component. The equation was

$$\begin{aligned} &\sum \vec{M}_{O_{BOOM}} = I_{BOOM}\alpha_{BOOM} = 0 \\ &\vec{M}_{TOW} + \vec{r}_{J/O_{BOOM}} \times \vec{J} + \vec{r}_{A/O_{BOOM}} \times \vec{A} + \vec{r}_{FW/O_{BOOM}} \times 2\vec{F}_{WA} \\ &\quad + \vec{r}_{M/O_{BOOM}} \times \vec{F}_{F-hyd} = 0. \end{aligned} \tag{A.3}$$

The model was developed in an inertial reference frame, therefore, the absolute acceleration of various points on the plot drill were computed without the need for rotating frames

of reference. Given the limited DOFs of the boom, the kinematic relationship of points on the boom rigid body was trivial, namely

$$\vec{v}_{O_{BOOM}} = \vec{v}_A = \vec{v}_J, \tag{A.4}$$

and

$$\vec{a}_{O_{BOOM}} = \vec{a}_A = \vec{a}_J. \tag{A.5}$$

A.1.2 Subframe FBD

Force and moment equations were developed for the subframe based on the FBD in Fig. A.4. The links of the k-th row unit remain parallel, so the orientation of both links was described by $\theta_{Link_k} = \theta_{Link1-k} = \theta_{Link2-k}$.

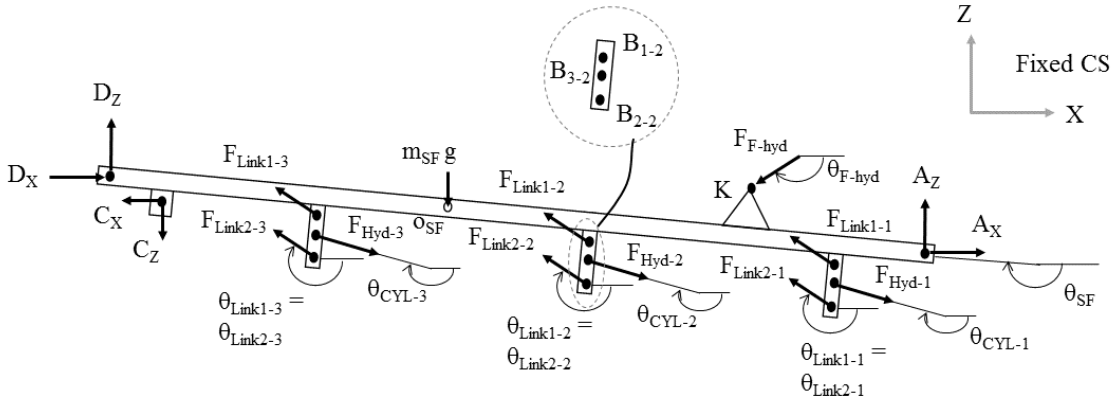

Figure A.4: Free body diagram of modelled subframe.

As shown in Fig. A.4, the links between the subframe and each row unit were assumed to be in tension. The hydraulic cylinders between the subframe and each row unit were assumed to apply a compressive force at the cylinder mounting points, similar to the frame hydraulic cylinder. Again, minimizing the number of angle values used in the FBDs resulted in θ_{Cyl-k} describing the tail of F_{Hyd-k} in Fig. A.4.

The force summations in the x and z directions considers the motion of the subframe in both directions, and were given by

$$\begin{aligned}
&\sum F_x = m_{SF} a_{O_{SF_x}} \\
&D_x - C_x + A_x + F_{F-hyd}\cos(\theta_{F-hyd}) + \sum_{k=1}^{3}\Big[F_{Link1-k}\cos(\theta_{Link_k}) + F_{Link2-k}\cos(\theta_{Link_k}) \\
&\quad + F_{Hyd-k}\cos(\theta_{Cyl-k} - 180\Big] = m_{SF} a_{O_{SF_x}},
\end{aligned} \tag{A.6}$$

and

$$\sum F_z = m_{SF} a_{O_{SF_z}}$$

$$D_z - C_z + A_z - m_{SF} g - F_{F-hyd} \sin(\theta_{F-hyd}) - \sum_{k=1}^{3} \Big[F_{Link1-k} \sin(\theta_{Link_k}) + F_{Link2-k} \sin(\theta_{Link_k}) + F_{Hyd-k} \sin(\theta_{Cyl-k} - 180°) \Big] = m_{SF} a_{O_{SF_z}}. \tag{A.7}$$

The moment summation was

$$\sum \vec{M}_{O_{SF}} = I_{SF} \alpha_{SF}$$

$$\vec{r}_{D/O_{SF}} \times \vec{D} + \vec{r}_{C/O_{SF}} \times \vec{C} + \vec{r}_{A/O_{SF}} \times \vec{A} + \vec{r}_{K/O_{SF}} \times \vec{F}_{F-hyd} + \sum_{k=1}^{3} \Big[\vec{r}_{B_{1-k}/O_{SF}} \times \vec{F}_{Link1-k} + \vec{r}_{B_{2-k}/O_{SF}} \times \vec{F}_{Link2-k} + \vec{r}_{B_{3-k}/O_{SF}} \times \vec{F}_{Hyd-k} \Big] = I_{SF} \alpha_{SF}. \tag{A.8}$$

The velocities of connection point D and the subframe CG point O_{SF} were given by

$$\vec{v}_D = \vec{v}_A + \vec{\omega}_{SF} \times \vec{r}_{D/A}, \tag{A.9}$$

and

$$\vec{v}_{O_{SF}} = \vec{v}_A + \vec{\omega}_{SF} \times \vec{r}_{O_{SF}/A} \tag{A.10}$$

where $\vec{\omega}_{SF}$ was the angular velocity of the subframe. The accelerations of these points were

$$\vec{a}_D = \vec{a}_A + \vec{\alpha}_{SF} \times \vec{r}_{D/A} + \vec{\omega}_{SF} \times (\vec{\omega}_{SF} \times \vec{r}_{D/A}), \tag{A.11}$$

and

$$\vec{a}_{O_{SF}} = \vec{a}_A + \vec{\alpha}_{SF} \times \vec{r}_{O_{SF}/A} + \vec{\omega}_{SF} \times (\vec{\omega}_{SF} \times \vec{r}_{O_{SF}/A}) \tag{A.12}$$

where $\vec{\alpha}_{SF}$ was the angular acceleration of the subframe.

A.1.3 Cart hitch FBD

The equations for the hitch were developed based on the FBD in Fig. A.5. Due to its significant mass, it was not treated as a two force member.

The force and moment summations were

$$\begin{aligned} \sum F_x &= m_{HITCH} a_{O_{HITCH_x}} \\ G_x + J_x &= m_{HITCH} a_{O_{HITCH_x}}, \end{aligned} \tag{A.13}$$

$$\begin{aligned} \sum F_z &= m_{HITCH} a_{O_{HITCH_z}} \\ G_z + J_z - m_{HITCH} g &= m_{HITCH} a_{O_{HITCH_z}}, \end{aligned} \tag{A.14}$$

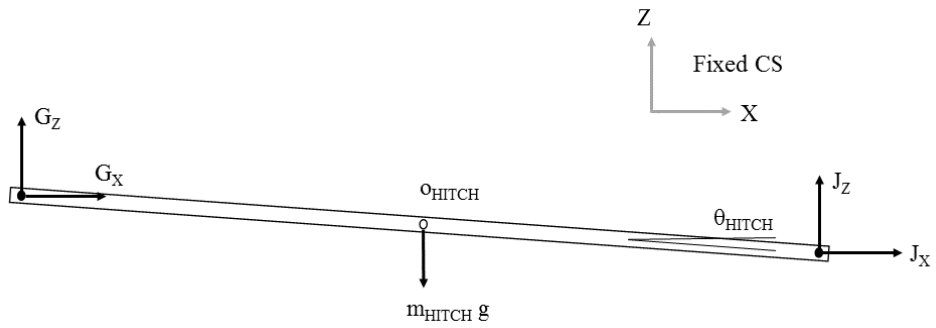

Figure A.5: Free body diagram of the air cart hitch.

and

$$\begin{aligned} \sum \vec{M}_{O_{HITCH}} &= I_{HITCH}\alpha_{HITCH} \\ \vec{r}_{G/O_{HITCH}} \times \vec{G} + \vec{r}_{J/O_{HITCH}} \times \vec{J} &= I_{HITCH}\alpha_{HITCH}. \end{aligned} \tag{A.15}$$

Similarly to the subframe, the velocities of connection point G and the hitch CG point O_{HITCH} were expressed by

$$\vec{v}_G = \vec{v}_J + \vec{\omega}_{HITCH} \times \vec{r}_{G/J}, \tag{A.16}$$

and

$$\vec{v}_{O_{HITCH}} = \vec{v}_J + \vec{\omega}_{HITCH} \times \vec{r}_{O_{HITCH}/J}. \tag{A.17}$$

The accelerations were given by

$$\vec{a}_G = \vec{a}_J + \vec{\alpha}_{HITCH} \times \vec{r}_{G/J} + \vec{\omega}_{HITCH} \times (\vec{\omega}_{HITCH} \times \vec{r}_{G/J}), \tag{A.18}$$

and

$$\vec{a}_{O_{HITCH}} = \vec{a}_J + \vec{\alpha}_{HITCH} \times \vec{r}_{O_{HITCH}/J} + \vec{\omega}_{HITCH} \times (\vec{\omega}_{HITCH} \times \vec{r}_{O_{HITCH}/J}). \tag{A.19}$$

A.1.4 Hitch support FBD

Equations for the hitch support link were developed based on the FBD in Fig. A.6.

For physical consistency θ_{TWSL} describes the tail-direction of the tail wheel support link reaction force, F_{TWSL}, in Fig. A.6. Its reaction at the tail wheel link (Sec. A.1.5) remains consistent with Newton's third law.

The summation of forces in the x and z direction, and moments about the CG were given by

$$\begin{aligned} \sum F_x &= m_{HSUPP} a_{O_{HSUPP_x}} \\ -D_x - G_x + F_{TWSL}\cos(\theta_{TWSL} - 180°) &= m_{HSUPP} a_{O_{HSUPP_x}}, \end{aligned} \tag{A.20}$$

$$\begin{aligned} \sum F_z &= m_{HSUPP} a_{O_{HSUPP_z}} \\ -D_z - G_z - m_{HSUPP} g - F_{TWSL}\sin(\theta_{TWSL} - 180°) &= m_{HSUPP} a_{O_{HSUPP_z}}, \end{aligned} \tag{A.21}$$

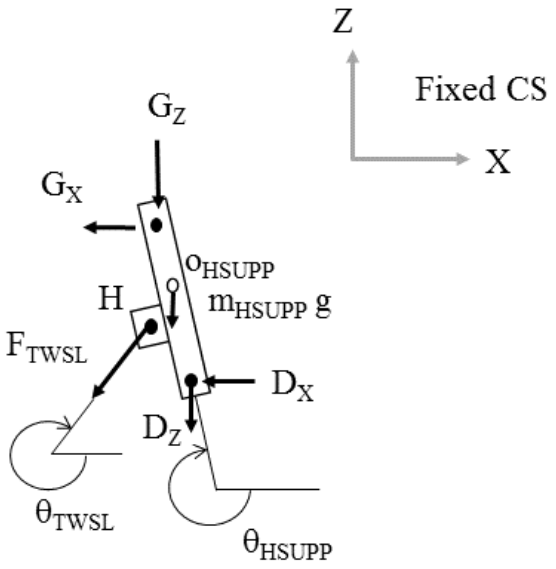

Figure A.6: Free body diagram of the hitch support link.

and

$$\begin{aligned} &\sum \vec{M}_{O_{HSUPP}} = I_{HSUPP}\alpha_{HSUPP} \\ &\vec{r}_{G/O_{HSUPP}} \times \vec{G} + \vec{r}_{D/O_{HSUPP}} \times \vec{D} + \vec{r}_{H/O_{HSUPP}} \times \vec{F}_{TWSL} = I_{HSUPP}\alpha_{HSUPP}. \end{aligned} \tag{A.22}$$

In addition to Eq. (A.16), $\vec{v}_G$ was also expressed by considering $\vec{v}_D$ and the angular velocity of the hitch support, namely

$$\vec{v}_G = \vec{v}_D + \vec{\omega}_{HSUPP} \times \vec{r}_{G/D}. \tag{A.23}$$

The velocity of the hitch support CG then became

$$\vec{v}_{O_{HSUPP}} = \vec{v}_D + \vec{\omega}_{HSUPP} \times \vec{r}_{O_{HSUPP}/D}. \tag{A.24}$$

The vector components of Eqs. (A.16) and (A.23) were equated, because both equations defined $\vec{v}_G$. Specifically, when the cross product of Eq. (A.16) was evaluated,

$$\vec{v}_G = (v_{J_x} + \omega_{HITCH} r_{G/J_z})\hat{i} + (v_{J_z} + \omega_{HITCH} r_{G/J_x})\hat{k}. \tag{A.25}$$

Equation (A.23) were evaluated including the substitution of the definition of $\vec{v}_D$ from Eq. (A.9) to give

$$\vec{v}_G = (v_{A_x} + \omega_{SF} r_{D/A_z} + \omega_{HSUPP} r_{G/D_z})\hat{i} + (v_{A_z} + \omega_{SF} r_{D/A_x} + \omega_{HSUPP} r_{G/D_x})\hat{k}. \tag{A.26}$$

Equating the components of Eqs. (A.25) and (A.26) and rearranging results in a linear system of two equations in terms of unknowns ω_{hsupp} and ω_{hitch} defined in terms of ω_{SF}. Considering Eq. (A.4), the system was given by

$$\omega_{HITCH} r_{G/J_z} - \omega_{HSUPP} r_{G/D_z} = \omega_{SF} r_{D/A_z}, \tag{A.27}$$

and

$$\omega_{HITCH} r_{G/J_x} - \omega_{HSUPP} r_{G/D_x} = \omega_{SF} r_{D/A_x}. \tag{A.28}$$

Similarly, $\vec{a}_G$ was also expressed by considering $\vec{a}_D$ and the angular velocity and acceleration of the hitch support link by

$$\vec{a}_G = \vec{a}_D + \vec{\alpha}_{HSUPP} \times \vec{r}_{G/D} + \vec{\omega}_{HSUPP} \times (\vec{\omega}_{HSUPP} \times \vec{r}_{G/D}). \tag{A.29}$$

The acceleration of the hitch support CG became

$$\vec{a}_{O_{HSUPP}} = \vec{a}_D + \vec{\alpha}_{HSUPP} \times \vec{r}_{O_{HSUPP}/D} + \vec{\omega}_{HSUPP} \times (\vec{\omega}_{HSUPP} \times \vec{r}_{O_{HSUPP}/D}). \tag{A.30}$$

The vector components of Eqs. (A.18) and (A.29) were equated, because both equations define $\vec{a}_G$. In a similar process to that used to equate velocity components, the linear system of equations became

$$\alpha_{HITCH} r_{G/J_z} - \alpha_{HSUPP} r_{G/D_z} = \alpha_{SF} r_{D/A_z} - \omega_{SF}^2 r_{D/A_x} - \omega_{HSUPP}^2 r_{G/D_x} + \omega_{HITCH}^2 r_{G/J_x}, \tag{A.31}$$

and

$$-\alpha_{HITCH} r_{G/J_x} + \alpha_{HSUPP} r_{G/D_x} = -\alpha_{SF} r_{D/A_x} - \omega_{SF}^2 r_{D/A_z} - \omega_{HSUPP}^2 r_{G/D_z} + \omega_{HITCH}^2 r_{G/J_z} \tag{A.32}$$

defined in terms of $\vec{\alpha}_{SF}$ and the previously computed angular velocity values.

A.1.5 Tail wheel link FBD

Kinematic and kinetic equations for the tail wheel link were developed based on the FBD in Fig. A.7. The tail wheel support link was assumed to act as a two-force member with negligible mass. This simplified the tail support link reaction force to F_{TWSL} acting long the centerline of the link, as defined by θ_{TWSL} as shown in Fig. A.7.

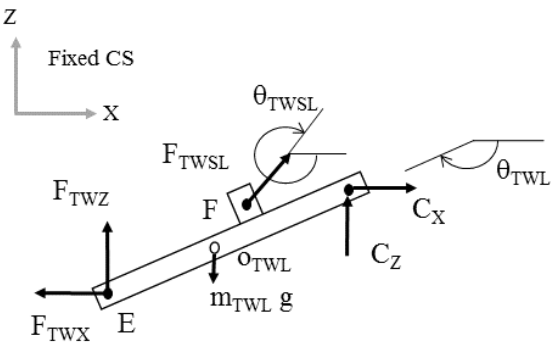

Figure A.7: Free body diagram of the tail wheel link.

The force equations in the x and z directions, and moment summation about the link CG were

$$\sum F_x = m_{TWL} a_{O_{TWL_x}}$$
$$C_x - F_{TWX} + F_{TWSL}\cos(\theta_{TWSL}) = m_{TWL} a_{O_{TWL_x}}, \tag{A.33}$$

$$\sum F_z = m_{TWL} a_{O_{TWL_z}}$$
$$C_z + F_{TWZ} - F_{TWSL}\sin(\theta_{TWSL}) - m_{TWL} g = m_{TWL} a_{O_{TWL_z}}, \tag{A.34}$$

and

$$\sum \vec{M}_{O_{TWL}} = I_{TWL}\alpha_{TWL}$$
$$\vec{r}_{C/O_{TWL}} \times \vec{C} + \vec{r}_{F/O_{TWL}} \times \vec{F}_{TWSL} + \vec{r}_{E/O_{TWL}} \times \vec{F}_{TW} = I_{TWL}\alpha_{TWL}. \tag{A.35}$$

Similar to Eqs. (A.9) and (A.11), kinematic values at connection point C between the subframe and tail wheel link were given by

$$\vec{v}_C = \vec{v}_A + \vec{\omega}_{SF} \times \vec{r}_{C/A} \tag{A.36}$$

and

$$\vec{a}_C = \vec{a}_A + \vec{\alpha}_{SF} \times \vec{r}_{C/A} + \vec{\omega}_{SF} \times (\vec{\omega}_{SF} \times \vec{r}_{C/A}). \tag{A.37}$$

The velocities of connection point F and the tail wheel link CG O_{TWL} were

$$\vec{v}_F = \vec{v}_C + \vec{\omega}_{TWL} \times \vec{r}_{F/C} \tag{A.38}$$

and

$$\vec{v}_{O_{TWL}} = \vec{v}_C + \vec{\omega}_{TWL} \times \vec{r}_{O_{TWL}/C}. \tag{A.39}$$

The velocity at F was also found considering the velocity of H on the hitch support (Fig.A.6) and the angular velocity of the tail wheel support link (ω_{TWSL})

$$\vec{v}_F = \vec{v}_H + \vec{\omega}_{TWSL} \times \vec{r}_{F/H}. \tag{A.40}$$

Similar to the process for solving the angular velocities of the four bar linkage involving the subframe, hitch, hitch support link, and boom, the components of Eqs. (A.38) and (A.40) were equated, forming a system of two equations with unknowns ω_{TWL} and ω_{TWSL}. Both $\vec{v}_C$ and $\vec{v}_H$ were functions of ω_{SF}, so Eqs. (A.38) and (A.40) were also dependent on ω_{SF}.

The accelerations of connection point F and the tail wheel link CG O_{TWL} were given by

$$\vec{a}_F = \vec{a}_C + \vec{\alpha}_{TWL} \times \vec{r}_{F/C} + \vec{\omega}_{TWL} \times (\vec{\omega}_{TWL} \times \vec{r}_{F/C}) \tag{A.41}$$

and

$$\vec{a}_{O_{TWL}} = \vec{a}_C + \vec{\alpha}_{TWL} \times \vec{r}_{O_{TWL}/C} + \vec{\omega}_{TWL} \times (\vec{\omega}_{TWL} \times \vec{r}_{O_{TWL}/C}). \tag{A.42}$$

The acceleration at F was found considering the acceleration at H on the hitch support link (Fig.A.6) along with the angular acceleration of the tail wheel support link (α_{TWSL}) following the calculation of the angular velocities of these links. Specifically,

$$\vec{a}_F = \vec{a}_H + \vec{\alpha}_{TWSL} \times \vec{r}_{F/H} + \vec{\omega}_{TWSL} \times (\vec{\omega}_{TWSL} \times \vec{r}_{F/H}). \tag{A.43}$$

Components of Eqs. (A.41) and (A.43) were equated because both define the acceleration at F. The system of two equations was solved for α_{TWL} and α_{TWSL}.

Points C and H were involved in solving for ω_{TWL}, ω_{TWSL}, α_{TWL}, and α_{TWSL}, so the velocity and acceleration of these points depended on ω_{SF} and α_{SF}; essentially, the motion of the entire rear frame structure with respect to the boom (hitch/subframe/hitch support link, and tail wheel link/tail wheel support link) was described by ω_{SF} and α_{SF} because of the 4-bar linkages of the frame.

A.1.6 Walking axle FBD

Equations were developed for the walking axle based on the FBD in Fig. A.8. The center of gravity of the walking axle was assumed to be at the pivot point with the boom, therefore the accelerations at this point were equal to those of the boom because boom rotation was not permitted. The walking axle had an angular DOF independent of the boom. The angle of the walking axle was given by θ_{WA}. The reaction force between the m-th walking axle wheel and the walking axle was given by $\vec{F}_{WWm}$.

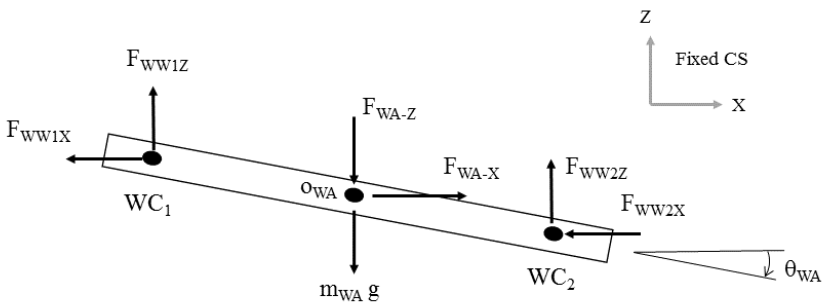

Figure A.8: A free body diagram of the modelled walking axle.

The force and moment summations were

$$\begin{aligned} &\sum F_x = m_{WA} a_{O_{WA_x}} \\ &F_{WA-X} - F_{WW1X} - F_{WW2X} = 0, \end{aligned} \tag{A.44}$$

$$\begin{aligned} &\sum F_z = m_{WA} a_{O_{WA_z}} \\ &F_{WW1Z} + F_{WW2Z} - F_{WA-Z} - m_{WA} g = m_{WA} a_{O_{WA_z}}, \end{aligned} \tag{A.45}$$

and

$$\begin{aligned} &\sum \vec{M}_{O_{WA}} = I_{WA} \alpha_{WA} \\ &\vec{r}_{WC_1/O_{WA}} \times \vec{F}_{WW_1} + \vec{r}_{WC_2/O_{WA}} \times \vec{F}_{WW_2} = I_{WA} \alpha_{WA}. \end{aligned} \tag{A.46}$$

The velocity of a walking axle wheel center ($WC_m, m = 1, 2$) was calculated from

$$\vec{v}_{WC_m} = \vec{v}_{O_{WA}} + \vec{\omega}_{WA} \times \vec{r}_{WC_m/O_{WA}}, \tag{A.47}$$

and the acceleration from

$$\vec{a}_{WC_m} = \vec{a}_{O_{WA}} + \vec{\alpha}_{WA} \times \vec{r}_{WC_m/O_{WA}} + \vec{\omega}_{WA} \times (\vec{\omega}_{WA} \times \vec{r}_{WC_m/O_{WA}}). \tag{A.48}$$

Thus, the angular position of the walking axle, θ_{WA}, and its derivatives with respect to time (ω_{WA} and α_{WA}), became a distinct DOF of the plot drill model.

A.1.7 Frame wheel FBD

Newtonian equations were developed for a general frame wheel (walking axle wheels or tail wheel) based on the FBD in Fig. A.9. The mass of the wheel and tire were concentrated to the generalized wheel center point WC. The sidewall forces also acted on the wheel center.

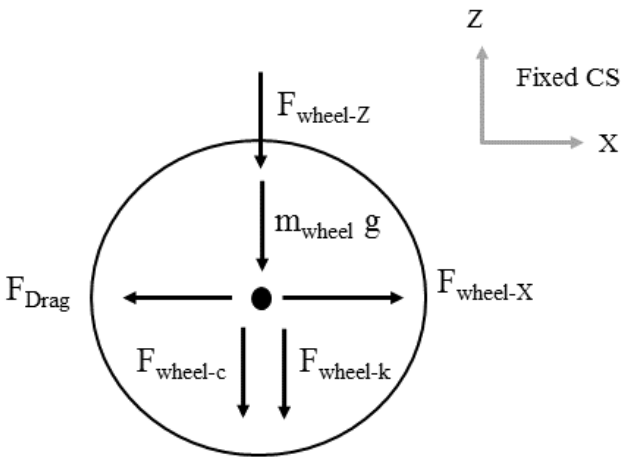

Figure A.9: Free body diagram of the tail or walking axle wheel.

$$\begin{aligned} \sum F_x &= m_{wheel} a_{WC_x} \\ F_{wheel-X} - F_{Drag} &= m_{wheel} a_{WC_x} \end{aligned} \tag{A.49}$$

$$\begin{aligned} \sum F_z &= m_{wheel} a_{WC_z} \\ - F_{wheel-Z} - m_{wheel} g - F_{wheel-c} - F_{wheel-k} &= m_{wheel} a_{WC_z} \end{aligned} \tag{A.50}$$

In Eqs. (A.49) and (A.50), the forces $F_{wheel-k}$ and $F_{wheel-c}$ represent the spring and viscous damper used to model the vertical sidewall deflection. Absolute reaction forces were needed in the deformable terrain modelling, so $F_{wheel-k}$ included the static load carried by the wheel. The direction of the side wall forces was chosen to reflect the extension of the sidewall being treated as a positive quantity; by this sign convention, $F_{wheel-k}$ was negative in the

static equilibrium configuration. $F_{wheel-X}$ and $F_{wheel-Z}$ were the reaction forces between the wheel and frame, and were opposite in direction to their counterparts acting on the frame, as in Fig. A.8 for example.

The rotational mechanics of all wheels in the model was neglected because all wheels were towed.

A.1.8 Treadband FBD

The forces acting on a rigid treadband were analyzed using the schematic in Fig. A.10. The treadband was considered massless, essentially acting as an interface between the pressure resulting from sinkage into the soil and the tire sidewall modelled as a nonlinear spring and viscous damper.

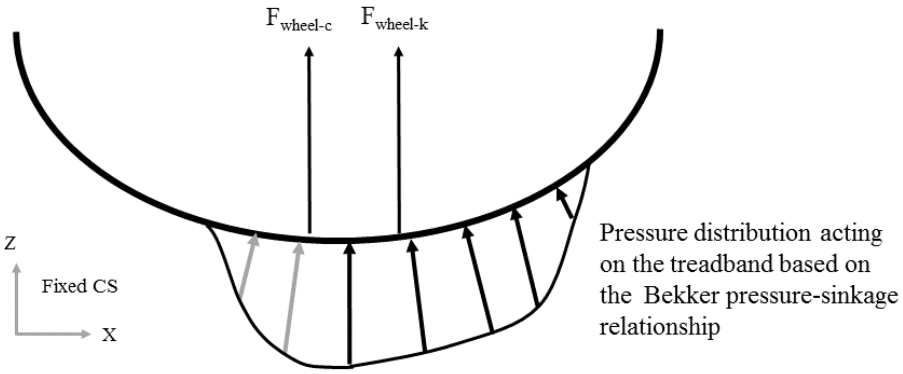

Figure A.10: A schematic of the forces acting on the rigid tire treadband. $F_{wheel-c}$ was modelled assuming an extension of the tire sidewall. $F_{wheel-k}$ also modelled assuming an extension of the sidewall from the static position, however the static load on the treadband was included in this force, therefore negative values of $F_{wheel-k}$ were typical.

The vertical force, F_z, to which Eqn. (3.1) must equate was calculated by

$$F_z = F_{static} - \kappa_{tire}\delta_{tire} - c_{tire}\dot{\delta}_{tire} \tag{A.51}$$

where F_{static} was the vertical static load on the wheel, κ_{tire} was the nonlinear stiffness of the tire sidewall, δ_{tire} was the deflection of the sidewall from the static configuration, c_{tire} was the damping coefficient of the tire sidewall, and $\dot{\delta}_{tire}$ was the relative velocity across the tire sidewall.

A.1.9 Row unit FBD

Force and moment equations for the i-th row unit were developed based on the FBD in Fig. A.11. Because the links remained parallel, their orientations were both described by θ_{Link_i}. Unlike the frame wheels, the packer wheel was not considered a separate body given its relatively small mass. As such, drag and side wall spring/damper forces were applied

directly to the packer wheel attachment point. Similar to the subframe FBD, because the links of the row unit remain parallel, the orientation of both links was described by $\theta_{Link_i} = \theta_{Link1-i} = \theta_{Link2-i}$.

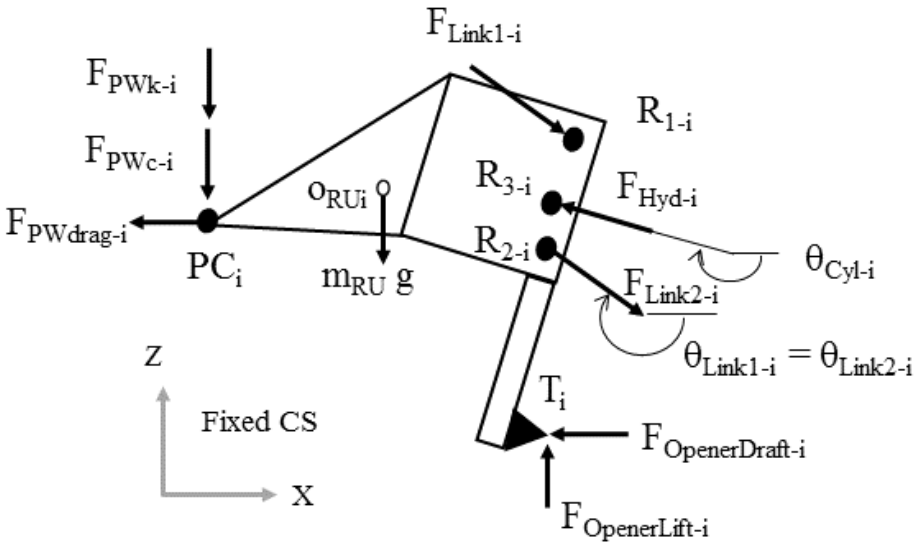

Figure A.11: Free body diagram of the i-th row unit.

The force and moment summations were give by

$$\sum F_x = m_{RU} a_{O_{RU_{i-x}}}$$
$$F_{Link1-i}\cos(\theta_{Link_i} - 180°) + F_{Link2-i}\cos(\theta_{Link_i} - 180°) + F_{Hyd-i}\cos(\theta_{Cyl_i}) - F_{OpenerDraft_i} - F_{PWdrag_i} = m_{RU} a_{O_{RU_{i-x}}}, \tag{A.52}$$

$$\sum F_z = m_{RU} a_{O_{RU_{i-z}}}$$
$$- F_{Link1-i}\sin(\theta_{Link_i} - 180°) - F_{Link2-i}\sin(\theta_{Link_i} - 180°) - F_{Hyd-i}\sin(\theta_{Cyl-i}) + F_{OpenerLift_i} - m_{RU} g - F_{PWk_i} - F_{PWc_i} = m_{RU} a_{O_{RU_{i-z}}}, \tag{A.53}$$

and

$$\sum \vec{M}_{O_{RU_i}} = I_{ru}\alpha_{RU_i}$$
$$\vec{r}_{PC_i/O_{RU_i}} \times \vec{F}_{PW_i} + \vec{r}_{T_i/O_{RU_i}} \times \vec{F}_{Opener_i} + \vec{r}_{R_{1-i}/O_{RU_i}} \times \vec{F}_{Link1-i} + \vec{r}_{R_{2-i}/O_{RU_i}} \times \vec{F}_{Link2-i} + \vec{r}_{R_{3-i}/O_{RU_i}} \times \vec{F}_{Hyd-i} = I_{ru}\alpha_{RU_i}. \tag{A.54}$$

The forces acting at the opener tip, $F_{OpenerDraft}$ and $F_{OpenerLift}$, were computed using the soil-tool interaction model explained in Sec. 3.4.4.

Assuming that the velocity and acceleration of row unit link points on the subframe (B_{1-i}, B_{2-i} and B_{3-i} – see Fig. A.4) were known, the kinematics of points on the row unit were developed considering the motion of the row unit links. For example, the velocity of the top link connection point was given by

$$\vec{v}_{R_{1-i}} = \vec{v}_{B_{1-i}} + \vec{\omega}_{TL_i} \times \vec{r}_{R_{1-i}/B_{1-i}}, \tag{A.55}$$

where $\vec{\omega}_{TL_i}$ was the angular velocity of the top link of the i-th row unit. The acceleration of this point was

$$\vec{a}_{R_{1-i}} = \vec{a}_{B_{1-i}} + \vec{\alpha}_{TL_i} \times \vec{r}_{R_{1-i}/B_{1-i}} + \vec{\omega}_{TL_i} \times (\vec{\omega}_{TL_i} \times \vec{r}_{R_{1-i}/B_{1-i}}). \tag{A.56}$$

The top and bottom row unit links were of equal length and remained parallel, so the row unit did not rotate relative to the subframe. Therefore, once $v_{R_{1-i}}$ was known, the absolute velocity of any other point on the row unit was computed with knowledge of ω_{SF}. For example, the velocity at the CG of the i-th row unit was given by

$$\vec{v}_{O_{RU_i}} = \vec{v}_{R_{1-i}} + \vec{\omega}_{SF} \times \vec{r}_{O_{RU_i}/R_{1-i}}. \tag{A.57}$$

The acceleration was computed by

$$\vec{a}_{O_{RU_i}} = \vec{a}_{R_{1-i}} + \vec{\alpha}_{SF} \times \vec{r}_{O_{RU_i}/R_{1-i}} + \vec{\omega}_{SF} \times (\vec{\omega}_{SF} \times \vec{r}_{O_{RU_i}/R_{1-i}}). \tag{A.58}$$

A.2 Summary

With all kinematic and kinetic relationships defined, the force, moment, and acceleration equations were arranged in a matrix to be solved using inversion within MATLAB®(The Mathworks, Inc., 2014). The velocity at any point on the plot drill was defined in terms of ω_{SF}, ω_{TL_i}, ω_{WA}, and v_{Boom_z}; these velocity values were determined from the 4th order Runge-Kutta integration of the acceleration variables α_{SF}, α_{TL_i}, α_{WA}, and a_{Boom_z}. Similarly, the position of the plot drill was determined from integrating the velocities ω_{SF}, ω_{TL_i}, ω_{WA}, and v_{Boom_z}.

The position and velocity states of the plot drill model were known at the beginning of the time step (from integration during the previous time step), so calculating the position and velocity of points of interest on the machine (i.e., wheel center points) was performed outside of the matrix inversion procedure; the position and velocity states were known at this stage in the simulation timestep. Within the structure of the computer program, position and velocity calculations were contained in functions separate from the main program.

Appendix B

Processing measured acceleration data

B.1 Background

Accelerations of various points on the plot drill were measured during equipment operation. However, because the coordinate systems (CS) of these sensors moved with the machine during testing, the components of gravity measured by each accelerometer changed as the machine moved during the test. Along with a brief overview of the data processing procedure, the process of transforming the acceleration data into a fixed non-inertial CS to correct the time-varying gravity components is outlined. The following procedure was based on the procedure given by Groves (2015) in *Navigation using inertial sensors*. Review of the full development of the method is left to the reader.

The angular orientation of the boom CS (B) with respect to an earth-fixed CS (F) was described using yaw-pitch-roll Euler angles (three consecutive finite rotations). At any point in time, the angular orientation of the boom CS could be described relative to the fixed CS first by rotating the boom CS about its z-axis by a yaw angle, ψ. The boom CS was then rotated about its y-axis by a pitch angle, θ. The final movement was a rotation of the boom CS about its x-axis by a roll angle, φ. Because the rotations were finite, the specific yaw-pitch-roll order must be maintained.

To transform a vector from the fixed CS to the boom CS, the effect of the yaw-pitch-roll Euler angles can be applied using three cascading rotation matrices. The yaw transformation was represented by

$$\mathbf{R}(\psi)_F^B = \begin{bmatrix} \cos\psi & -\sin\psi & 0 \\ \sin\psi & \cos\psi & 0 \\ 0 & 0 & 1 \end{bmatrix}. \tag{B.1}$$

The pitch transformation was given by

$$\mathbf{R}(\theta)_F^B = \begin{bmatrix} \cos\theta & 0 & \sin\theta \\ 0 & 1 & 0 \\ -\sin\theta & 0 & \cos\theta \end{bmatrix}. \tag{B.2}$$

The roll transformation was given by

$$\mathbf{R}(\varphi)_F^B = \begin{bmatrix} 1 & 0 & 0 \\ 0 & \cos\varphi & -\sin\varphi \\ 0 & \sin\varphi & \cos\varphi \end{bmatrix}. \tag{B.3}$$

By applying these three finite rotations in the correct order, the full transformation was given by

$$\mathbf{R}_F^B = \mathbf{R}(\varphi)_F^B \times \mathbf{R}(\theta)_F^B \times \mathbf{R}(\psi)_F^B = \begin{bmatrix} \cos\theta\cos\psi & \cos\theta\sin\psi & -\sin\theta \\ \sin\varphi\sin\theta\cos\psi - \cos\varphi\sin\psi & \sin\varphi\sin\theta\sin\psi + \cos\varphi\cos\psi & \sin\varphi\cos\theta \\ \cos\varphi\sin\theta\cos\psi + \sin\varphi\sin\psi & \cos\varphi\sin\theta\sin\psi - \sin\varphi\cos\psi & \cos\varphi\cos\theta \end{bmatrix} \tag{B.4}$$

where $\times$ is used to indicate matrix multiplication for clarity.

To rotate a vector from the boom CS to the fixed CS, the matrix transpose of $\mathbf{R}_F^B$ is used (e.g., $\mathbf{R}_B^F = \mathbf{R}_F^{B^T}$).

B.2 Data processing procedure

The following steps summarize the procedure used to convert the logged values to calibrated engineering units, with the appropriate transformations applied to acceleration data.

1. Logged data were recorded in the form of voltages and currents, as outlined in Sec. 4.2.4. Sensor calibrations were immediately applied in post-processing using MATLAB®(The Mathworks, Inc., 2014).

2. Data were downsampled to 100 Hz using a finite impulse response (FIR) low pass filter.

3. The stationary period of the implement immediately before movement started was identified by the user based on measured acceleration signals. The initial pitch and roll angles of the inertial measurement unit (IMU) mounted on the plot drill boom were computed from this stationary period based on the components of gravity identified in the boom X and Y directions (a_x and a_y, respectively).

   The initial pitch angle was found by

   $$\theta_{initial} = \arcsin(a_{x_{initial}}/g). \tag{B.5}$$

   The initial roll angle was then computed by

   $$\varphi_{initial} = \arcsin(a_{y_{initial}}/(g\cos(\theta_{initial}))). \tag{B.6}$$

4. With the initial roll and pitch angles known, and an assumed yaw angle of 0, an initial rotation was computed using Eq. (B.4).

5. The rotation matrix for the next time step was updated based on knowledge of the angular velocity of the boom CS at the current time step. The angular velocity of the boom CS was equal to the angular velocity of the boom as measured by the IMU gyroscope ($\vec{\omega}$). The update matrix $\mathbf{A}$, was given by

   $$\mathbf{A} = \begin{bmatrix} 1 & -\omega_\psi dt & \omega_\theta dt \\ \omega_\psi dt & 1 & -\omega_\varphi dt \\ -\omega_\theta dt & \omega_\varphi dt & 1 \end{bmatrix}. \tag{B.7}$$

Therefore, the rotation matrix at time $t + \Delta t$, from the fixed CS to the boom CS, was computed by

$$\mathbf{R}_F^B(t + \Delta t) = \mathbf{A} \times \mathbf{R}_F^B(t) \tag{B.8}$$

6. For an acceleration measurement from a given time step, the gravity component was removed by rotating the measured acceleration in the boom CS ($\vec{a}^B_{BOOM,meas}$) to the fixed CS and subtracting $g\hat{k}$ in the fixed CS, as gravity acted in the vertical direction ($\hat{k}$) of the fixed CS. Specifically, the gravity corrected acceleration of the boom in the fixed CS, $\vec{a}^F_{BOOM,corr}$, was computed by

$$\vec{a}^F_{BOOM,corr} = \mathbf{R}_B^F \times \vec{a}^B_{BOOM,meas} - g\hat{k}. \tag{B.9}$$

7. An additional CS was used to described the position of the subframe because it could pitch separately of the boom. However, the boom and subframe moved with the same yaw and roll motion. Essentially, the subframe CS orientation (SF) was computed by applying an additional rotation to the boom rotation matrix since the relative angle between the boom and subframe (θ_{SF}) was continuously measured during testing. It was given by

$$\mathbf{R}_F^{SF} = \begin{bmatrix} \cos\theta_{SF} & 0 & \sin\theta_{SF} \\ 0 & 1 & 0 \\ -\sin\theta_{SF} & 0 & \cos\theta_{SF} \end{bmatrix} \times \mathbf{R}_F^B. \tag{B.10}$$

Knowledge of the subframe CS at each time step was maintained by performing this additional boom CS rotation at each time step. $\mathbf{R}_F^{SF}$ was then used to rotate the subframe and row unit acceleration measurements to the fixed CS to removed the gravity contribution, similar to Step 6.

B.3 Conclusion

Due to the very small angles of rotation experienced by the plot drill, little difference resulted from applying the full rotation procedure above, as compared to just subtracting a constant g-offset from the vertical acceleration data. For thoroughness, the procedure was included. If future data collection efforts include terrain with significant topographic relief, a procedure similar to the one above may be appropriate.

Appendix C

List of symbols

Symbols used throughout the document are defined below.

Symbol	Description
g	Gravitational constant - 9.81 m/s^2
$\vec{a}$	A vector quantity
$\mathbf{A}$	A general matrix quantity
$\mathbf{A}^T$	The transpose of a matrix
τ	Shear stress
τ_{max}	Maximum shear stress
τ_{soil}	Shear strength of soil
c	Soil cohesion
σ	Normal stress
ϕ	Soil friction angle
γ	Soil density
d	Blade depth
c_a	Soil-metal adhesion
δ	Soil-metal friction angle
q	Surcharge pressure
N	Soil-related N-factor
P	Blade cutting force
α	Tool rake angle
β	Soil failure plane angle from surface
H	Horizontal component of cutting force
V	Vertical component of cutting force
u	Sinkage
p	Pressure
k	Soil sinkage coefficient
n	Soil sinkage exponent
b	Plate diameter or tire width
k_c	Cohesive sinkage coefficient
k_ϕ	Frictional sinkage coefficient
K	Shear deformation coefficient
R	Tire radius
τ	Shear stress
u_{max}	Sinkage at tire bottom
θ_{init}	Angle of initial soil-tire contact
θ_{exit}	Angle of final soil-tire contact
$\vec{F}$	A force vector
F_x	A force component in the x direction

F_{name}	An applied force representing the named component
k_{unload}	Slope of elastic soil recovery
A_o	Elastic soil recovery coefficient
A_k	Elastic soil recovery coefficient
$\dot{u}$	Sinkage velocity
m	Sinkage velocity exponent
k_o	Velocity-dependent pressure-sinkage coefficient
$A_{cylinder}$	Hydraulic cylinder piston area
$P_{hydraulic}$	Hydraulic pressure acting on piston face
κ_{Tire}	Tire sidewall vertical stiffness
c_{Tire}	Tire sidewall vertical damping coefficient
δ_{tire}	Tire sidewall deflection
$\dot{\delta}_{tire}$	Tire sidewall deflection rate
t	Time
L_{sep}	Longitudinal separation distance between the hoe opener tip and packer wheel center
t_{delay}	A time delay to travel a distance of L_{sep}
v	Velocity
t_i	Time at the i-th time step
$Z_{PW}(t)$	Packer wheel terrain elevation with time
$Z_{OP}(t)$	Opener terrain elevation with time
N_{span}	The number of discretization points of a length, *span*
$\delta_{OpenerEquilibrium}(t)$	The change from the opener's equilibrium position with time
$C_{feedback}$	Coefficient controlling amount of row unit position feedback
Δt	Time-step size
Δt^+ or Δt^-	The beginning (+) or end (-) of a simulation timestep
$\vec{u}_{init}$	A vector of initial sinkage iteration guesses at each tire
$\vec{u}_{result}$	A vector of sinkage iteration results at each tire
$\vec{F}_{soil}$	A vector of vertical soil contact forces at each tire
$\dot{\vec{x}}_{damper}$	A vector of tire sidewall damper velocities at each tire
$\vec{x}_{spring}$	A vector of tire spring damper deflections at each tire
P_{hyd}	Frame and/or row unit hydraulic operating pressure
G_{xx}	Power spectrum of signal x
γ^2_{xy}	Magnitude-squared coherence between signals x and y
f	Frequency
F_{BODY}	Applied force acting on the body specified in subscripts
F_{F-hyd}	Force applied by frame hydraulic cylinder
F_{Hyd-k}	Force applied by the k-th row unit hydraulic cylinder
M_{BODY}	Applied moment acting on the body specified in subscripts
θ_{BODY}	Angle describing the orientation of the body of interest in the fixed coordinate system (CS)

m_{BODY}	Mass of the body of interest
I_{BODY}	Mass of the body of interest
o_{BODY}	Center of gravity (CG) of the body of interest
$A_x - J_x$	Interaction forces in the x-direction at pinned connections between rigid bodies
$\vec{r}_{A/B}$	Relative position of point A relative to point B in the fixed CS
$v_{O_{BODY_x}}$	Velocity at the CG of the body of interest in the x direction
$\vec{v}_{O_{BODY}}$	Vector of velocity at the CG of the body of interest
$a_{O_{BODY_x}}$	Acceleration at the CG of the body of interest in the x direction
$\vec{a}_{O_{BODY}}$	Vector of acceleration at the CG of the body of interest
$\vec{\omega}_{BODY}$	Angular velocity vector of the body of interest
$\vec{\alpha}_{BODY}$	Angular acceleration vector of the body of interest
ψ	Yaw angle of a body
θ	Pitch angle of a body
ϕ	Roll angle of a body
$\hat{i}$	A unit vector
$\mathbf{R}(\psi)_F^B$	A rotation matrix from the fixed CS to the boom CS only due to a yaw rotation
$\vec{a}^F_{BOOM,meas}$	A measured acceleration of the boom in the fixed CS